## **POLITECNICO DI TORINO**

Master's Degree in Environmental and Land Engineering



MASTER'S DEGREE THESIS

# High-resolution data for Urban Heat Island analysis: a case study in Turin's District 6

Supervisor:	Candidate:
Prof. Piero Boccardo	Stefano De Razza

## Ringraziamenti

Desidero ringraziare il Prof. Boccardo per l'impegno e la passione che mette nel suo lavoro, e per la sua capacità di trasmettere entusiasmo e curiosità. Lo ringrazio per la disponibilità con cui ha accolto la mia proposta di approfondire un argomento per me tanto importante, incoraggiandomi a esplorarlo da nuove prospettive.

Un ringraziamento speciale va alla mia famiglia, da sempre il mio punto di riferimento. Sapete bene che non sono di molte parole, ma desidero dedicare questo lavoro a voi, come simbolo degli anni trascorsi lontano, fatti di sacrifici e attese. Grazie per aver sempre creduto in me, per avermi sostenuto con la vostra presenza costante e per avermi insegnato che la determinazione e l'amore sono la vera base di ogni traguardo. Senza di voi, tutto questo non sarebbe stato possibile.

To Tomy, thank you for always being by my side, despite the space between us. Thank you for your love, your patience, and for the calm you bring into my storms. Your guidance has always been true and wise, helping me find my way even when things felt uncertain. You are like an iceberg that keeps me from sinking and you will always be my safe place.

Grazie ai miei coinquilini, compagni di università e amici, in particolare per le risate condivise, le cene improvvisate e il sostegno reciproco in ogni fase di questo percorso. Ognuno di voi ha contribuito a rendere questi anni un'esperienza non solo di studio, ma soprattutto di crescita e di momenti che porterò per sempre con me.

#### **Abstract**

More frequent and intense heatwaves are just one of the consequences of anthropogenic climate change. Cities are among the areas most exposed and vulnerable to heat, generating what is known as the Urban Heat Island (UHI) effect. This phenomenon has been largely studied in recent years, especially using thermal sensors on satellites, but few studies investigate the phenomenon at the microscale, providing more accurate data.

The present study aims to investigate the urban microclimate of a section of District 6 in the city of Turin on a day classified as a heatwave in August 2025, using airborne LiDAR and thermal infrared data at 1 m resolution. Among the primary objectives are to study the thermal response of different soil types during daytime and nighttime hours. Simultaneously, the study models, using a GIS-based approach, the variation in shading and solar irradiance received at ground level throughout the day, as well as estimates other geometric factors such as the Sky View Factor, which describes urban canyoning. These models derive from Digital Elevation Models (DEMs) obtained from LiDAR surveys.

The statistical analyses that are conducted on the same study area provide results consistent with those found in the literature and highlight the important role of shading and vegetation in decreasing surface temperatures during daytime hours.

Using a dynamic shade optimisation approach, the study aims to provide various pedestrian routes to reach different areas of the study area, minimising sun exposure throughout the day. This can help increase thermal comfort and highlight the most vulnerable zones, known as hot spots, as well as the safe spots. Moreover, the study provides an easily replicable methodological approach to identify heat-vulnerable areas where mitigation measures can be adopted to reduce vulnerability.

#### Keywords:

Urban Heat Island (UHI), LiDAR, Airborne Thermal Remote Sensing, DEM-based Modelling, Urban Heat Vulnerability.

# Table of Contents

Absti	ract	I
List o	of Tables	III
List o	of Figures	V
Acro	nyms	VIII
1.	Introduction	1
1.	Purpose and Scope of the Study	1
1.2	2 Study Area	3
2.	Heatwaves and Urban Heat Islands	5
2.	Overview of Climate Change, Heatwaves, and Urban Heat Islands	5
2.2	2 Climate Analysis	7
	2.2.1 Long-term Temperature Analysis	8
	2.2.2 Heatwaves Analysis	10
	2.2.3 Tropical Nights Analysis	12
3.	LiDAR Technology	14
3.	1 Overview of LiDAR	14
	3.1.1 Laser Properties	16
3.2	2 LiDAR Data Processing and Products	17
	3.2.1 LiDAR Data Processing and Validation	19
	3.2.2 Validation with Ground Control Points	23
3.3	Feature Extraction from LiDAR Data	25
	3.3.1 Land-Use and Land-Cover Classification	26
4.	Shadow Analysis	29
5	Linhan Cannons and Slav View Factor	22

<i>6. 1</i>	Solar Irradiance and Radiative Exchange in Urban Area	37
6.1	Fundamentals of Solar Irradiance	37
6.2	Radiative Properties and Energy Balance in Urban Environments	38
6.3	Solar Radiation Models	42
<i>7</i> . ′	Thermal Remote Sensing	47
7.1	Principles of Thermal Remote Sensing	47
7.2	Resolution of Thermal Images	50
7.3	Acquisition and Processing of High-Resolution Thermal and Multispectral	Data51
<i>8</i> . <i>8</i>	Statistical Analysis	61
8.1	Day vs Night Temperature Analysis	61
8.2	2 Temperature by Land Cover Class	63
8.3	Day-Night Temperature Differences by Land Cover	66
8.4	Effect of Shading on Surface Temperature	68
8.5	5 SVF by Land Cover Class	72
8.6	Temperature by SVF Class	74
8.7	7 Solar Irradiance by Land Cover Class	79
8.8	Solar Irradiance by SVF Class	81
8.9	Daytime Temperature by Solar Irradiance Class	83
9.	Urban Heat Vulnerability Assessment	86
10.	Conclusions	96
11	References	00

# List of Tables

Table 2.1 - Regression results on residuals of daily maximum and minimum temperatures	9
Table 2.2 - Linear regression results of HW and hot days	12
Table 2.3 - Linear regression results of tropical nights	13
Table 3.1 - Typical specifications of airborne LiDAR systems	17
Table 3.2 - Summary of LiDAR point cloud files used in the study	22
Table 3.3 - DTM vertical accuracy,	24
Table 3.4 - Summary of land-use and land-cover classes	28
Table 6.1 - Representative absorptivity and albedo values for various surfaces	40
Table 6.2 - Representative emissivity values for various surface materials	41
Table 6.3 - Outputs produced by the r.sun.incidout model	43
Table 7.1 - Summary of infrared spectral regions	48
Table 7.2 - Main technical and operational parameters of the flight plan	54
Table 7.3 - Characteristics of GCPs	56
Table 8.1 - Descriptive statistics of temperature for daytime and nighttime acquisitions	62
Table 8.2 - Mean temperature difference between day and night	62
Table 8.3 - Daytime temperature statistics for different soil classes	63
Table 8.4 - Daytime temperature differences between soil classes	64
Table 8.5 - Nighttime temperature statistics for different soil classes	65
Table 8.6 - Nighttime temperature differences between soil classes	66
Table 8.7 - Descriptive statistics of ΔT between soil classes	67
Table 8.8 - Day-night ΔT between soil classes	67
Table 8.9 - Descriptive statistics of temperatures in shaded versus unshaded areas	68
Table 8.10 - Comparison of temperatures for non-shadow versus shadow areas	69
Table 8.11 - Descriptive statistics of daytime temperature by soil class and shade	69
Table 8.12 - Differences in temperature shadow vs non-shadow areas between soil classe	s 70
Table 8.13 - Descriptive statistics of SVF by soil class	72
Table 8.14 - SVF differences between soil classes	73
Table 8.15 - Descriptive statistics of daytime temperature by SVF class	74
Table 8.16 - Descriptive statistics of nighttime temperature by SVF class	75
Table 8.17 - Descriptive statistics of ΔT by SVF class	75
Table 8.18 - Daytime temperature differences between SVF classes	76

Table 8.19 - Nighttime temperature differences between SVF classes	77
Table 8.20 - $\Delta T$ between SVF classes	77
Table 8.21 - Linear regression parameters and t-test for slope of temperature vs SVF $\dots$	78
Table 8.22 - Descriptive statistics of total solar irradiance by soil class	79
Table 8.23 - Differences of total solar irradiance between soil classes	80
Table 8.24 - Descriptive statistics of total solar irradiance by SVF class	81
Table 8.25 - Differences of total solar irradiance between SVF classes	82
Table 8.26 - Descriptive statistics of daytime temperature by solar irradiance class	83
Table 8.27 - Differences of daytime temperature between solar irradiance classes	84

# List of Figures

Figure 1.1 - Methodological framework	2
Figure 1.2 - Study area: a section of District 6 in Turin	3
Figure 2.1 - Location of Torino Caselle weather station	7
Figure 2.2 - Maximum and minimum temperatures from 1st January 1995 to 31st	December
2024: (A) Maximum temperatures; (B) Residuals of maximum temperatures; (C)	) Minimum
temperatures; (D) Residuals of minimum temperatures	9
Figure 2.3 - Daily classification: heatwaves, hot days, and no data	11
Figure 2.4 - Annual frequency of hot days and HWS with trend lines	11
Figure 2.5 - Daily distribution of tropical nights	13
Figure 2.6 - Annual frequency of tropical nights with trend line	13
Figure 3.1 - Schematic of the airborne survey system	16
Figure 3.2 - (A) Digital Surface Model (DSM); (B) Digital Terrain Model (DTM)	); (C) Non-
Vegetated Surface (NVS)	18
Figure 3.3 - Complementary attributes of the LiDAR point cloud in a portion of	f the study
area. (A) True colour RGB; (B) Point elevation; (C) Automatic point classification	cation; (D)
LiDAR intensity	20
Figure 3.4 - Digital Terrain Model (DTM) of the study area	21
Figure 3.5 - Digital Surface Model (DSM) of the study area	21
Figure 3.6 - Ground Control Points (GCPs)	24
Figure 3.7 - (A) Residuals distribution; (B) Absolute error distribution	25
Figure 3.8 - Combined visualisation of building (red) and vegetation canopy (gre	en) heights
in the study area	26
Figure 3.9 - Classification of land-use and land-cover	27
Figure 4.1 - Cumulative daily shading map	30
Figure 4.2 - Shading simulation.	31
Figure 4.3 - Percentage of solar radiation exposure and shaded area	32
Figure 4.4 - Solar noon shading simulation	32
Figure 5.1 - Concept of Sky View Factor (SVF): open sky (SVF = 1) vs obstructe	d locations
(0 < SVF < 1)	33

Figure 5.2 - Illustration of SVF derivation: Google Street View fisheye images (top	), horizon
detection (bottom), and resulting SVF (bold) for four worldwide locations (Mic	ldel et al.,
2018)	34
Figure 5.3 - Sky View Factor (SVF)	35
Figure 5.4 - Classified SVF	35
Figure 6.1 - Direct, diffuse, and reflected irradiance	38
Figure 6.2 - Modelled solar irradiance: (A) Direct irradiance; (B) Diffuse irradiance	iance; (C)
Reflected irradiance	44
Figure 6.3 - Total solar irradiance	44
Figure 6.4 - Classified solar irradiance	45
Figure 6.5 - Total insolation time	46
Figure 6.6 - Total daily solar irradiance	46
Figure 7.1 - Spectral emissive power vs wavelength	50
Figure 7.2 - Aerial survey aircraft (CESSNA 4004)	52
Figure 7.3 - Dual Digi-THERM (IGI) thermal system	53
Figure 7.4 - Flight paths for the study: (A) Daytime flight; (B) Nighttime flight	53
Figure 7.5 - GCPs used for georeferencing thermal imagery	56
Figure 7.6 - Daytime temperature	58
Figure 7.7 - Nighttime temperature	58
Figure 7.8 - ΔT (day-night temperature difference)	59
Figure 7.9 - Visual validation of the shading model	60
Figure 8.1 - Temperature distribution: Day vs Night	62
Figure 8.2 - Daytime temperature distribution by soil class	64
Figure 8.3 - Nighttime temperature distribution by soil class	65
Figure 8.4 - ΔT Day-Night distribution by soil class	67
Figure 8.5 - Daytime Temperature: Non-Shadow vs Shadow Areas	69
Figure 8.6 - Daytime temperature distribution by soil class and shadow	70
Figure 8.7 - SVF distribution by soil class	73
Figure 8.8 - Surface temperature distribution by SVF class: (A) Daytime; (B) Night	ttime; and
(C) ΔT	76
Figure 8.9 - Surface temperature distribution by SVF values with linear regre	ssion: (A)
Daytime; (B) Nighttime; (C) ΔT	78
Figure 8.10 - Total solar irradiance distribution by soil class	80
Figure 8 11 - Total solar irradiance distribution by SVF class	82

Figure 8.12 - Daytime temperature distribution by total solar irradiance class	84
Figure 8.13 - Temperature vs Total Solar Irradiance, classified by shading: shadow	and non-
shadow areas	85
Figure 9.1 - Case 1: Temperature-minimising path	87
Figure 9.2 - Case 1: Shadow-maximising path	88
Figure 9.3 - Case 1: Comparison between paths	89
Figure 9.4 - Case 1: Shadow-maximising paths for each hour	90
Figure 9.5 - Case 1: Shaded area proportion and corresponding path distances	90
Figure 9.6 - Case 1: Series of hourly shadow-maximising paths	91
Figure 9.7 - Case 2: Shadow-maximising paths for each hour	93
Figure 9.8 - Case 2: Shaded area proportion and corresponding path distances	93
Figure 9.9 - Case 2: Series of hourly shadow-maximising paths	94

## Acronyms

ANOVA Analysis of Variance

CHM Canopy Height Model

DEM Digital Elevation Model

DTM Digital Terrain Model

DSM Digital Surface Model

EPSG European Petroleum Survey Group

FFT Fast Fourier Transform

GCP Ground Control Point

GHG Greenhouse Gas

GIS Geographic Information System

GNSS Global Navigation Satellite System

GPS Global Positioning System

GRASS Geographic Resources Analysis Support System

HW Heat Wave

HWMI Heat Wave Magnitude Index

IFOV Instantaneous Field of View

IMU Inertial Measurement Unit

IR Infrared

IPCC Intergovernmental Panel on Climate Change

LAS LASer

LiDAR Light Detection and Ranging

LWIR Long-Wave Infrared

MAE Mean Absolute Error

MIR *Mid-Infrared* 

NASA National Aeronautics and Space Administration

NCEI National Centers for Environmental Information

NIR Near-Infrared

NOAA National Oceanic and Atmospheric Administration

NVS Non-Vegetated Surface

nDSM Normalized Digital Surface Model

RMSE Root Mean Square Error

RS Remote Sensing

SD Standard Deviation

SE Standard Error

SNR Signal-to-Noise Ratio

SVF Sky View Factor

SWIR Short-Wave Infrared

UMEP Urban Multi-scale Environmental Predictor

UTM Universal Transverse Mercator

UHI Urban Heat Island

VLWIR Very Long-Wave Infrared

WGS World Geodetic System

WMO World Meteorological Organization

WHO World Health Organization

TIR Thermal Infrared

GLS Generalized Least Squares

IQR Interquartile Range

### 1. Introduction

#### 1.1 Purpose and Scope of the Study

Understanding the dynamics of urban thermal behaviour is becoming increasingly important due to the continuous rise of global temperatures and because of the more frequent and severe heatwaves due to climate change. Urban areas are very vulnerable to the Urban Heat Island (UHI) phenomenon, which occurs when temperatures within the urban fabric are much higher with respect to temperatures experienced in rural areas. The primary goal of this research is to investigate the phenomenon of UHI within a strongly anthropized environment, with a focus on identifying microclimatic variations at a very detailed scale. This is done through high-resolution remote sensing data. The UHI phenomenon is investigated using low altitude aerial surveys, instead of the lower resolution satellite imagery that is often affected by atmospheric noise. The use of LiDAR (Light Detection and Ranging) technology is an essential component of the methodology, and by using the resulting 3D point clouds, very detailed 3D models of the urban fabric are created. These models allow to identify and classify urban features, such as streets, trees and buildings, and also to better understand the spatial distribution of heat. In addition, the study analyses the GIS-based tools estimating solar radiation and shading patterns. Moreover, the Sky View Factor (SVF) provides additional information about urban geometry.

#### The research aims to:

- 1. Identify the areas where the UHI effect is most pronounced by integrating thermal imaging obtained in the thermal infrared spectra during aerial surveys conducted in the daytime and at night, with solar irradiance and shading models;
- 2. Understand how urban materials behave in terms of heat storage and dissipation;
- 3. Determine potential cool spots, such as places that are better shaded by vegetation or constructions and that are less exposed to direct sunlight.

Results aim to help create more resilient cities and safer areas for people that are more vulnerable by suggesting urban development methods that are focused on climate change mitigation and adaptation strategies.

The study is structured into several sections, each focusing on different topics that are all essential for the understanding of the UHI phenomenon and the development of a

vulnerability assessment. The first step involves conducting a climatic analysis using data from a meteorological station near the study area, to provide robust climatological basis for the analysis of UHI. Furthermore, this section is crucial, as the analysis of maximum and minimum temperature trends over that period enables the identification of days classified as heatwaves and nights defined as tropical nights. Then, another section is dedicated to the extraction of digital elevation models, obtained through the processing of data acquired using LiDAR technology. From these data, the land cover class related to tree canopy is extracted, which is then used as a soil type in the land use map. An important section is the GIS analysis, which uses the previously obtained elevation models to identify and model shaded areas, the SVF, and solar irradiance over the study area. All this information, together with the section dedicated to the acquisition and analysis of thermal images, is integrated into the statistical analysis, which represents the core of the work. This phase provides fundamental information on the behaviour of the urban fabric during a heatwave. Finally, the last section focuses on the assessment of urban heat vulnerability during heatwaves using a dynamic route optimisation approach. The model considers temperature and shading to identify routes with higher thermal comfort and areas most exposed to heat, providing useful suggestions for urban planning. The entire methodology is summarised in the diagram below (Figure 1.1).

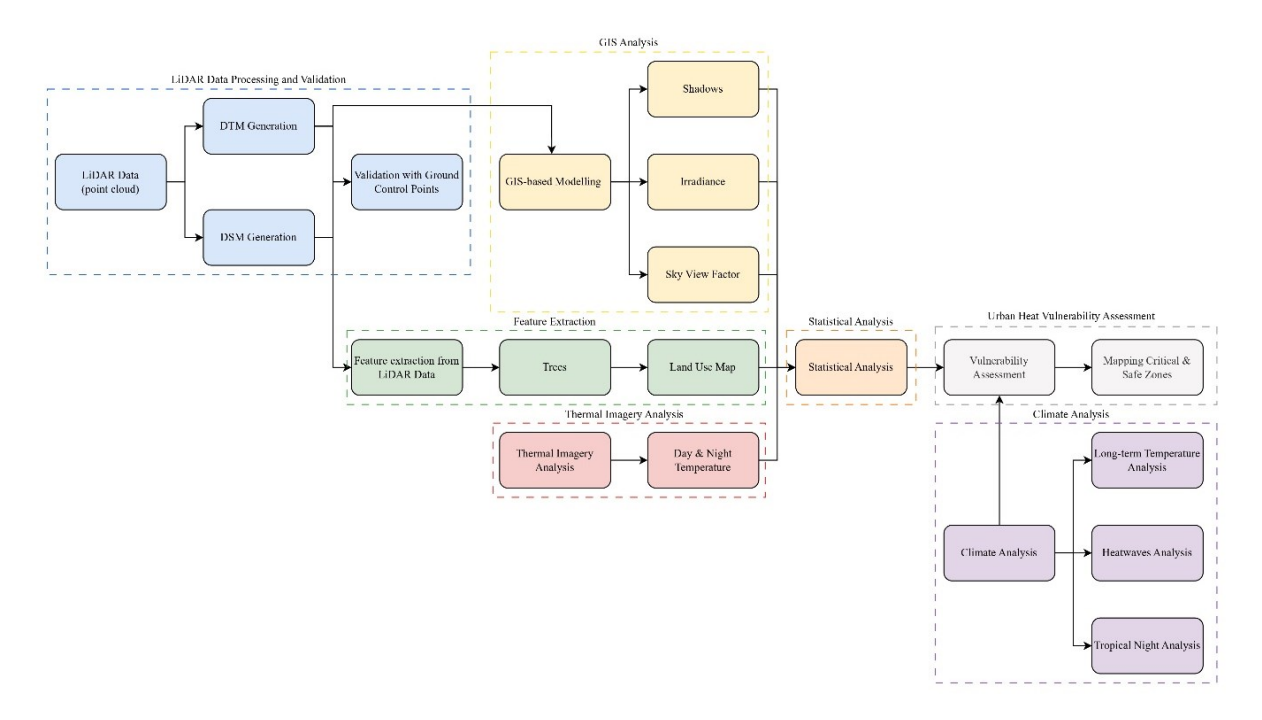


Figure 1.1 - Methodological framework

#### 1.2 Study Area

The study corresponds to a part of District 6, which is in the northeastern part of the city of Turin, in Italy. With a total surface of about 2.000 km², the area lies between the neighbourhoods of Regio Parco and Barriera di Milano, which exhibit significant socio-cultural complexity and human landscape alteration. The study area is shown in Figure 1.2. The existence of earlier studies and data that can be examined and integrated with the information collected during this investigation supports the choice of this area.

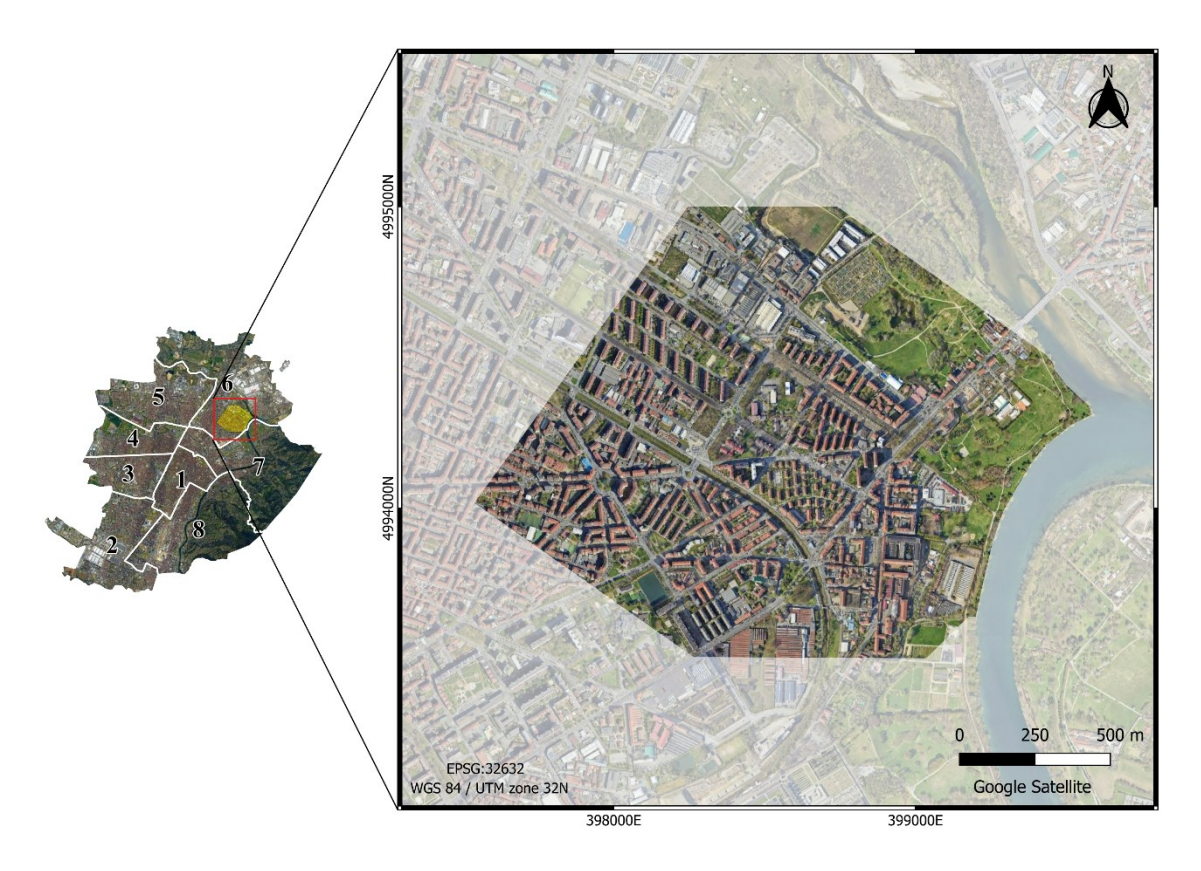


Figure 1.2 - Study area: a section of District 6 in Turin

The study area is characterised by strong landscape heterogeneity. It mostly includes impermeable urban elements such as asphalt and concrete, as well as residential areas and industrial buildings with roofs that facilitate heat retention and contribute to overheating of the area, especially during the summer season. Moreover, in the area it is possible to notice the limited presence of green spaces with adequate vegetation capable of providing shelter from direct sunlight during the hottest days. This may have a negative impact on the ability of these green areas to mitigate the effects of climate change and to reduce the effects of the

UHI. Furthermore, the social characteristics of the area make it even more vulnerable to the potential risks resulting from heatwaves and heat stress. For this reason, it is essential to study and investigate the vulnerability of these regions in order to encourage the development of new strategies to counteract the impact of UHIs.

#### 2. Heatwayes and Urban Heat Islands

# 2.1 Overview of Climate Change, Heatwaves, and Urban Heat Islands

Climate change is one of the most pressing global challenges of the 21st century (Feulner, 2015). According to WMO, it refers to a long-term change in the state of the climate that can be identified by changes in the mean and/or the variability of its properties. The current changes in climate are primarily caused by increased concentrations of greenhouse gases (GHGs) in the atmosphere since the Industrial Revolution due to human activities (IPCC, 2013) such as the combustion of fossil fuels (coal, oil and gas), deforestation, land use change, increasing livestock farming, agricultural activities, etc. (IPCC, 2018). These gases trap heat from the sun, leading to a rise in average global temperatures (United Nations, n.d.). The consequences of climate change are very serious and can be seen in natural, social and business threats (European Commission & Directorate-General for Climate Action, n.d.), impacting ecosystems, weather patterns, sea levels, and human societies (EEA, 2025). The Sixth Assessment Report of the IPCC (2023) states that hot extremes, including heatwaves, have become more frequent and intense since the 1950s across most regions of the world, due to human-caused climate change. Heatwaves are defined as "prolonged period of muchwarmer-than-average weather" (Copernicus, 2024). Although there is no universally accepted definition of a heatwave, several criteria and thresholds have been proposed and tested in the scientific literature. These extreme heat events have become more common globally and they pose risks to ecosystems and human health (WMO, 2023). Temperatures in Europe are warming twice as fast as the global average, with 2024 recorded as the hottest year (World Meteorological Organization & European Union, 2025). Moreover, the warmest 10 years experienced by the region have been since 2007, in particular the last 3 years have been the warmest on record. In fact, 19 of the 23 most severe European heatwaves since 1950 have occurred since 2000 (WHO, 2025). Heatwave's risks are particularly pronounced in urban environments, where the combination of climate change and city characteristics creates what is known as the Urban Heat Island (UHI) effect. Moreover, urban population exposure to extreme heat has strongly increased in recent decades due to both climate change and rapid urbanisation (Tuholske et al., 2021). WMO defines urban climate as local climate that is modified by interactions between the built-up area and regional climate. The UHI effect

results from interactions between the urban environment and atmospheric processes, leading to elevated temperatures in cities compared to surrounding rural areas (Collier, 2006; Santamouris, 2015). Oke (1982) provided an analysis of the energetic mechanisms driving this phenomenon. This analysis shows how changes in surface properties and energy fluxes contribute to urban warming. This effect arises in urban environments due to factors such as vegetation cover, season, extent of built-up areas, time of day, population density, the presence of water bodies, and other variables (Deilami et al., 2018). Urban surfaces absorb and retain more heat than surrounding rural surfaces. Materials commonly used in cities, such as asphalt, concrete, bricks, and roofing tiles, have low albedo and high thermal mass, meaning they absorb solar radiation during the day and release it slowly at night, keeping urban areas warmer (Vujovic et al., 2021). This temperature difference worsens the health risks associated with heatwaves, especially for vulnerable populations including the elderly, young children, people with pre-existing medical conditions, and those living in low-income neighbourhoods with limited access to cooling infrastructure (Harlan et al., 2006), by increasing the incidence of heat exhaustion, heat stroke, cardiovascular diseases, and respiratory illnesses (van Daalen et al., 2024). HWs combined with UHIs have been linked to spikes in mortality rates during hot seasons in many cities worldwide. Numerous epidemiological studies have demonstrated the adverse effects of high temperatures on human health. For instance, Baccini et al. (2008) and Oudin Aström et al. (2015) conducted comprehensive analysis across different European cities and found that elevated heat levels were associated with an increase in mortality rates. Heatwave-related mortality in the European Region is estimated to have increased by over 30% in the past 20 years, with more than 61,000 heat-related deaths recorded in 2022. That year, Italy was the most affected country, accounting for almost 18,000 of these deaths (Ballester et al., 2023). In 2023, the number of heat-related deaths was 47,000 (WHO, 2025). A particularly concerning aspect of urban heat stress is the occurrence of hot nights, where minimum temperatures remain high. Normally, nighttime temperatures provide relief from daytime heat. However, in urban areas affected by the UHI effect, the retention of heat prevents this natural cooling, prolonging heat exposure (Possega et al., 2022). As a result, urbanisation contributes to the increase in nighttime temperature extremes (Schatz & Kucharik, 2015; Sun et al., 2019). This heat stress can impact sleep and cognitive function, and increase the risk of heat-related illnesses. This means that hot nights significantly worsen the health impact of heatwaves (Buguet et al., 2023).

#### 2.2 Climate Analysis

For a comprehensive understanding of temperature dynamics, and thus of the impact of heatwaves, it is essential to establish the foundations of a climatic study that describes the long-term behaviour of temperatures in the area. In particular, to ensure statistical robustness, it is required a temporal baseline of at least 30 years of continuous temperature observations. The meteorological data used in this study are obtained from the National Centers for Environmental Information (NCEI) of NOAA. Among the four available weather stations surrounding the Turin area (Torino Caselle, Torino Venaria, Torino Bric Croce, and Aeritalia Torino) the Torino Caselle station was selected. This station is managed by ENAV and is located within the Turin-Caselle airport area at 287 meters above sea level (45°11′30.65″N, 7°39′02.39″E), and it is approximately 11 km far from the study area (Figure 2.1). This choice is motivated by the station's dataset, which allows for the reconstruction of a 30-year baseline with consistent daily records.

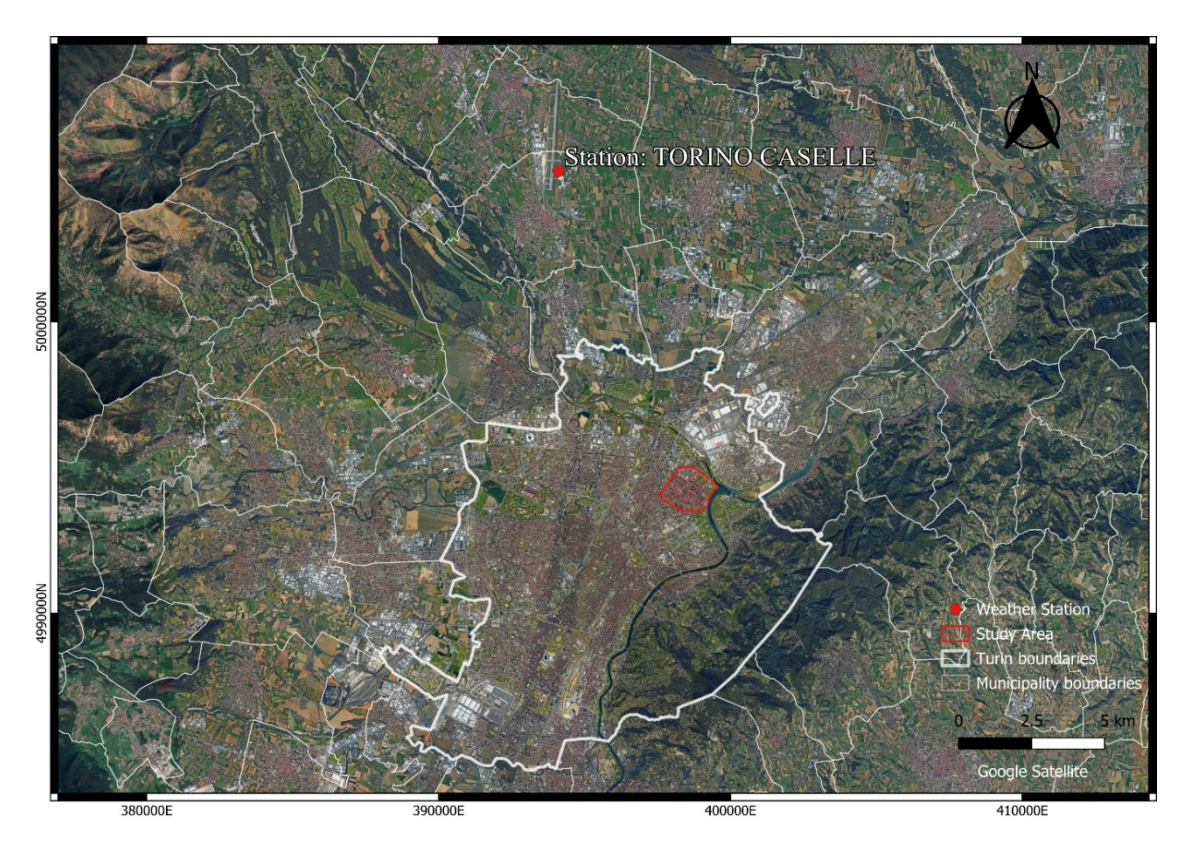


Figure 2.1 - Location of Torino Caselle weather station

#### 2.2.1 Long-term Temperature Analysis

The first phase of the climatic analysis focuses on detecting the existence of a trend in the daily maximum and minimum temperatures recorded at the station between January 1995 and December 2024. After an initial cleaning phase, gaps in the data are identified. These gaps are filled to maintain temporal continuity using the long-term daily mean, corresponding to the 30-year average of maximum or minimum daily temperatures. Once the gaps are filled, the seasonality is removed in order to extract a clear temperature trend. To remove this seasonality, a spectral analysis is performed by applying a Fast Fourier Transform (FFT), which converts the series from the time domain into the frequency domain. The FFT produces both amplitude and phase spectra, from which the three main harmonic components can be identified:

- First harmonic: reflects the annual oscillation;
- Second harmonic: reflects the seasonal cycle;
- Third harmonic: adjusts the shape.

By combining the first three harmonic components with their corresponding amplitudes and phases, the Periodic Component (PC) is reconstructed. The Periodic Component can be expressed as:

$$PC = A_1 \cos(2\pi f_1 + \phi_1) + A_2 \cos(2\pi f_2 + \phi_2) + A_3 \cos(2\pi f_3 + \phi_3)$$
 (Eq. 2.1)

Where:

- $A_1$ ,  $A_2$ ,  $A_3$  are the amplitudes of the first, second, and third harmonic components;
- $\phi_1, \phi_2, \phi_3$  are the phase shifts of the first, second, and third harmonics;
- $f_1, f_2, f_3$  are the frequencies of the first, second, and third harmonics:

$$o f_1 = \frac{1}{366} \text{ cycles/day}$$

$$o f_2 = \frac{2}{366} \text{ cycles/day}$$

$$f_3 = \frac{3}{366}$$
 cycles/day

The value 366 is used instead of 365.25 because in the dataset all years include February 29th. In non-leap years this day is recorded as "no data."

Harmonic components are typically centred around zero, but in this study they are adjusted using the mean of the observed temperatures to centre the harmonics relative to the actual temperature trend. Then, residuals are obtained by subtracting this periodic model from the gap-filled series. Finally, a linear regression is applied to the residuals to verify the existence of a temperature trend. The trends for maximum and minimum daily temperatures are shown in Figure 2.2.

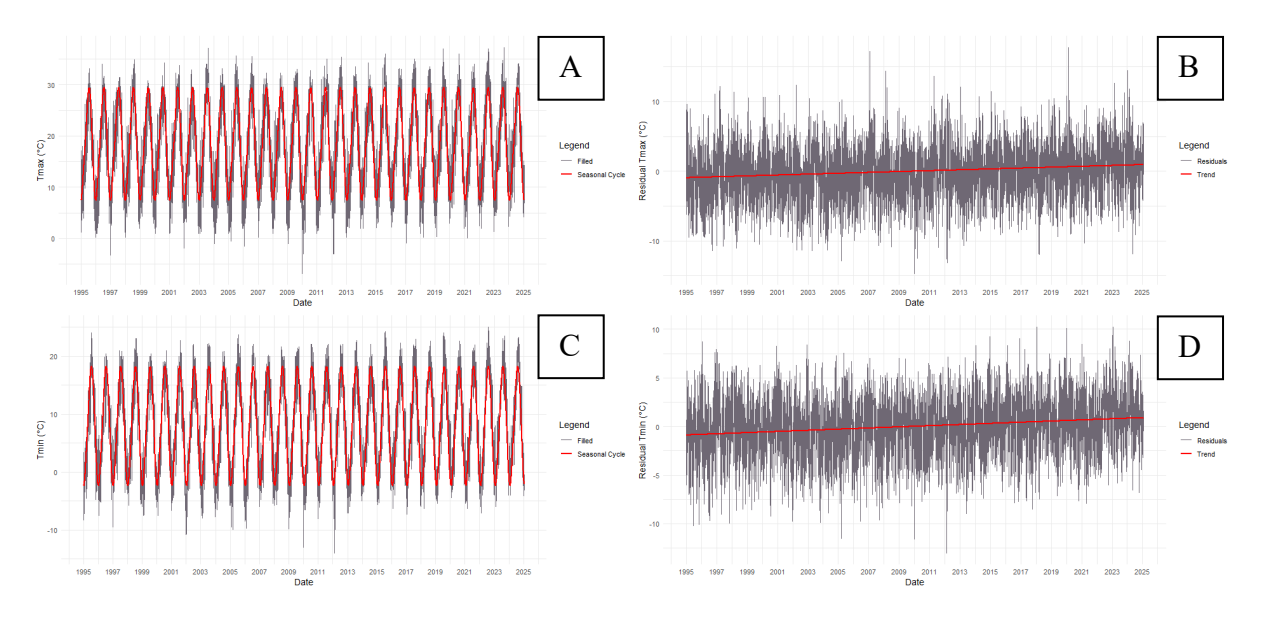


Figure 2.2 - Maximum and minimum temperatures from 1st January 1995 to 31st December 2024: (A) Maximum temperatures; (B) Residuals of maximum temperatures; (C) Minimum temperatures; (D) Residuals of minimum temperatures

Results of the linear regression on the residuals are presented in Table 2.1 and show a warming trend in both cases. Maximum daily temperatures show an increase of +0.063 °C/year, while minimum daily temperatures show an increase of +0.060 °C/year. The p-values confirm that these trends are highly statistically significant.

Table 2.1 - Regression results on residuals of daily maximum and minimum temperatures

Temperature	Intercept	Slope Daily	Slope Annual	p-value
Tmax	-0.939	0.000171	0.0626	6.522e-56 ***
Tmin	-0.893	0.000163	0.0595	2.238e-77 ***

#### 2.2.2 Heatwaves Analysis

In this section, the presence and characteristics of HWs in Turin are analysed using temperature data from the Torino Caselle station from 1st January 1995, to 24th August 2025. HW days were identified using the Heat Wave Magnitude Index (HWMI), which quantifies the maximum magnitude of HWs within a given year. In this case, a HW is defined as a period of at least three consecutive days during which daily maximum temperatures exceed the threshold determined for the reference period (1995-2025). The threshold corresponds to the 90th percentile of daily maximum temperatures, calculated within a centred 31-day moving window (Russo et al., 2014):

$$A_d = \bigcup_{y=1995}^{2025} \bigcup_{i=day-15}^{day+15} T_{y,i}$$
 (Eq. 2.2)

Where:

- $A_d$  is the threshold;
- U is the union of datasets;
- $T_y$  is the daily  $T_{max}$  of the year y and the day i.

The same criterion is applied in previous UHI studies, such as Todeschi et al. (2022). Days that exceed the 90th percentile but do not occur in a sequence of at least three consecutive days are classified as "hot days." For each year, the duration and frequency of HWs, the number of HWs during the summer months (June to September) and the total number of hot days are found. For 2025, data are analysed only up to 24th August. Data from 25th August to 30th September are treated as "no data". So, the number of hot days and HWs during the reference period may be underestimated, as potential events occurring in late August and September are not included. The results are presented in Figure 2.3.

Results in Figure 2.4 show how the total number of hot days and HW days increased significantly from 1995 to 2025. It is interesting that starting from 2014, every subsequent year experienced at least one HW.

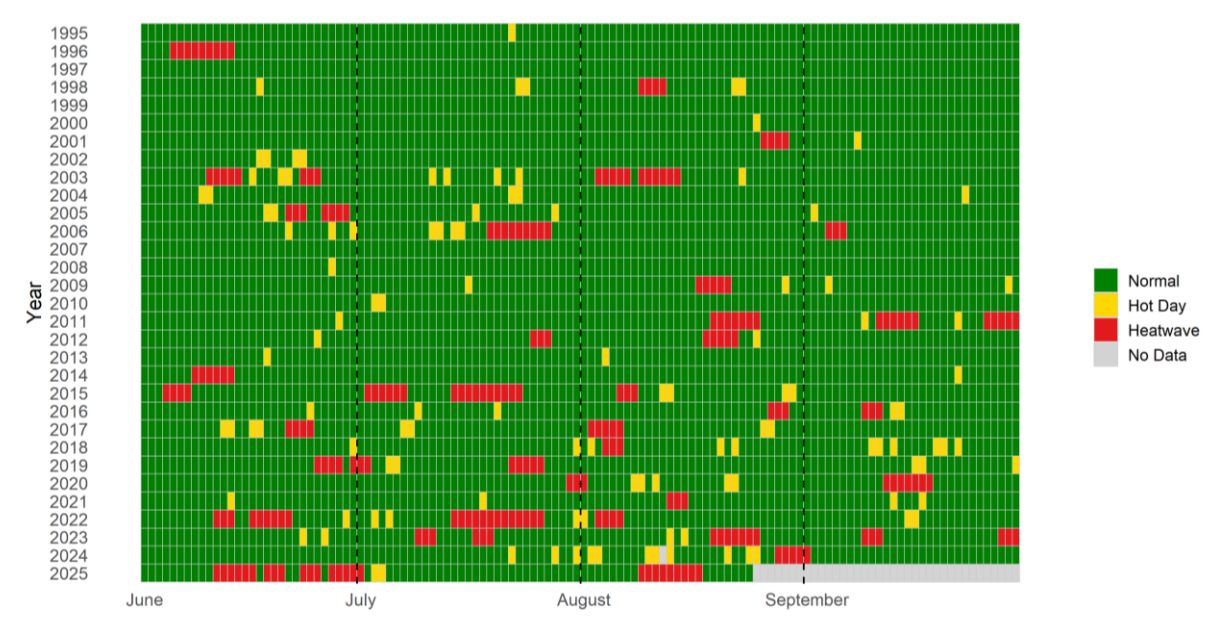


Figure 2.3 - Daily classification: heatwaves, hot days, and no data

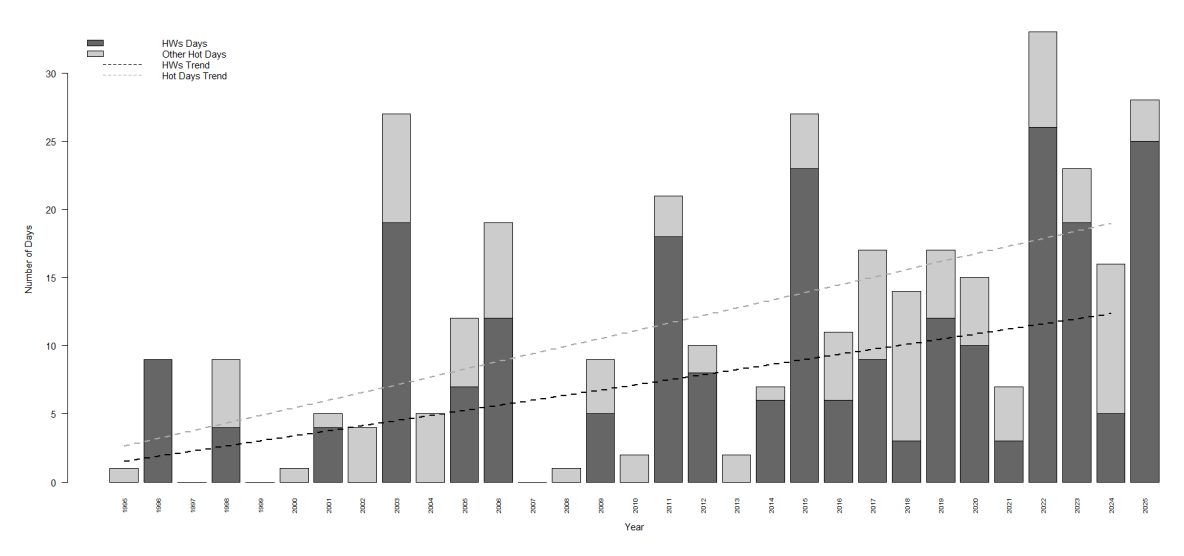


Figure 2.4 - Annual frequency of hot days and HWS with trend lines

The linear regression applied to the period 1995-2024 shows a statistically significant positive trend (Table 2.2). The trend shows that HW days are increasing by +0.37 days per year, while total hot days are increasing by +0.56 days per year.

Table 2.2 - Linear regression results of HW and hot days

Variable	Intercept	Slope (days/year)	$R^2$	p-value
HW Days	-743.220	0.373	0.191	0.0159 *
Total Hot Days	-1121.136	0.563	0.295	0.00192 **

#### 2.2.3 Tropical Nights Analysis

Minimum temperatures have proved to be very important in determining the presence of tropical nights in Turin. The definition of a tropical night varies depending on the geographical area that is considered. In European countries, a night is defined as tropical when the minimum recorded temperatures do not fall below 20 °C (Copernicus, 2025).

By setting a threshold of 20 °C, the series of minimum temperatures from 1995 to 2025 was analysed, considering the months from June to September. The results are shown in Figure 2.5.

Through the linear regression of the data shown in Figure 2.6, it is possible to see the positive trend present in the series. The results are shown in Table 2.3. Specifically, the trend of increase in the number of tropical nights is highly statistically significant, with an average increase of about +0.63 tropical nights per year. The results are consistent with the trend of minimum temperatures in the same region.

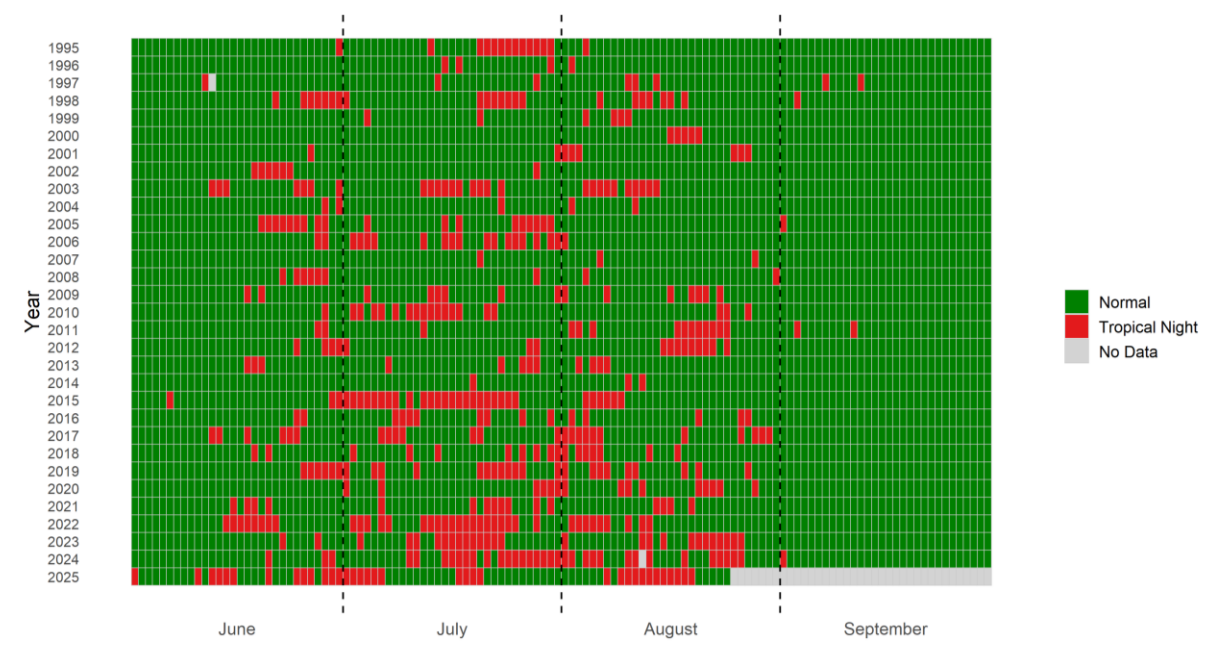


Figure 2.5 - Daily distribution of tropical nights

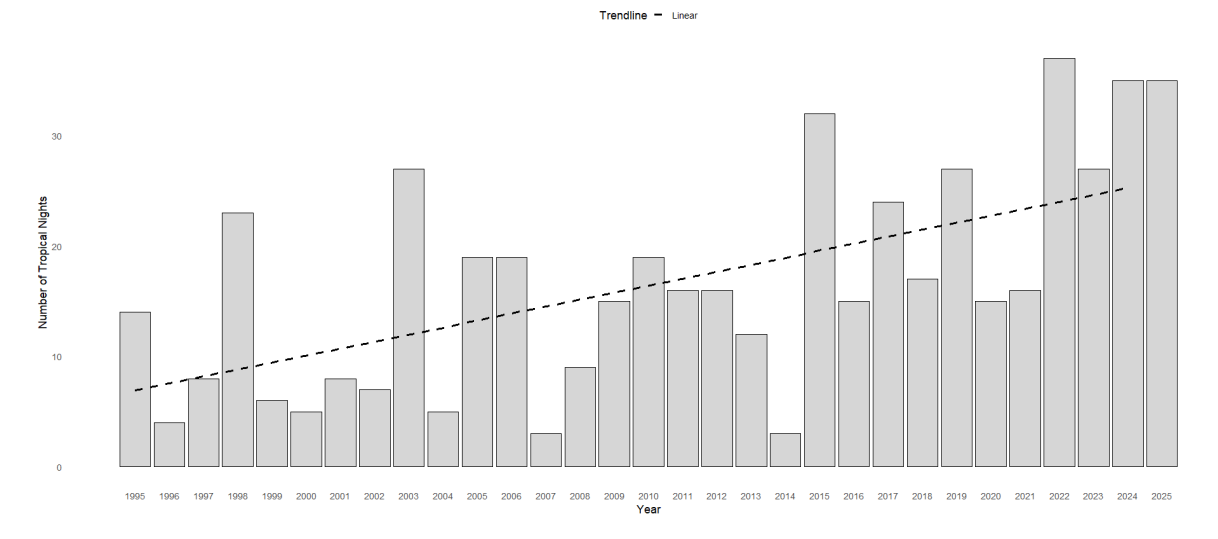


Figure 2.6 - Annual frequency of tropical nights with trend line

Table 2.3 - Linear regression results of tropical nights

Intercept	Slope (nights/year)	$R^2$	p-value
-1256.658	0.633	0.338	0.000752 ***

## 3. LiDAR Technology

#### 3.1 Overview of LiDAR

Understanding and mitigating the effects of the UHI effect requires a complete knowledge of the city's physical configuration, including building geometry, vegetation cover and the types of materials of surfaces. One of the most effective technologies for obtaining this level of detailed spatial information is LiDAR (Light Detection and Ranging). LiDAR is an active remote sensing method which uses laser pulses to measure distances from a sensor to surfaces on the Earth. These pulses are emitted from a transmitter and bounce back from surfaces, to be captured by a receiver that then translates them into electrical signals (Wasser, 2024). This process allows for the creation of high-resolution 3D point clouds, which enable the generation of digital elevation models (DEMs).

LiDAR systems are implemented across different platforms, each specialised to specific applications and environments (Mehendale & Neoge, 2020):

- Airborne LiDAR: installed on aircraft or helicopter, used in topographic mapping, forestry, and environmental monitoring due to its efficiency in capturing broad-scale information. It has two subtypes:
  - Topographic LiDAR: used in forestry, urban planning, environmental monitoring, etc.
  - Bathymetric LiDAR: used to map underwater areas near coastlines, shores, and banks.
- Terrestrial LiDAR: used to survey highways and railways, urban mapping, manage facilities, create 3D models for spaces, etc. It has two subtypes:
  - Mobile LiDAR: mounted on moving platforms such as cars, boats, or trains. It
    is used to analyse road infrastructure, locate incoming road signs, light poles,
    etc.
  - o Static LiDAR: used in engineering, archaeology, mining, and surveying.

Regardless of the platform, all LiDAR systems rely on some core components (Lohani & Ghosh, 2017):

- LiDAR sensors: the laser scanner is used to generate short-width laser pulses, transmit them toward the ground, scan the ground below while transmitting pulses, and the photodetector receives the return signal. By measuring the time it takes for each pulse to return, the system calculates the distance to the surface;
- GNSS receiver: the GNSS unit mounted on the aircraft works in tandem with a ground-based GNSS base station receiver and observes the 3D position of the aircraft at each epoch of GNSS observation;
- IMU sensor: the Inertial Measurement Unit (IMU) records the accelerations and orientations of the aircraft using accelerometers and gyroscopes.
- Onboard computer: timestamps the different data produced by the above sensors using the GNSS time and archives raw data;
- Digital camera: it is common to also have a medium format digital camera along with the LiDAR sensor, as it provides colour information of the terrain, offering additional useful information.

The fundamental principle behind a LiDAR system is the time-of-flight method obtained through light reflection. The emitted pulse travels at a very high speed, corresponding to the speed of light. Since this speed is known, it is possible to compute the following formula to retrieve the distance (Mehendale & Neoge, 2020):

$$Distance = \frac{c\Delta t}{2}$$
 (Eq. 3.1)

Where:

- c is the speed of light;
- $\Delta t$  is the time the laser pulse took to go and come back to the sensor.

By repeating this process hundreds of thousands of times per second, it is possible to obtain a very detailed point cloud representing points acquired on the surface, each one corresponding to a precise position in space. These points also contain additional metadata, such as GPS timestamp, intensity, scan angle, return angle, and type of classification. These data are usually stored using a standardised file structure, the LAS file format. Figure 3.1 illustrates the airborne LiDAR survey system.

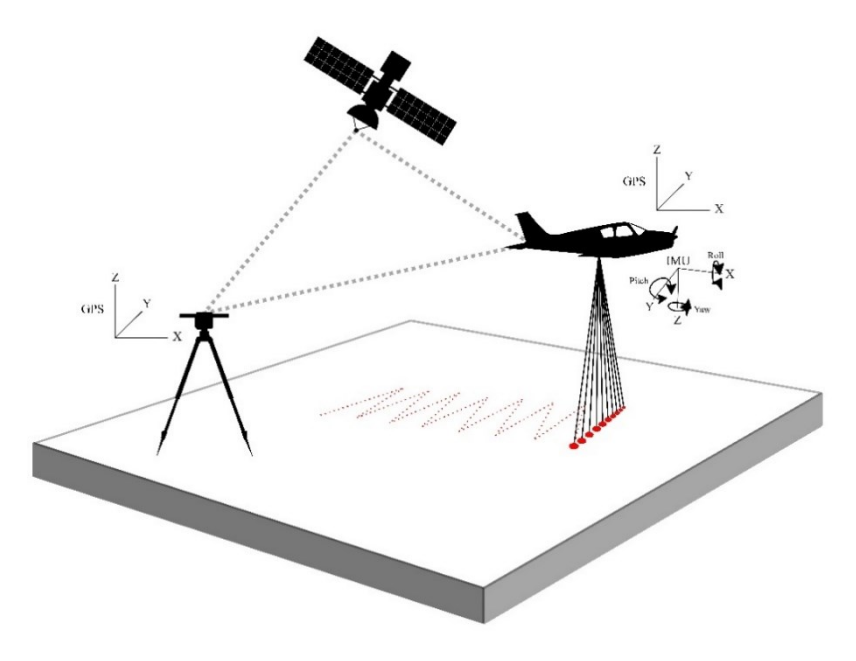


Figure 3.1 - Schematic of the airborne survey system

#### 3.1.1 Laser Properties

The laser properties of the LiDAR system are fundamental. The beam divergence refers to how much the laser beam spreads as it travels, influencing the laser footprint size on the ground and the system's spatial resolution, with a smaller footprint providing higher-resolution data. The relationship between flight height (h), beam divergence ( $\gamma$ ), and footprint diameter ( $A_L$ ) is given by Baltsavias (1999):

$$A_L = h\gamma \tag{Eq. 3.2}$$

Another critical property is intensity, defined as the ratio of strength of reflected light to that of emitted light. Intensity is not a function of the laser itself. It depends on the reflectance of the target surface. Surfaces with higher reflectance or perpendicular angles of incidence return more energy, which improves the detectability of features in the data. Intensities are in fact useful information for classifying land cover in LiDAR data (Song et al., 2002). The intensity usually produces a grey scale pseudo-ortho from just the LiDAR data itself.

Finally, the pulse rate, the scan rate and the platform's speed determine the density of the point cloud.

Moreover, two other factors that strongly influence and determine data reliability are accuracy and resolution. The study by Passalacqua et al. (2015) provides typical values for airborne LiDAR systems, as reported in Table 3.1. Resolution refers to the number of points

acquired per square meter, and higher densities correspond to more detailed representations of terrain features. Vertical and horizontal accuracy refer to terrain elevation and planimetric position, respectively (ASPRS, 2004).

Table 3.1 - Typical specifications of airborne LiDAR systems

Spatial extent (km²)	Typical point density (pts/m²)	Best georeferenced or measurement accuracy (vert/horiz) (m)	Smallest footprint (m)
10 - 100s	1 - 100	0.05 / 0.2 - 0.2 / 0.6	0.1 - 1

#### 3.2 LiDAR Data Processing and Products

Before being used, the raw data recorded by LiDAR acquisitions undergo a series of processes.

The first step is pre-processing, where the raw data are georeferenced using the values recorded by the onboard GNSS and IMU systems. In this step, the data are also calibrated to improve accuracy and correct for any errors and cleaned of external noises.

Once the pre-processing and data cleaning phase is done, the classification phase begins, where each data point is assigned a specific category.

Once classified, the LiDAR data can be used to generate different results. Among the most important results is the Digital Elevation Model (DEM), a 3D model representing the Earth's surface, including the Digital Terrain Model (DTM) and the Digital Surface Model (DSM) (Manune, 2007). The DTM represents the terrain surface, excluding points characterizing features such as buildings and vegetation (Figure 3.2A). The DSM represents the Earth's external surface, including elements such as buildings and vegetation (Figure 3.2B). Another variant is the Non-Vegetated Surface (NVS), that represents a DSM that includes only human structures and buildings (Figure 3.2C) (Guth et al., 2021).

These models lay the foundation for the creation of secondary models, derived to extract more detailed information and features (Guth et al., 2021). For example, the normalised DSM (nDSM) is calculated by subtracting the DTM from the DSM, and the result provides a model representing the heights of objects above ground level. The Canopy Height Model (CHM)

represents the vegetation height by subtracting the NVS from the DSM, offering a model for studying urban greenery or forest areas (Croneborg et al., 2020).

As documented in recent publications, these acquisitions are very useful for monitoring infrastructure and vegetation as well as analysing urban morphology (Takhtkeshha et al., 2024). In the context of urban HWs, LiDAR data enables the extraction of 3D models of the urban fabric, capturing elements such as building heights and shapes, urban canyons, and other factors that influence heat distribution. It is also useful for mapping green spaces and urban parks, which are increasingly essential for contrasting the effects heatwaves through shade and evapotranspiration (Hofierka et al., 2017; Pyszny et al., 2020). Moreover, when combined with thermal imagery, LiDAR data also enables the visualisation of heat distribution on the urban fabric, helping to identify hotspot and cool spot areas and serving as a basis for determining mitigation strategies (Mandanici et al., 2016).

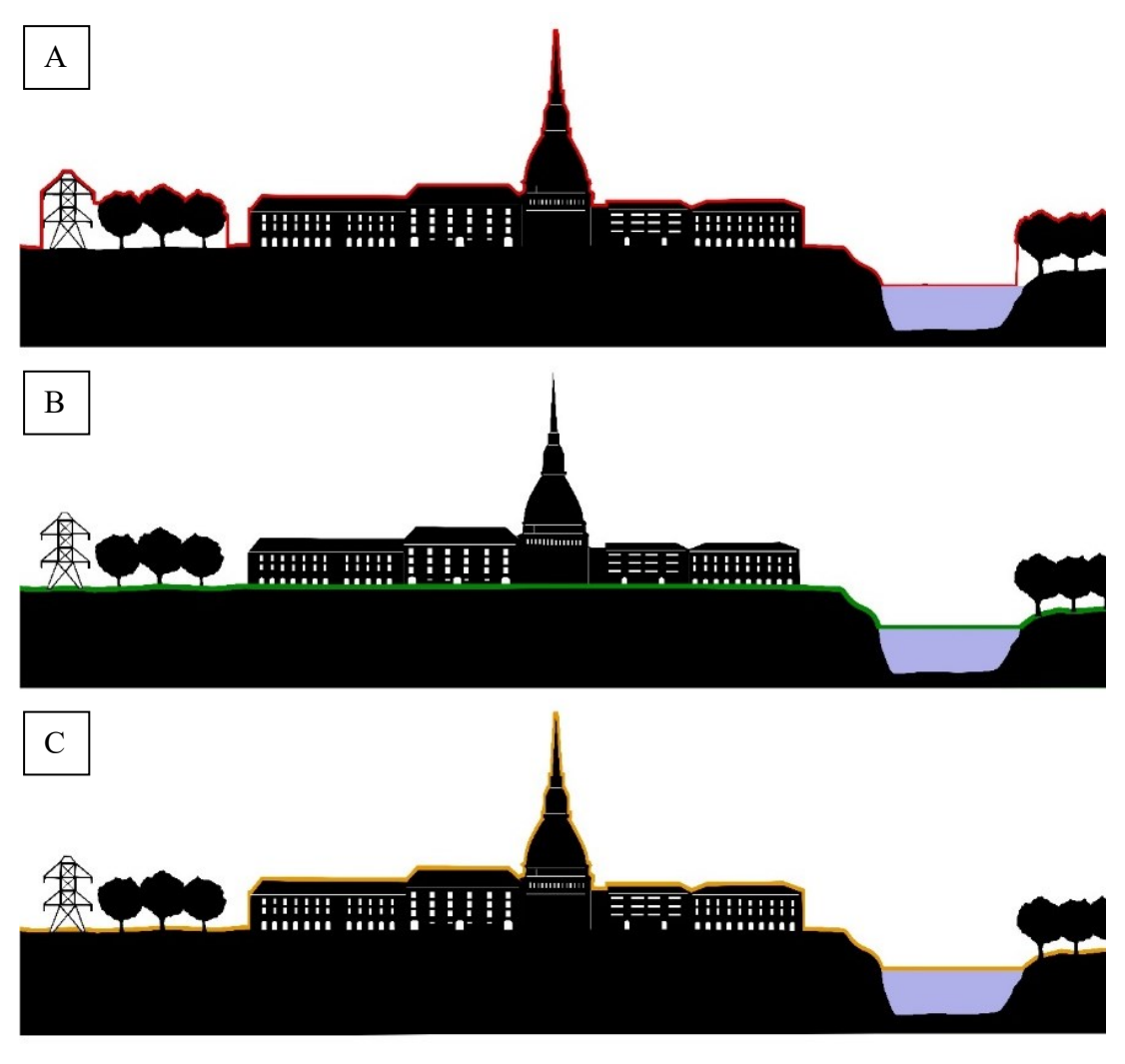


Figure 3.2 - (A) Digital Surface Model (DSM); (B) Digital Terrain Model (DTM); (C) Non-Vegetated Surface (NVS)

#### 3.2.1 LiDAR Data Processing and Validation

To implement the general workflow described in Section 3.2, it was used LiDAR data acquired by the Politecnico di Torino in 2022. The files containing the point clouds are in LAS file format. There are 15 files, each covering an area of 0.25 km<sup>2</sup>, for a total investigated surface of 3.75 km<sup>2</sup> and a total of 106,401,261 acquired points. The LAS point cloud is georeferenced using the EPSG:32632 (WGS 84 / UTM Zone 32N) coordinate reference system, as specified in the file metadata. The characteristics of each used file are shown in Table 3.2. The acquisitions used a nadir-oriented sensor, directing laser pulses vertically downward. By processing these data in a GIS environment, specifically using ENVI LiDAR 6.1 software, it is possible to obtain useful outputs, including DTM, DSM, and orthophoto of the area. The resulting rasters are then clipped to the study area initially described, covering approximately 54% of the surface analysed by the LiDAR survey. Figure 3.3 highlights complementary attributes of the point cloud in a portion of the study area. Specifically, Figure 3.3A shows the dataset in RGB (true colour), providing a representation of buildings, roads, and vegetation. Figure 3.3B shows the elevation of points. Figure 3.3C shows automatic point classification. Only ground points have been classified, which are fundamental for generating the Digital Terrain Model (DTM), while the remaining unclassified points (mainly buildings and vegetation) provide the basis for generating the Digital Surface Model (DSM). Finally, Figure 3.3D displays LiDAR intensity in grayscale. The resulting DSM and DTM (Figure 3.4 and Figure 3.5) are generated at a high spatial resolution of 1 m/pixel and serve as input for subsequent analysis steps.

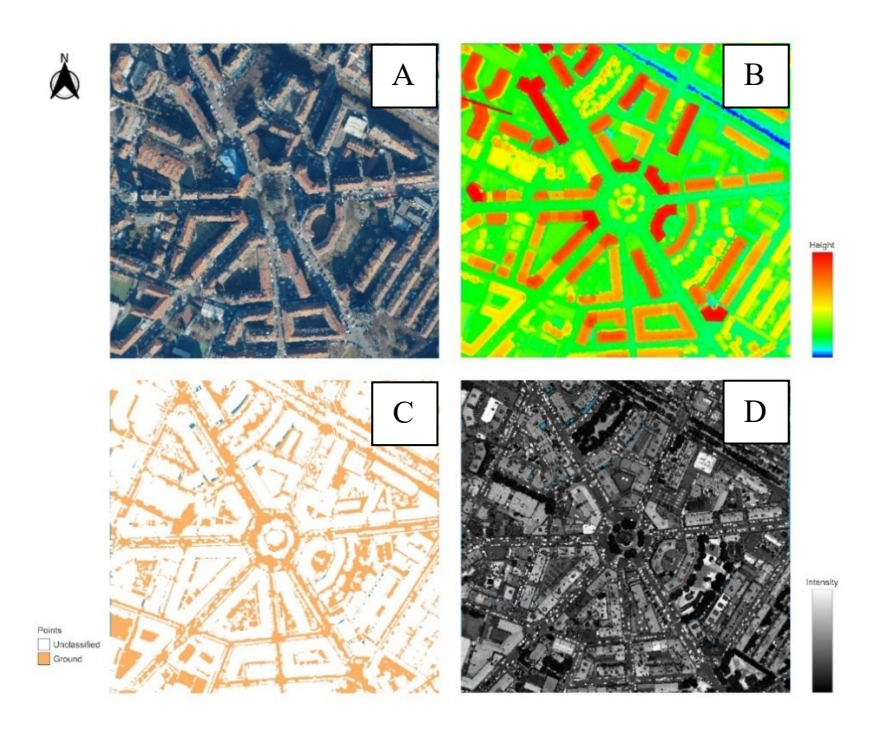


Figure 3.3 - Complementary attributes of the LiDAR point cloud in a portion of the study area. (A) True colour RGB; (B) Point elevation; (C) Automatic point classification; (D) LiDAR intensity

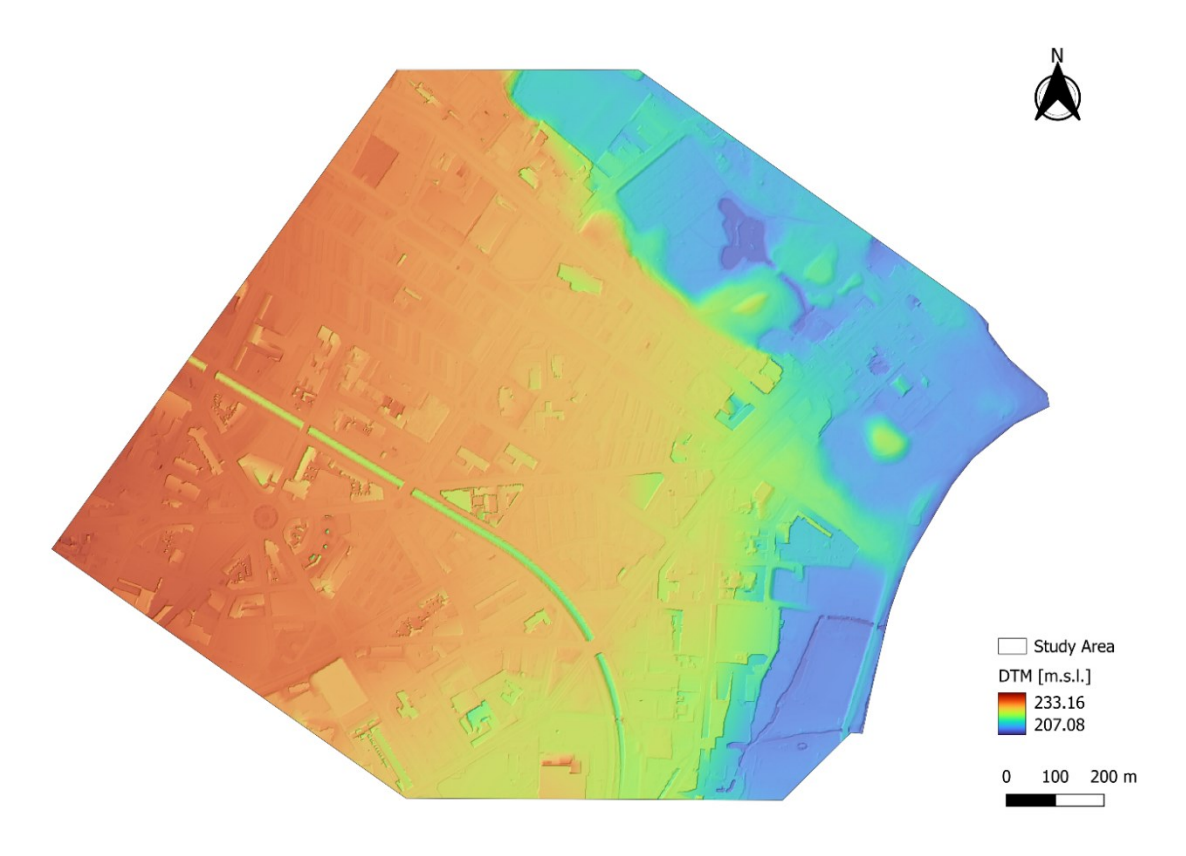


Figure 3.4 - Digital Terrain Model (DTM) of the study area

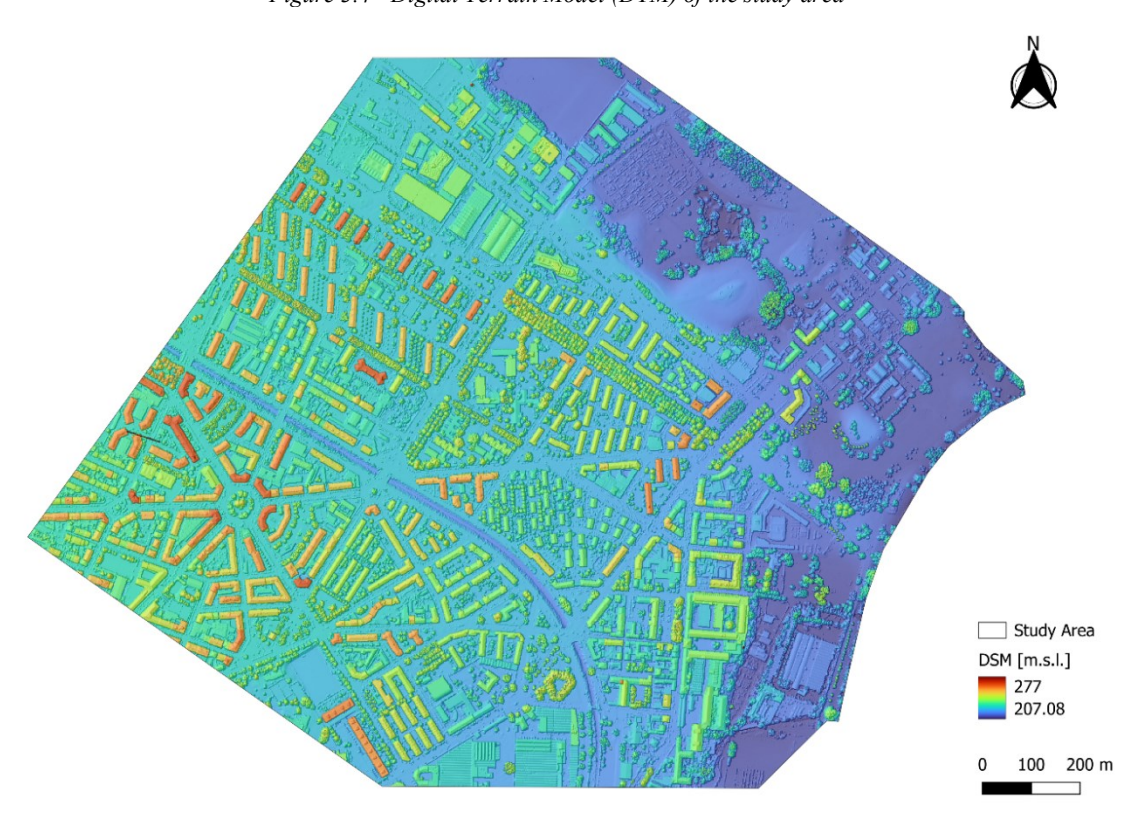


Figure 3.5 - Digital Surface Model (DSM) of the study area

Table 3.2 - Summary of LiDAR point cloud files used in the study

	32_399500_ 4994500.las	32_397500_ 4993500.las	32_397500_ 4994000.las	32_397500_ 4994500.las	32_398000_ 4993500.las
Xmin	399500	397500	397500	397500	398000
Xmax	400000	398000	398000	398000	398500
Ymin	4994500	4993500	4994000	4994500	4993500
Ymax	4995000	4994000	4994500	4995000	4994000
Zmin [m.s.l]	207.797	220.285	221.363	222.896	217.156
Zmax [m.s.l]	248.162	268.916	278.512	281.22	267.243
DX[m]	499.998	499.998	499.999	499.999	499.998
DY[m]	499.997	499.998	499.999	499.999	499.998
DZ[m]	40.365	48.631	57.149	58.324	50.087
$N^{\circ}$ Points	7456073	7760433	7413074	7900047	7228035
	32_398000_ 4994000.las	32_398000_ 4994500.las	32_398500_ 4993500.las	32_398500_ 4994000.las	32_398500_ 4994500.las
Xmin	398000	398000	398500	398500	398500
Xmax	398500	398500	399000	399000	399000
Ymin	4994000	4994500	4993500	4994000	4994500
Ymax	4994500	4995000	4994000	4994500	4995000
Zmin [m.s.l]	218.008	214.567	209.81	212.75	209.84
Zmax [m.s.l]	269.177	269.814	258.906	266.239	254.479
DX[m]	499.998	499.999	499.998	499.998	499.998
DY[m]	499.999	499.999	499.999	499.999	499.999
DZ[m]	51.169	55.247	49.096	53.489	44.639
$N^{\circ}$ Points	7611386	7211955	7611650	7715762	7264767
	32_399000_ 4993500.las	32_399000_ 4994000.las	32_399000_ 4994500.las	32_399500_ 4993500.las	32_399500_ 4994000.las
Xmin	399000	399000	399000	399500	399500
Xmax	399500	399500	399500	400000	400000
Ymin	4993500	4994000	4994500	4993500	4994000
Ymax	4994000	4994500	4995000	4994000	4994500
Zmin [m.s.l]	209.023	209.22	209.1	208	206.923
Zmax [m.s.l]	279.896	250.441	257.915	252.765	249.643
DX[m]	499.998	499.998	499.998	499.999	499.998
DY[m]	499.999	499.998	499.998	499.999	499.998
DZ[m]	70.873	41.221	48.815	44.765	42.72
N° Points	6207252	6747651	6388841	8831150	3053185

### 3.2.2 Validation with Ground Control Points

Before the model is used, it is essential to perform a data validation process to ensure the dataset's accuracy and reliability. This step is critical because even small positional or elevation errors in LiDAR-derived models can propagate through subsequent analyses, leading to inaccurate results. The validation process in this study compares the LiDARderived model with a set of reliable ground control points (GCPs). These GCPs are obtained from the Geoportal of the Piedmont Region (Geoportale Regione Piemonte) and correspond to geodetic benchmarks whose positions and elevations are determined through precise geomatic surveys. Each benchmark includes an elevation value expressed in meters above sea level. These points help identifying and quantifying any error present in the model. Within the defined study area, a total of 233 points is initially identified after filtering out those with incomplete or invalid elevation data. An additional filtering step removes GCPs located on building roofs and under vegetation, as these elevated surfaces can distort ground elevation measurements. Polygons representing volumetric building units are obtained from the Geoportal of the Piedmont Region and used as spatial masks to exclude all GCPs on building surfaces. For vegetation, a manual visual approach is used to remove points. In total, 91 points are removed after applying both building roof and vegetation filters, leaving 142 ground-level points suitable for validation (Figure 3.6). The elevation values from these points are then compared with the corresponding cell values in the LiDAR-derived DTM. Statistical measures are calculated to assess the DTM's vertical accuracy, as shown in Table 3.3 and in Figure 3.7.

The analysis shows a negative bias of -0.047 m, indicating a very small underestimation of ground elevation on average. The RMSE is 0.215 m, with a median absolute residual of 0.074 m, suggesting overall good accuracy. These results confirm the DTM's reliability for further analysis.

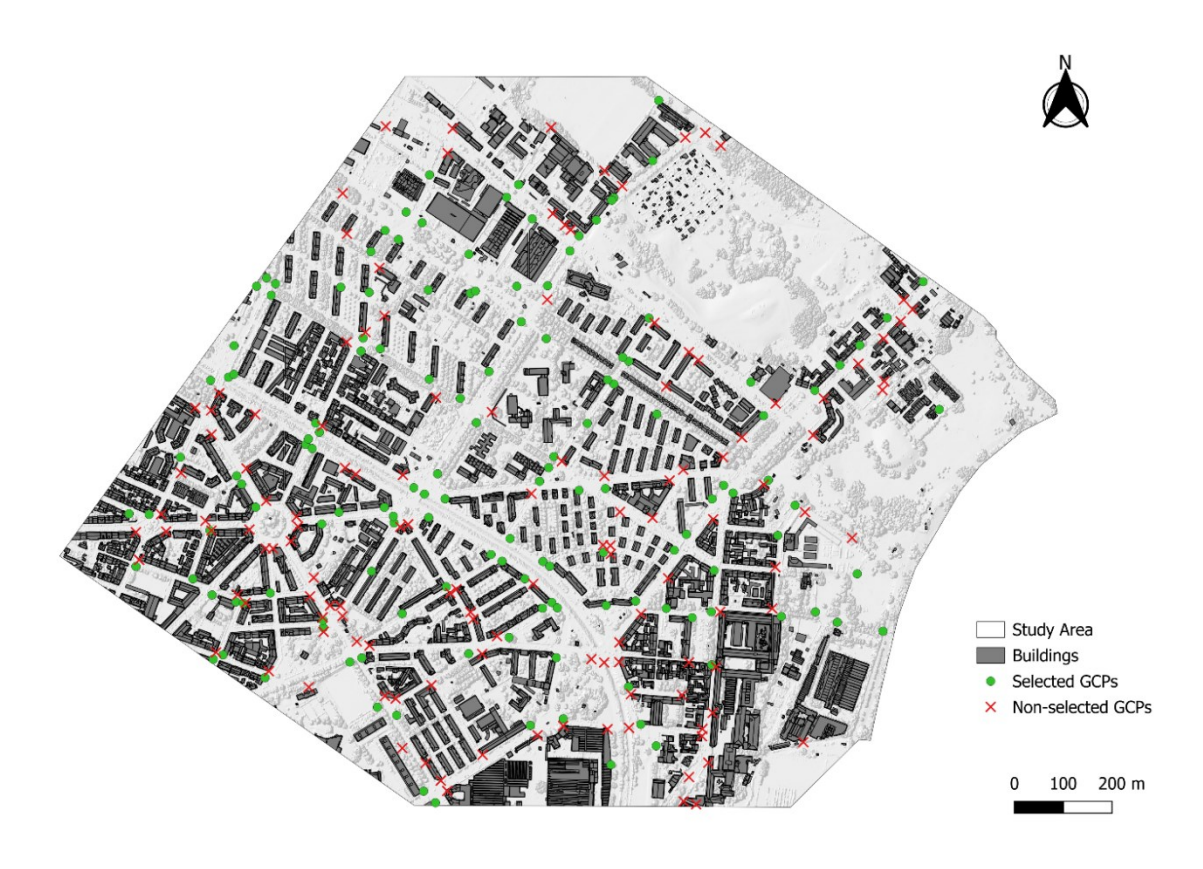


Figure 3.6 - Ground Control Points (GCPs)

Table 3.3 - DTM vertical accuracy,

Metric	Value
Total points	233
Excluded points	91
Valid points	142
Min residual (m)	-1.031
Max residual (m)	1.656
Bias (mean error) (m)	-0.047
RMSE (m)	0.215
MAE (m)	0.119
Std dev $\sigma$ (m)	0.21
5th percentile  resid  (m)	0.013
Median  resid  (m)	0.074
95th percentile  resid  (m)	0.286

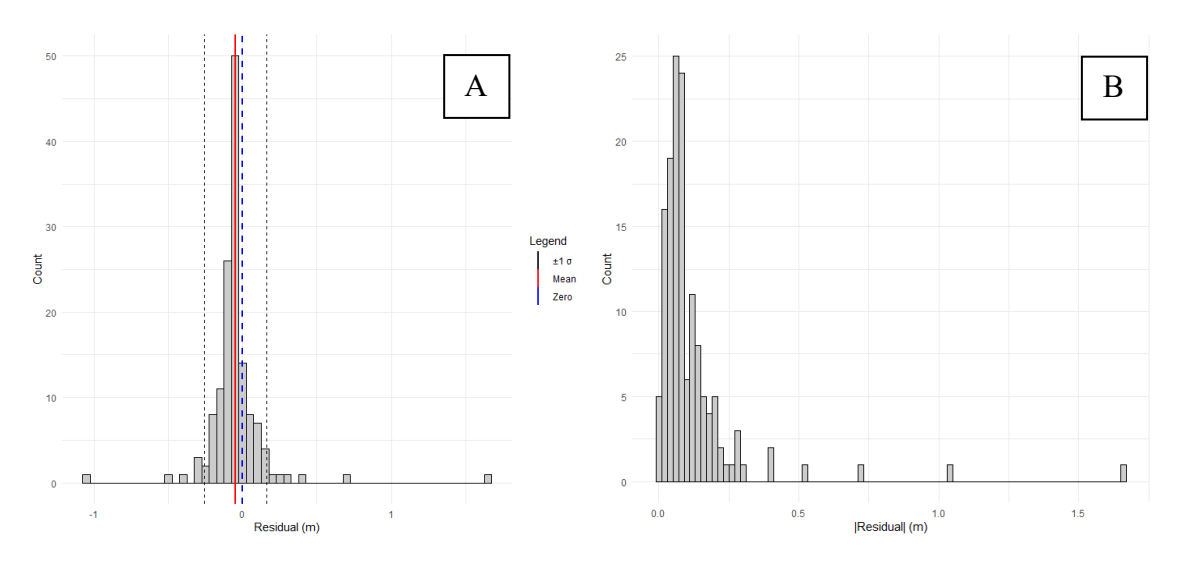


Figure 3.7 - (A) Residuals distribution; (B) Absolute error distribution

### 3.3 Feature Extraction from LiDAR Data

A fundamental step in determining the actual surface area covered by tree vegetation within the study area is the calculation of the Canopy Height Model (CHM). This model provides information on the extent of vegetation, which is essential for a more detailed analysis of how green areas influence temperature. Initially, the normalised Digital Surface Model (nDSM) is derived by subtracting the DTM from the DSM using the raster calculator in QGIS. This model includes elements such as trees, but also buildings, vehicles, and low vegetation, while assigning a value of 0 to all pixels corresponding to ground level. To ensure that only features capable of producing significant shading are considered, a filtering process is applied with a threshold of 3 meters. Elements below 3 m in height are set to 0. Moreover, to isolate vegetation exclusively, a mask is applied to exclude buildings and other volumetric structures, based on data provided by the Piedmont Region Geoportal. Finally, the data are vectorised to obtain a vector format representation of tree-covered green areas, which will be used for subsequent spatial analyses.

The same nDSM was used to derive models characterising only the buildings. In this case, vegetated areas were excluded, allowing for the extraction of the relative height of each building. The resulting raster contains only built structures and allows visualisation of building heights. A combined visualisation of canopy and building heights is presented in Figure 3.8.

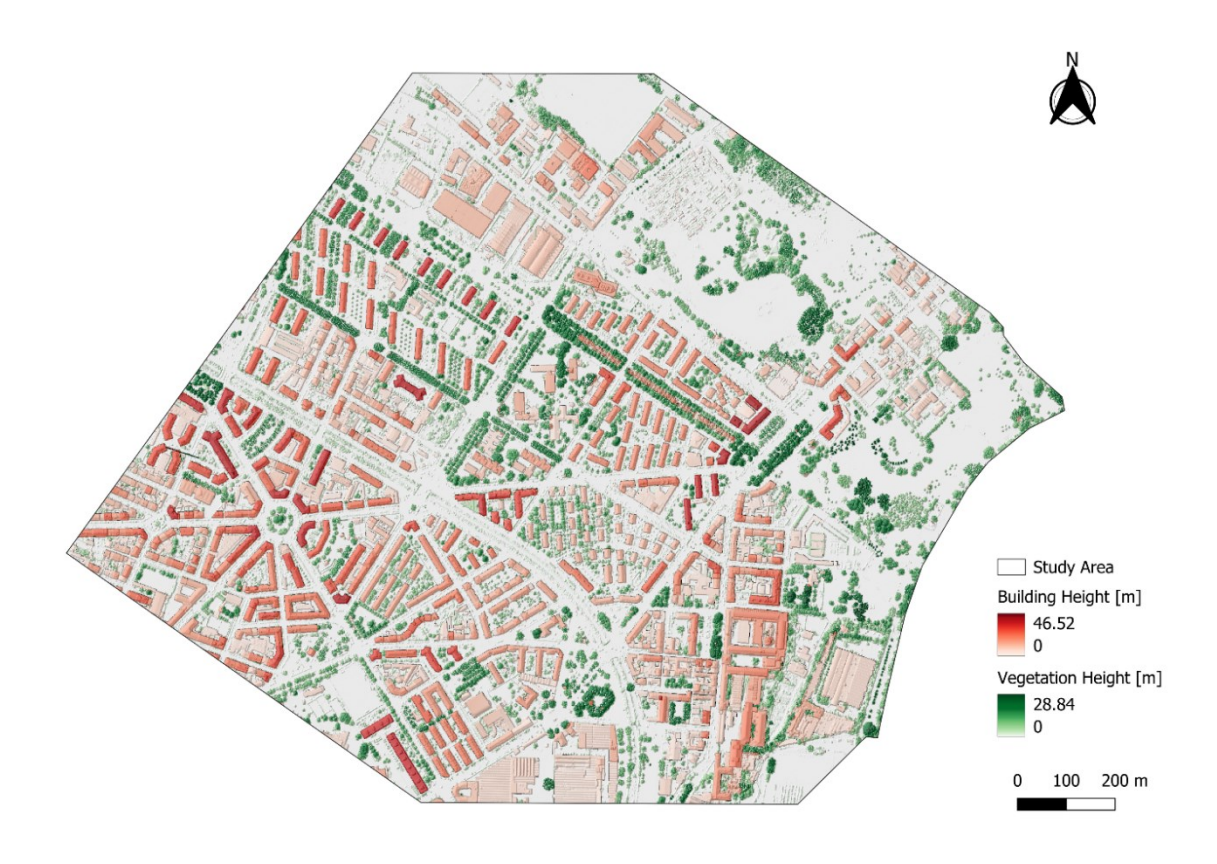


Figure 3.8 - Combined visualisation of building (red) and vegetation canopy (green) heights in the study area

### 3.3.1 Land-Use and Land-Cover Classification

The analysis to determine the main soil categories within the area of interest is performed using various input data from the Piedmont Region Geoportal and the LiDAR-derived tree cover. Specifically, the files are pre-processed in an initial phase of cleaning and correcting the geometry. During this process, care is taken to avoid data redundancy, ensuring that each part of the study area is assigned to a single thematic class and that multiple classes do not describe the same area. After these corrections, each input data is mapped to a final thematic class, as shown in Figure 3.9. Buildings and volumetric units are classified as Built-up, vehicular circulation areas as Roads, green spaces and agricultural land as Green areas, trees as Trees, water bodies as Water bodies, and all remaining classes are grouped under Other. Finally, the area of each individual class is calculated and compared with the entire study area as a percentage to determine its share of the study. The final distribution of classes is summarised in Table 3.4.

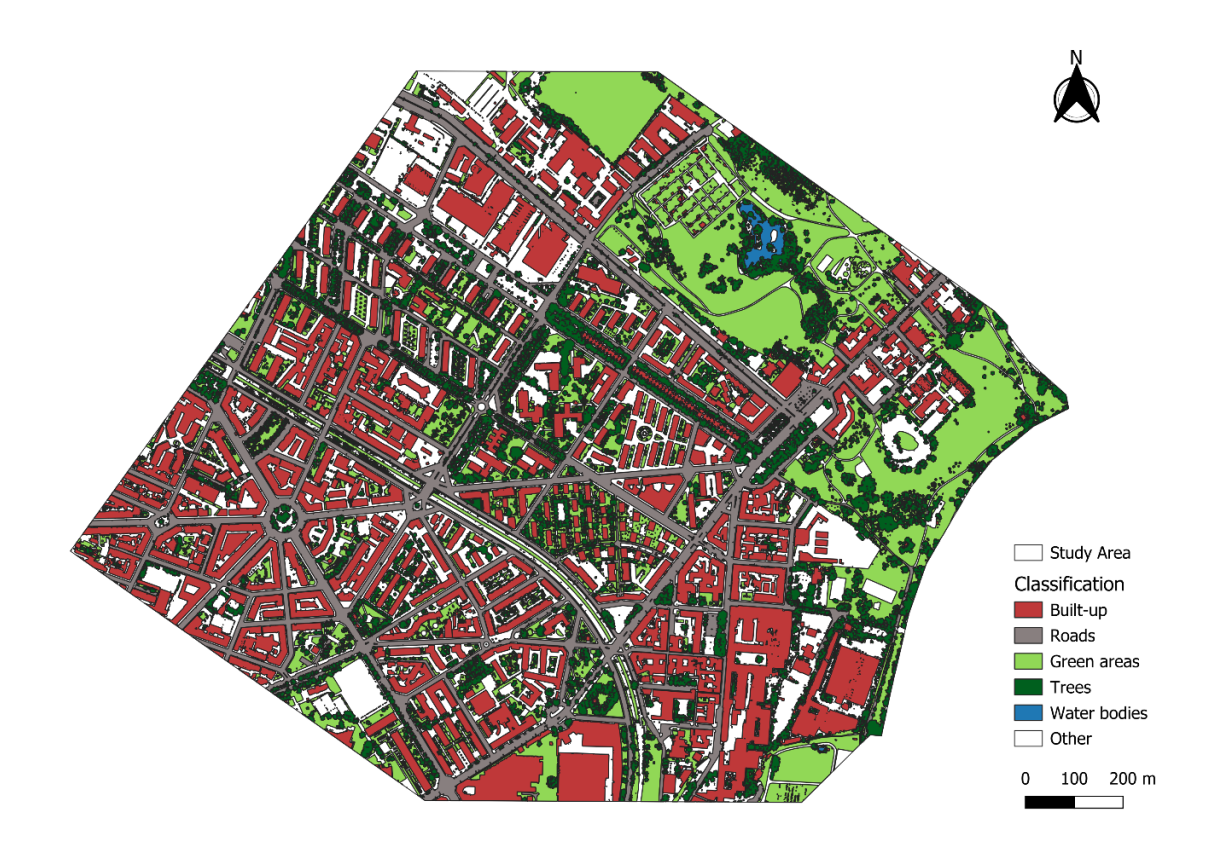


Figure 3.9 - Classification of land-use and land-cover

The results of the analysis of the main components of land cover and use in the area show that the most prevalent component is buildings, which account for 24.57%. These values are typical of urbanised areas. It is important to note that this category includes the roof surfaces of residential and commercial buildings as well as those of industrial areas. The materials used for these roofs can significantly vary (tiles, concrete, metal, plastic roofing, etc.) so their thermal behaviour and response to solar exposure could also differ. Green areas, including green spaces, urban parks, and agricultural land, also represent a high percentage, corresponding to 21.93%. In particular, the largest green areas are located in Parco dell'Arrivore and Parco della Confluenza di Piazza Sofia. Considering tree-covered areas, which account for 13.71% of the total, the combination of these two classes, both mostly permeable and subject to evapotranspiration, brings the overall percentage to 35.64%. These areas are the most important for UHI mitigation strategies, as their increased presence leads to reduce surface temperatures. Vehicular circulation areas represent a relatively high percentage at 13.71%. These surfaces, made of impermeable materials with low albedo values such as concrete and asphalt, heat up rapidly on the hottest days, exacerbating the UHI phenomenon. Water bodies are very limited, since the boundaries of the study area stop at the

banks of the Po River and do not include the river itself, and correspond only to the pond in Parco dell'Arrivore. Finally, the "Other" category corresponds to various classes which are not sufficiently specific and fall within areas with different material types and permeability values. To avoid potential classification errors, these were grouped into a single category and excluded from subsequent analyses.

Table 3.4 - Summary of land-use and land-cover classes

Input	Description	Output	Percentage
Circ_6_020102_EDIFICIO  Circ_6_020101_UNITA_VOLUMETRICA	Buildings (main structures) Volumetric	Built- up	24.57%
	units		
Circ_6_010101_AREA_DI_CIRCOLAZIONE_ VEICOLARE	Vehicular circulation areas	Roads	13.95%
Circ_6_060401_AREA VERDE  Circ_6_060106_COLTURA_AGRICOLA	Green spaces, urban parks Agricultural land	Green areas	21.93%
	land		
Trees	Tree canopy from LiDAR extraction	Trees	13.71%
Circ_6_040102_SPECCHIO_D'ACQUA	Natural or artificial water bodies	Water bodies	0.25%
(all other classes)	All remaining land-use/land-cover classes	Other	25.59%

# 4. Shadow Analysis

Shadows occur when objects totally or partially occlude direct light from a source of illumination. When considering the shadow cast by a typical high-rise building, there are two shadows present: the cast shadow and the self-shadow. A cast shadow is projected by the object in the direction of the light source (the one cast on the ground) and the self-shadow is the part of the object which is not illuminated by direct light (i.e., the facade of the building). The part of a cast shadow where direct light is completely blocked by an object is called the umbra, while the part where direct light is partially blocked is called the penumbra (Arévalo et al., 2008; Dare, 2005). In nadiral remote sensing, almost all shadows are cast shadows because the sensor looks straight down.

Shadow analysis examines how buildings, trees, and other structures influence the amount of sunlight reaching different areas throughout the day, as they can reduce local temperatures by limiting direct solar exposure (Huang & Wang, 2019). A study by Martinelli et al. (2015) revealed that shaded areas provide improved thermal conditions and greater outdoor comfort. In fact, temperatures in shaded areas are cooler than in unshaded areas.

Shadow analysis often relies on urban models derived from LiDAR data, which provide detailed DSMs. Researchers often use these models to assess how buildings influence shading in public areas, making them essential in urban planning decisions that focus on thermal comfort (Konarska et al., 2014; Zwoliński & Jarzemski, 2015).

Simulation software such as UMEP-SOLWEIG (Lindberg et al., 2018) allow shadow studies. In particular, this model simulates shadows using the "shadow volume" approach described by Ratti & Richens (1999). In this method, the raster DSM is shifted according to the Sun's azimuth angle and lowered at each iteration based on the Sun's elevation angle to calculate shadow volumes. A portion of the shadow volume is determined at each iteration, and the entire shadow volume is generated by taking the maximum value for each iteration. This is stored in a new DSM. The shadow volume image is then subtracted from the original DSM to generate the map of shadows. The result is a Boolean image, in which pixels with values lower than zero are in sunshine (assigned value = 1) and those with values greater than zero are in shade (assigned value = 0). The final output visualises shadow distribution at specific times or over extended periods, and the dynamics of shadows depend on factors such as urban geometry and orientation, greenery, time and location.

Using the same software in QGIS, it is possible to analyse the daily shading pattern for a specific date. For this study, the date considered is August 15th, corresponding to the acquisition of remotely sensed aerial thermal data over Turin. The shading distribution within the study area, simulated from sunrise to sunset with hourly variability, is shown in Figure 4.2. Furthermore, Figure 4.1 shows the complete daily shading pattern, providing an overview of areas that are most shaded or exposed to sunlight throughout the specific day. Specifically, observing the trend percentage of solar radiation exposed and the shaded area throughout the day (Figure 4.3), shaded areas are abundant in the morning, reaching about 90% at 7:00, and then declining to a minimum of about 19% around 13:30 (solar noon at 13:34) when sunlight exposure is highest, before rising again in the evening. It is important to note that this pattern is derived from a nadir-based DSM, which does not capture the threedimensional structure of tree canopies. Consequently, the shade under trees when the sun is high is not represented, so the percentage of ground shading is slightly underestimated during these periods. Finally, for the purposes of this study, the shaded and unshaded areas at solar noon are vectorised in order to be used as the basis for subsequent statistical analyses, which will be discussed in Section 8. These areas are shown in Figure 4.4.

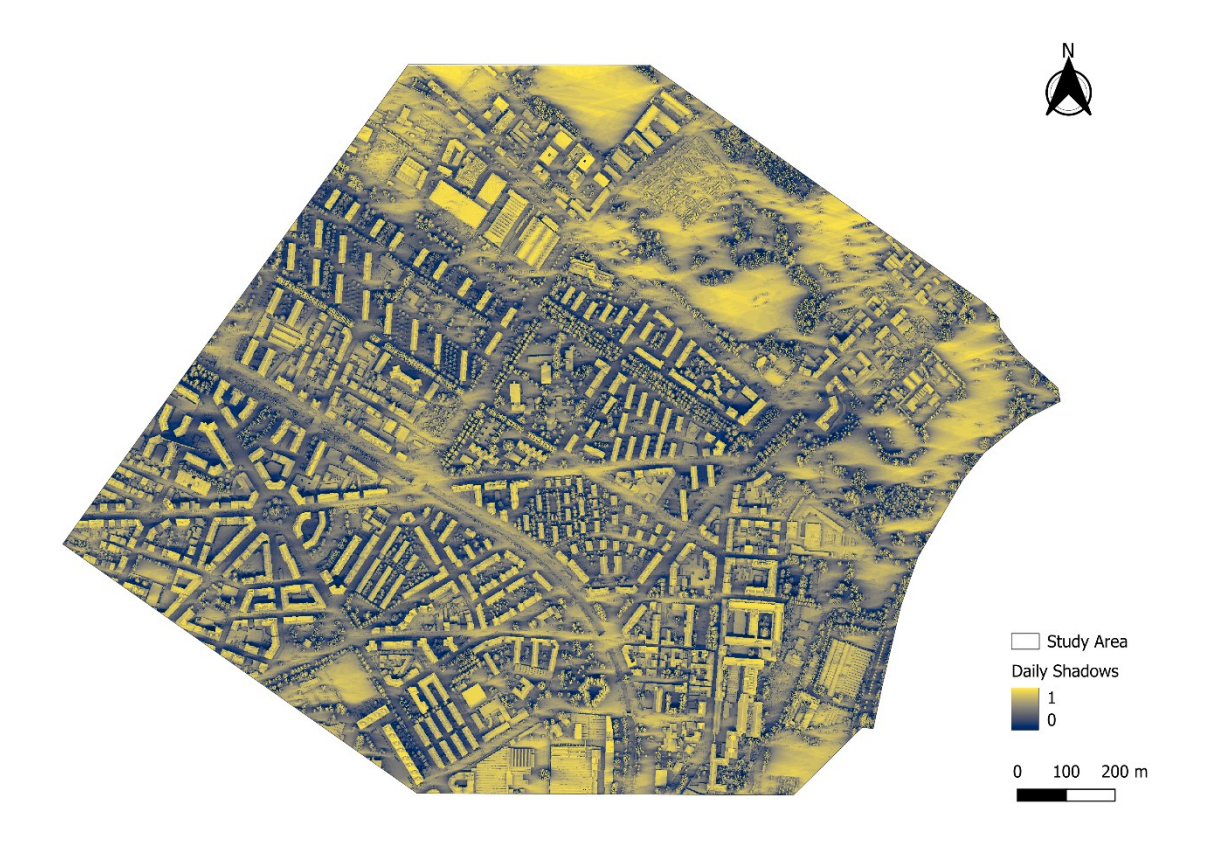


Figure 4.1 - Cumulative daily shading map

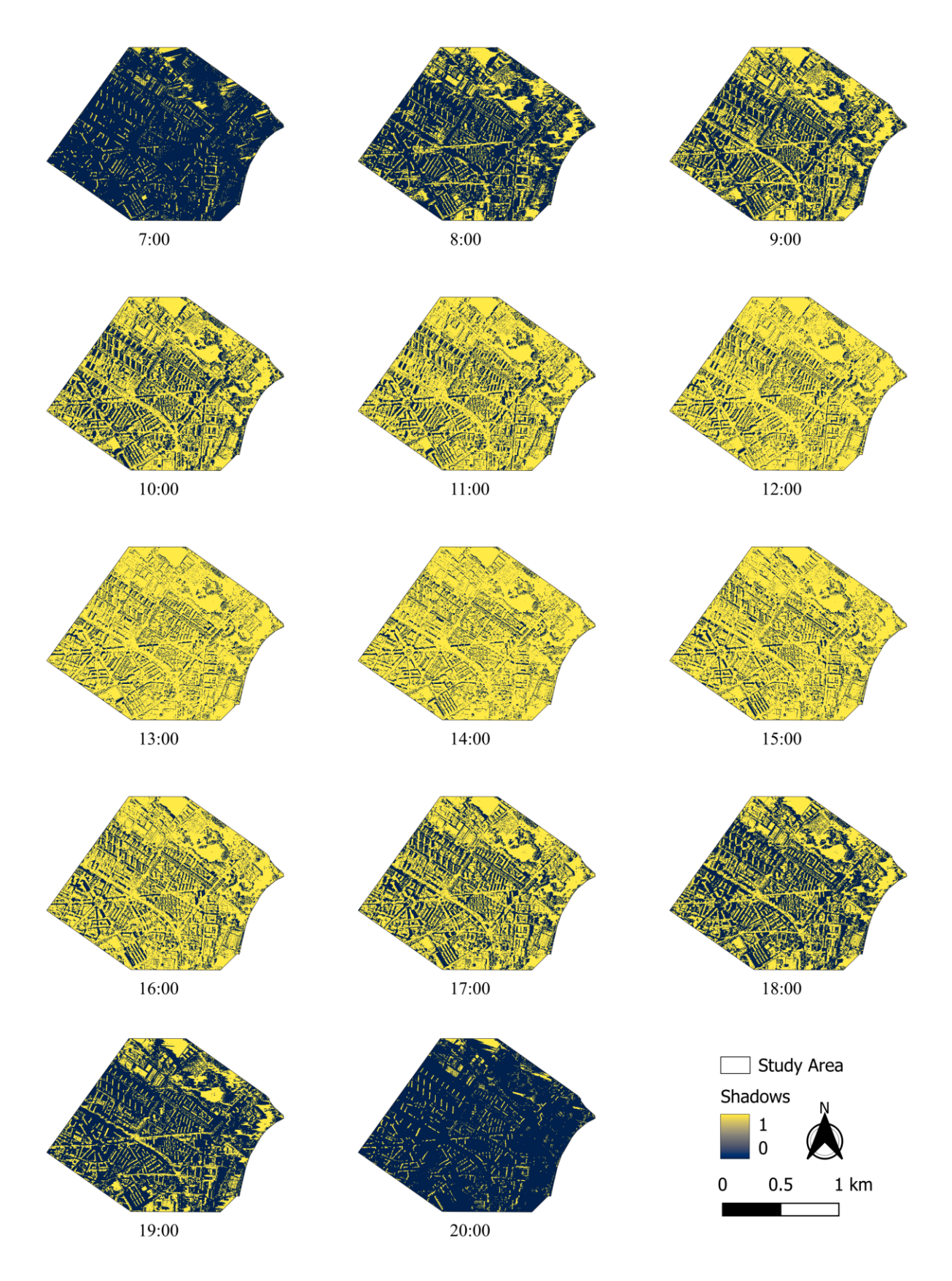


Figure 4.2 - Shading simulation

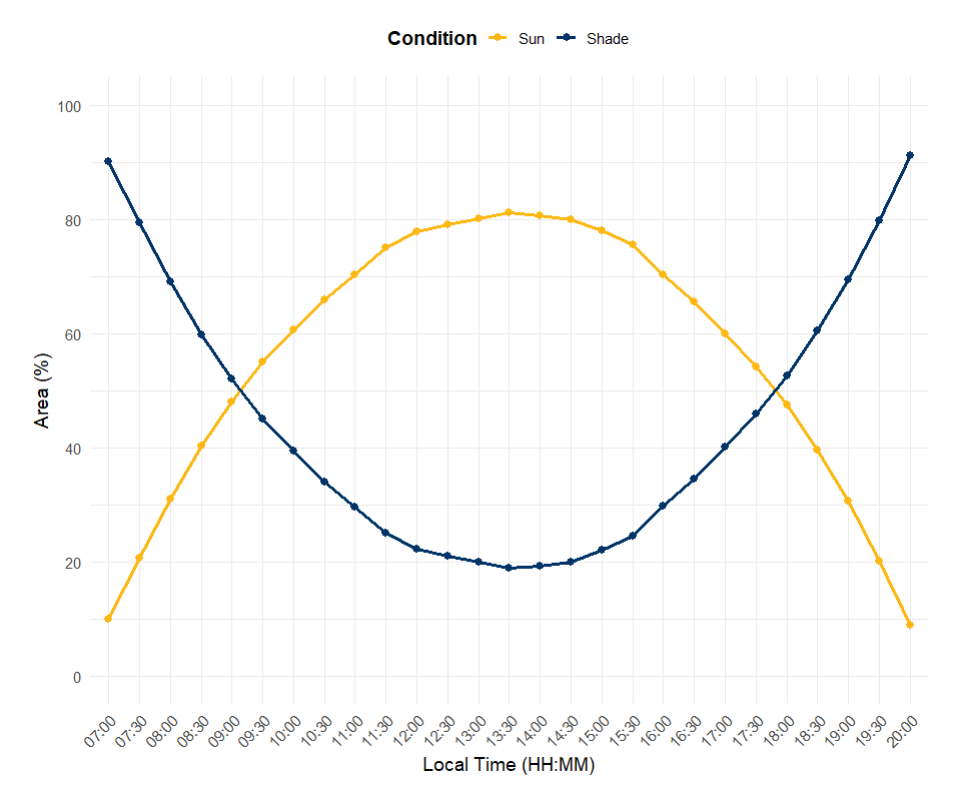
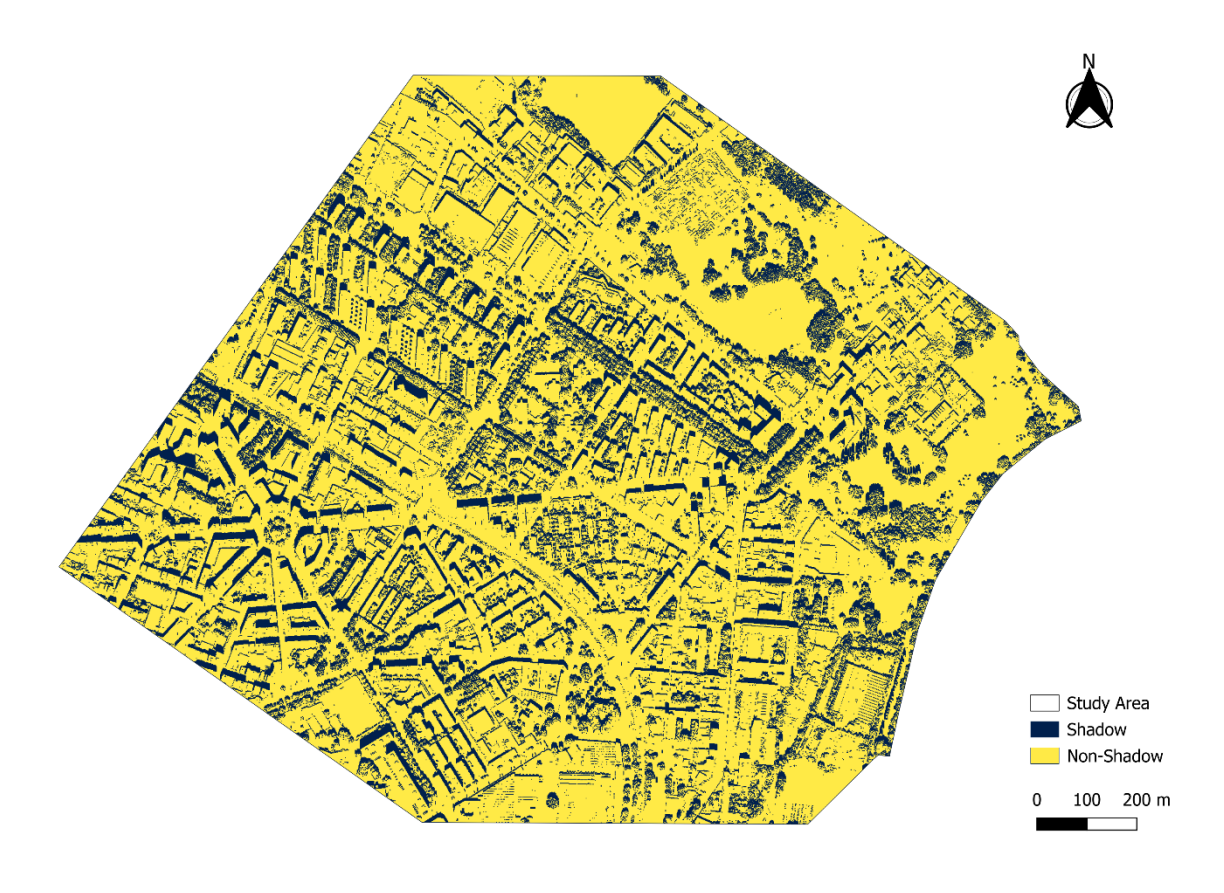


Figure 4.3 - Percentage of solar radiation exposure and shaded area



Figure~4.4 - Solar~noon~shading~simulation

## 5. Urban Canyons and Sky View Factor

Urban geometry plays a critical role influencing the UHI effect. In particular, the thermal and radiative balance of cities is greatly affected by so-called urban canyons. Oke was the first to create a theory of urban canyons (Nunez & Oke, 1977; Oke, 1976). According to this theory, an urban canyon is a three-dimensional space between buildings which has a bottom (the road) and two boards (building walls). A key parameter that governs the radiative exchanges in these areas is the Sky View Factor (SVF), which quantifies how open or enclosed a location is relative to surrounding urban features through a dimensionless measure between zero and one, representing totally obstructed and free spaces, respectively (Oke, 1981). Mathematically, the SVF at a given point is defined as the ratio of the radiation received (or emitted) by a planar surface to the radiation emitted (or received) by the entire hemispheric environment (Watson & Johnson, 1987). When obstructions such as buildings or vegetation are present, the visible sky is reduced, lowering the SVF (Figure 5.1).

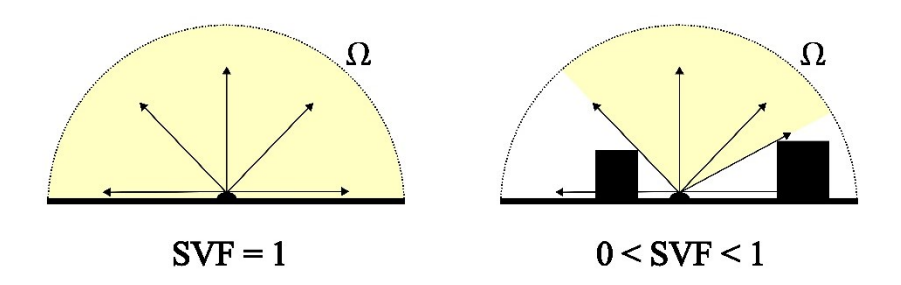


Figure 5.1 - Concept of Sky View Factor (SVF): open sky (SVF = 1) vs obstructed locations (0 < SVF < 1)

Usually SVF are calculated by image-based and computational methods. A typical example of this method is a fisheye photograph (Figure 5.2) combined with image processing techniques which help to distinguish sky from obstacles (Honjo et al., 2019). When photographic data is unavailable, the assessment of the SVF may be carried out using GIS-based methods. Moreover, as indicated by Hämmerle et al. (2011), the use of advanced 3D-modeling techniques could also be considered.



Figure 5.2 - Illustration of SVF derivation: Google Street View fisheye images (top), horizon detection (bottom), and resulting SVF (bold) for four worldwide locations (Middel et al., 2018)

In this study, the UMEP (Urban Multi-scale Environmental Predictor) plug-in on QGIS is used to calculate the SVF. The output is a continuous raster with values between 0 and 1 (Figure 5.3), which is then classified into five categories to simplify spatial analysis and visualisation (Figure 5.4). In the SVF analysis, both buildings and vegetation are assumed to affect sky visibility. The High class covers 29.7% of the area, the Moderate class 24.1%, and the Very High class 20.3%. This indicates that the area is characterised by a strong presence of open spaces that are directly exposed to solar radiation, and potentially most at risk during the daytime of the hottest sunny days. The areas with Very Low SVF values constitute the 7.9% of the area.

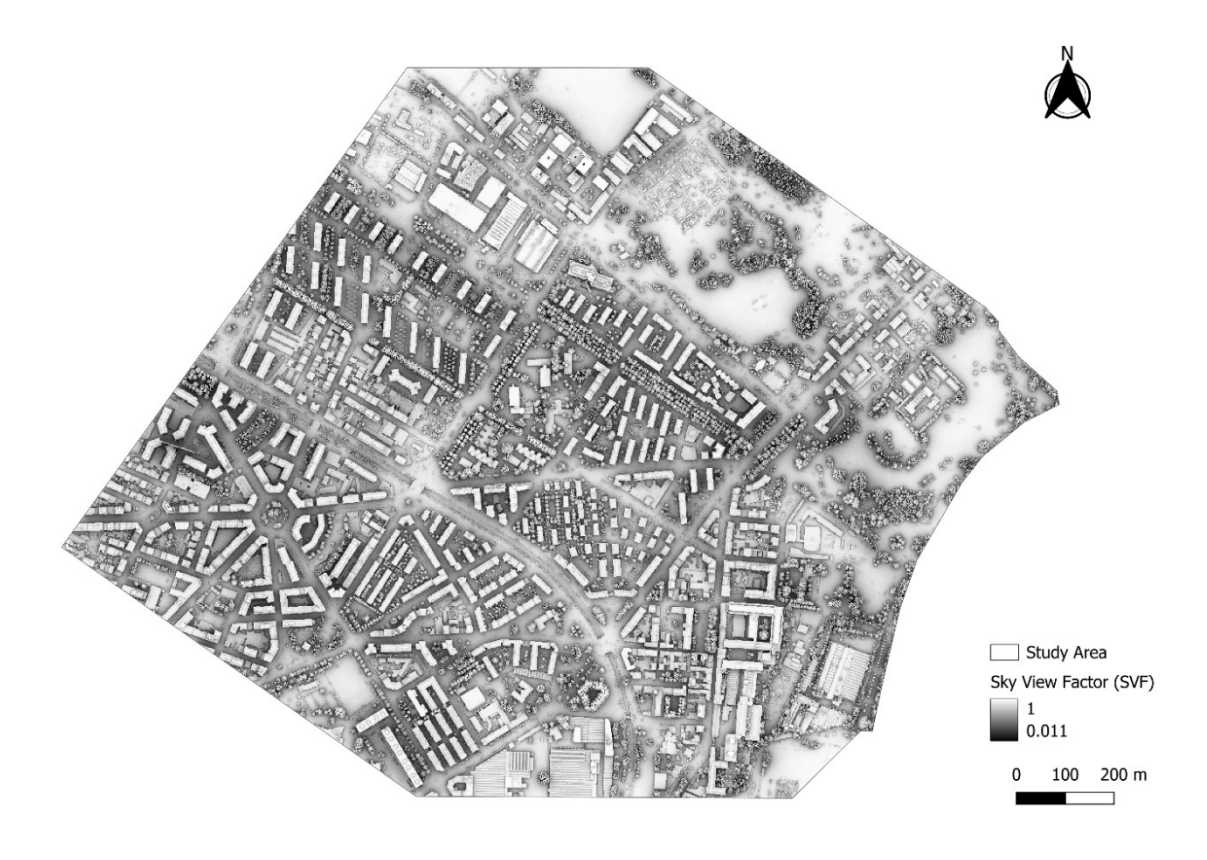


Figure 5.3 - Sky View Factor (SVF)

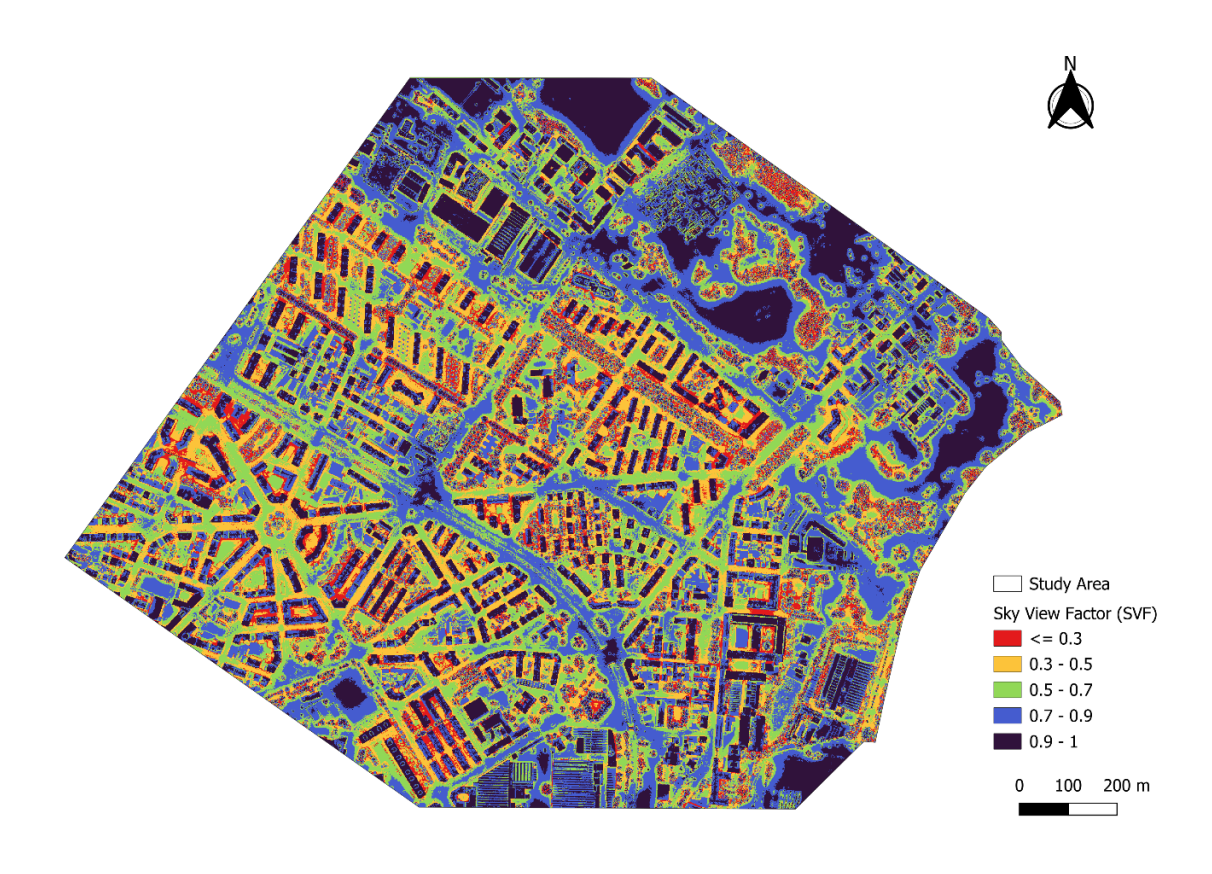


Figure 5.4 - Classified SVF

SVF plays a double role in regulating the temperature of a city. In the daylight, high SVF values result in direct solar irradiance on the exposed surfaces. These surfaces have a higher heat yield (Jiao et al., 2019). In contrast, at night, high SVF values help in the release of longwave radiation from urban canyons to the surrounding environment, leading to cooling. If an urban area has low SVF, the night heat release is limited. Consequently, these surfaces exhibit higher minimum temperatures and are also subjected to longer periods of heat stress, especially during HWs (Palusci & Cecere, 2022; Syrios & Hunt, 2007).

Another factor influenced by urban morphology is airflow. The low SVF value areas are usually less ventilated due to the physical obstacles present. This results in a situation of a stagnant microclimate which aggravates the UHI because of limited heat dispersion (Nunez & Oke, 1977).

Open urban spaces such as squares, very wide streets, and parking areas are quite different because even though they have high SVF, they mostly lack vegetation and shading. These spaces get direct solar radiation for the entire day, and if these areas are not well covered by trees or other shields, they are very likely to become hot and increase health risks during HWs. As a result, both narrow streets with low SVF and open spaces with high SVF can create thermally stressful conditions.

# 6. Solar Irradiance and Radiative Exchange in Urban Area

### 6.1 Fundamentals of Solar Irradiance

A key factor contributing to the UHI effect is solar irradiance. The Earth's climate and energy systems are powered by the Sun (IPCC, 2013; Lindsey, 2009). Radiation heat transfer is the process by which energy is exchanged between bodies in the form of electromagnetic waves. This is the only form of energy transfer that can take place in a vacuum such as the region between the Sun and the Earth. The energy flux due to radiation on a surface, referred to as irradiance E, is measured in watts per square meter (W/m²) in the SI system and is defined as the radiant flux received by a surface per unit area. It is related to the incident radiant flux  $\Phi$  by:

$$E = \frac{d\Phi}{dA}$$
 (Eq. 6.1)

Irradiance varies with factors such as time of day, latitude, season, atmospheric conditions, and the Earth's orbit. As shown in Figure 6.1, the total irradiance *E* incident on a surface can be expressed as the sum of three distinct components (Matius et al., 2021):

$$E = E_{direct} + E_{diffuse} + E_{reflected}$$
 (Eq. 6.2)

Where:

Direct irradiance ( $E_{direct}$ ) is the part of the solar irradiance that directly reaches a surface without being scattered or reflected by the atmosphere. It is a function of the solar incidence angle  $\theta$  and the direct normal irradiance  $E_{DN}$  (the solar radiation received on a surface perpendicular to the Sun's rays):

$$E_{direct} = E_{DN} \cos \theta \tag{Eq. 6.3}$$

- $E_{DN}$  depends on factors such as the day of the year, atmospheric conditions, and solar altitude;
- Diffuse irradiance ( $E_{diffuse}$ ) is the part of the solar irradiance that is scattered by molecules and particles in the atmosphere and arrives at the surface from all directions. It depends on atmospheric conditions and the tilt angle of the surface;

- Reflected irradiance ( $E_{reflected}$ ) represents the part of the solar irradiance that has bounced off surrounding surfaces, such as the ground or nearby buildings, and subsequently arrives at the point of interest. The amount depends on the reflectance (albedo) of the surrounding surfaces, as well as surface geometry.

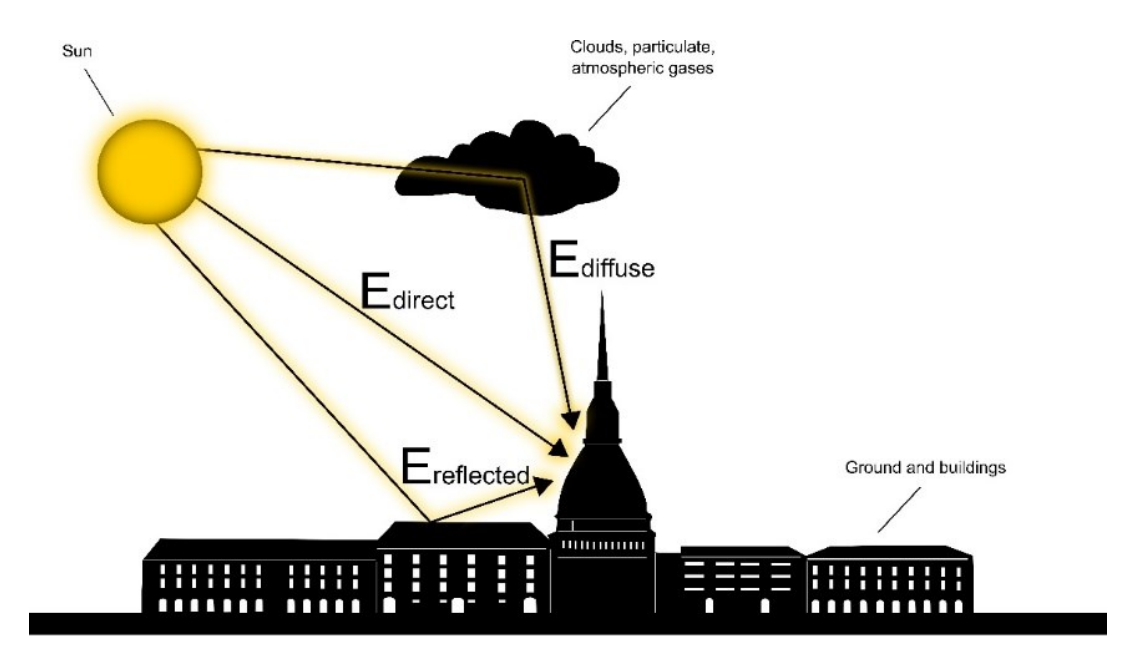


Figure 6.1 - Direct, diffuse, and reflected irradiance

# 6.2 Radiative Properties and Energy Balance in Urban Environments

Urban surfaces interact with solar irradiance according to fundamental optical properties that satisfy the conservation relation:

$$\alpha + \tau + \rho = 1 \tag{Eq. 6.4}$$

#### Where:

- $\alpha$  is the fraction of incident solar irradiance absorbed by the material (absorptivity);
- $\tau$  is the fraction transmitted through the material (transmissivity);
- $\rho$  is the fraction reflected by the material (reflectivity).

For most surfaces characterising urban environments, transmission is negligible ( $\tau = 0$ ), reducing the relation to:

$$\alpha + \rho = 1 \tag{Eq. 6.5}$$

This suggests that the surface absorbs any solar radiation that is not reflected (Kehagia et al., 2019). It is essential to formulate the concept of energy balance in order to more accurately describe energy dynamics in urban areas. The general energy balance equation is derived from the first rule of thermodynamics:

$$Energy gains = Energy losses + Energy storage$$
 (Eq. 6.6)

In an urban system, energy inputs, primarily from solar radiation and anthropogenic heat sources, are distributed through various pathways, including (Lin et al., 2017):

- Convection;
- Evaporation and transpiration;
- Storage in urban materials;
- Horizontal advection.

This can be expressed as:

$$q_r + q_T = q_E + q_L + q_S + q_A$$
 (Eq. 6.7)

Where:

- $q_r$  is the net radiative heat flux;
- $q_T$  is the anthropogenic heat input;
- $q_E$  is the sensible heat flux;
- $q_L$  is the latent heat flux;
- $q_S$  is the heat stored in urban materials;
- $q_A$  is the net horizontal heat advection.

The main component of energy input in urban environments is solar irradiance absorbed by surfaces, which directly influences the energy balance of the system. The way a surface interacts with incoming radiation is governed by its radiative properties, including absorptivity ( $\alpha$ ), reflectivity or albedo ( $\rho$ ) and emissivity ( $\epsilon$ ). Urban materials are commonly characterised by high absorptivity for solar irradiance and low albedo, resulting in a wide fraction of the incoming solar irradiance absorbed by surfaces. This absorbed energy increases the energy of urban surfaces, raising their temperature. Absorbed energy is then conducted deeper, emitted as radiation, or transferred to air near the surface by convection

(Kaloush et al., 2008). The instantaneous absorbed solar irradiance on an urban surface can be expressed as described by Incropera & DeWitt (1996):

$$q_{solar} = \alpha \left( E_{direct} + E_{diffuse} + E_{reflected} \right)$$
 (Eq. 6.8)

The albedo represents the fraction sunlight that is diffusively reflected by a surface, and it can be defined as:

$$\rho = 1 - \alpha \tag{Eq. 6.9}$$

The values of albedo assumed by urban surfaces varies depending on the construction materials used, with values ranging from 0 to 1, corresponding to total absorption or refraction, respectively (Sangiorgio et al., 2020). Some common absorptivity and albedo values for different surfaces are provided in Table 6.1 (Nichols Consulting Engineers, 2012).

Table 6.1 - Representative absorptivity and albedo values for various surfaces

Surface Type	Absorptivity α	Albedo ρ
Fresh Asphalt	0.95	0.05
Fresh Grey Portland Cement	0.65	0.35
Black Soil	0.87	0.13
Desert Sand	0.60	0.40
Bare Soil (land)	0.83	0.17
Cool Pavement Coatings	0.50	0.50
Aged Asphalt	0.80	0.20
Arctic Region	0.23	0.77
Green Grass	0.75	0.25
White Portland Cement	0.20	0.80
Aged Portland Cement	0.71	0.29
White Roof Coatings	0.12	0.88

From a climate perspective, albedo acts as a defence against solar heating, and it is considered one of the most efficient factors in mitigating the UHI effect (Hayes et al., 2022; Morini et al., 2016; Sangiorgio et al., 2020). For example, in the case of Salento's white cities, the high albedo of limestone surfaces contributed to a rare reverse UHI effect during HWs (De Razza et al., 2024). Moreover, materials and surfaces characterised by a combination of low albedo and emissivity values tend to absorb and retain heat during the day and release it very slowly at night, intensifying the UHI effect.

Emissivity values are essential for understanding how closely a surface behaves to an ideal black body, and are dependent on the type of material and the surface texture, as shown in the following table (Table 6.2):

Table 6.2 - Representative emissivity values for various surface materials

Material	Emissivity ε
Asphalt	0.88
Brick	0.90
Concrete, rough	0.91
Glass, smooth (uncoated)	0.95
Limestone	0.92
Marble (polished)	0.89 to 0.92
Paint (including white)	0.90
Paper, roofing or white	0.86 to 0.88
Plaster, rough	0.89

The emitted long-wave thermal radiation from these surfaces follows the Stefan-Boltzmann law:

$$q_{emit} = \varepsilon \sigma T^4$$
 (Eq. 14)

Where:

-  $\varepsilon$  is the surface emissivity;

- $\sigma = 5.67 \times 10^{-8} \,\mathrm{W \cdot m^{-2} \cdot K^{-4}}$  is the Stefan-Boltzmann constant;
- T is the surface temperature in K.

However, surfaces also receive longwave radiation from the atmosphere and surrounding objects. The net longwave radiative flux is given by:

$$q_{r,longwave} = \varepsilon (R_{L\downarrow} - \sigma T^4)$$
 (Eq. 6.10)

Where  $R_{L\downarrow}$  is the incoming longwave radiation. The net radiative heat flux  $(q_r)$  exchanged between an urban surface and the environment can be obtained from the balance of incoming and outgoing shortwave and longwave radiation. Mathematically, it can be expressed as described by Bretheron (2023):

$$q_r = \alpha E + \varepsilon (R_{L\downarrow} - \sigma T^4)$$
 (Eq. 6.11)

This net radiative balance determines how much energy is retained or released by the surface.

### 6.3 Solar Radiation Models

Solar radiation models are useful for estimating quantities such as solar irradiance in areas where measurement stations are unavailable or limited. Numerous models developed in a GIS environment have been proposed in the literature. Among them, one of the most used is the r.sun module, described by (Hofierka & Šúri, 2002). The r.sun module is a comprehensive model for estimating solar radiation and is fully integrated into the open-source GRASS GIS environment. Irradiance prediction is implemented through the r.sun.incidout sub-model, which calculates the solar incidence angle and the three components of instantaneous solar irradiance (direct, diffuse, and reflected) (W/m²). The results can be generated either without terrain shadowing (default) or with shadowing effects enabled, under both clear-sky and overcast conditions.

This calculation requires only a few input, such as elevation, slope and aspect which can be derived from LiDAR data, together with the day number and local solar time. Other optional parameters can be adjusted to adapt the simulation to specific conditions. The outputs generated by the r.sun.incidout model are summarised in Table 6.3.

Table 6.3 - Outputs produced by the r.sun.incidout model

 Parameter
 Units

 Solar incidence angle
 Decimal degrees

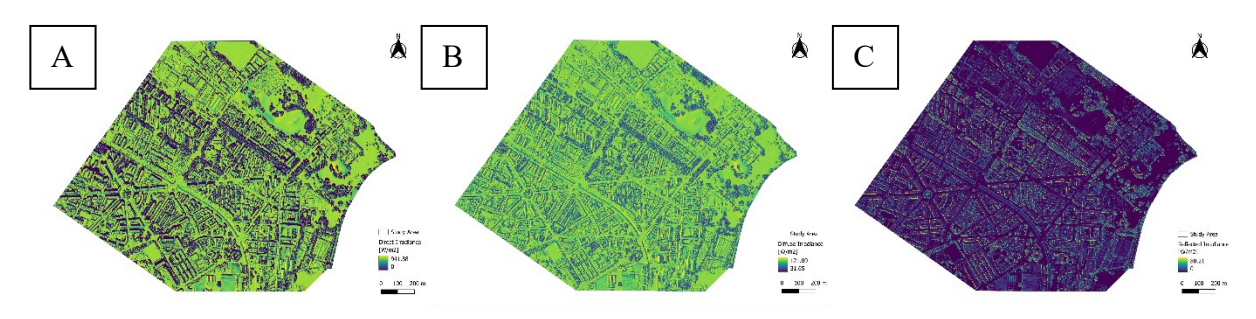
 Direct irradiance
 W/m²

 Diffuse irradiance
 W/m²

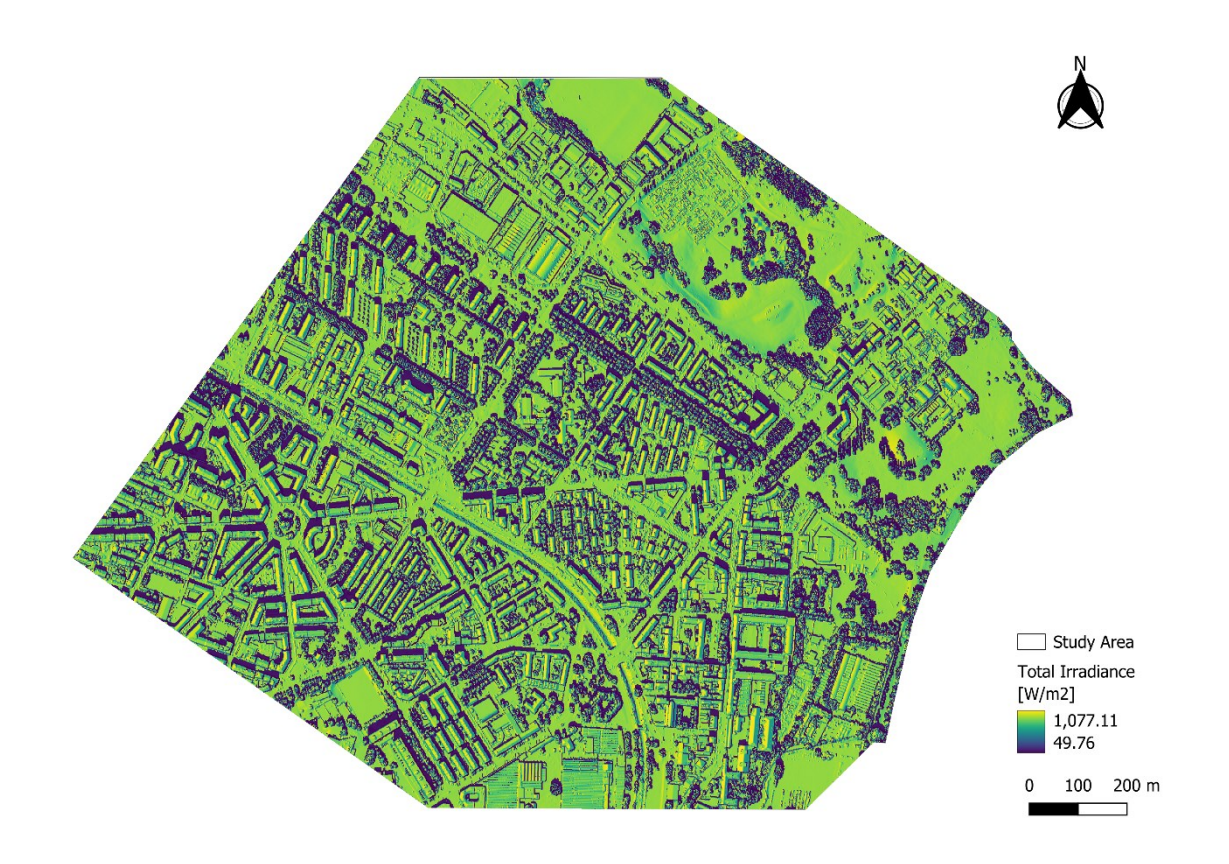
 Reflected irradiance
 W/m²

 Total Irradiance
 W/m²

With this algorithm, using the data of the study area, it is possible to obtain a solar irradiation model characterising the area on 15th August 2025, focusing on the peak solar hour, when the sun is at noon (at 13:34 local time). In Figure 6.2, it is possible to see the three components that determine the irradiance received at ground level. The main component is certainly direct irradiance. The total irradiance is shown in Figure 6.3. Since the model refers to a summer day, calculated at the time of maximum solar elevation and without accounting for atmospheric interference, the resulting irradiance values are very high across most of the study area. For a better understanding of the distribution of solar irradiance over the area, a classification is performed based on the level of total irradiance. Specifically, 5 classes were used ranging from "Very Low" to "Very High". The thresholds are 200, 400, 600, and 800 W/m². The Very High class covers about 52% of the area, while the High (11%), Moderate (5%), and Low (4%) classes together represent about 20%. The Very Low class accounts for 28% of the area. The spatial distribution of these classes can be seen in Figure 6.4



Figure~6.2 - Modelled~solar~irradiance;~(A)~Direct~irradiance;~(B)~Diffuse~irradiance;~(C)~Reflected~irradiance



Figure~6.3 - Total~solar~irradiance

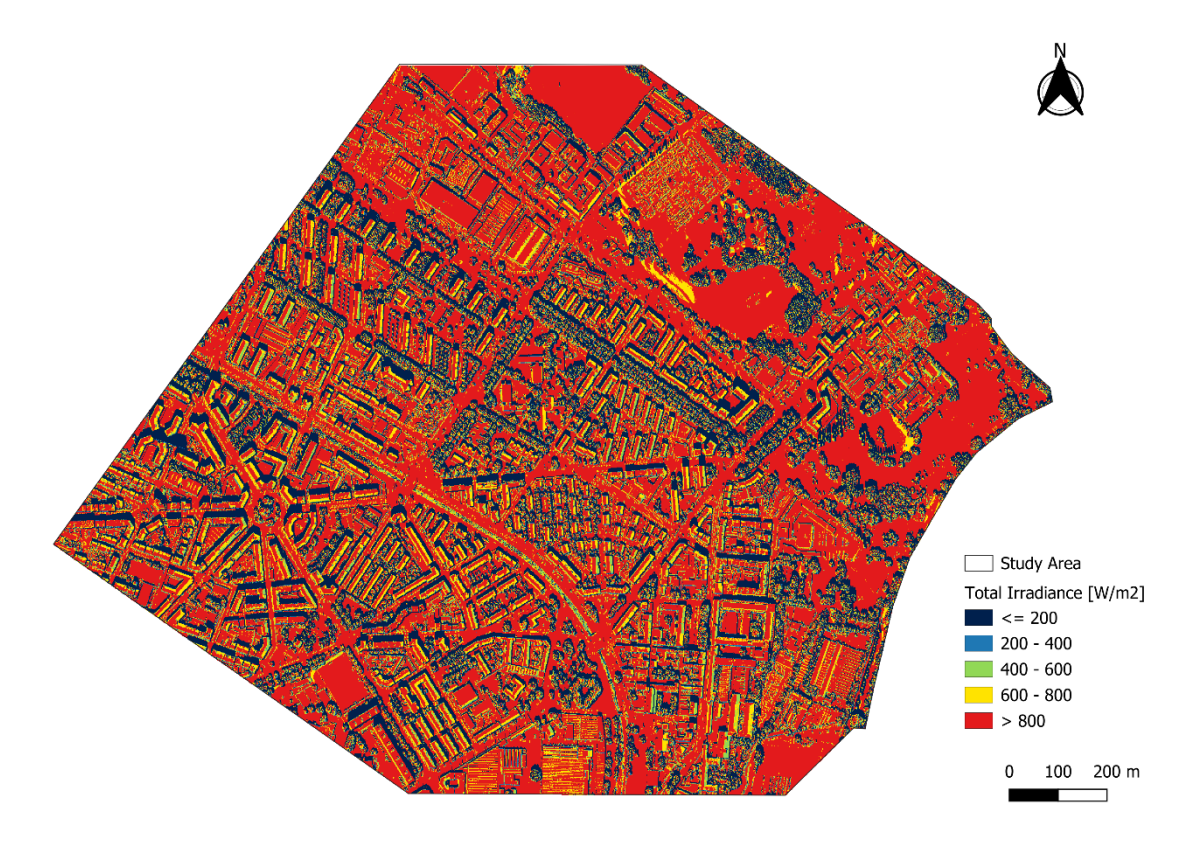


Figure 6.4 - Classified solar irradiance

Additional results from the solar radiation analysis show the duration of solar exposure across the study area. Using the r.sunhours model it can be seen that the most exposed areas are the rooftops of tall buildings and urban parks, which reach peak exposure times of approximately 11 hours of total solar radiation during the day (Figure 6.5). The corresponding total daily radiant exposure (Figure 6.6), instead, ranges from a minimum of approximately 405 Wh/m²·day to a maximum of approximately 7,348 Wh/m²·day, and it is obtained using r.sun.insoltime model.

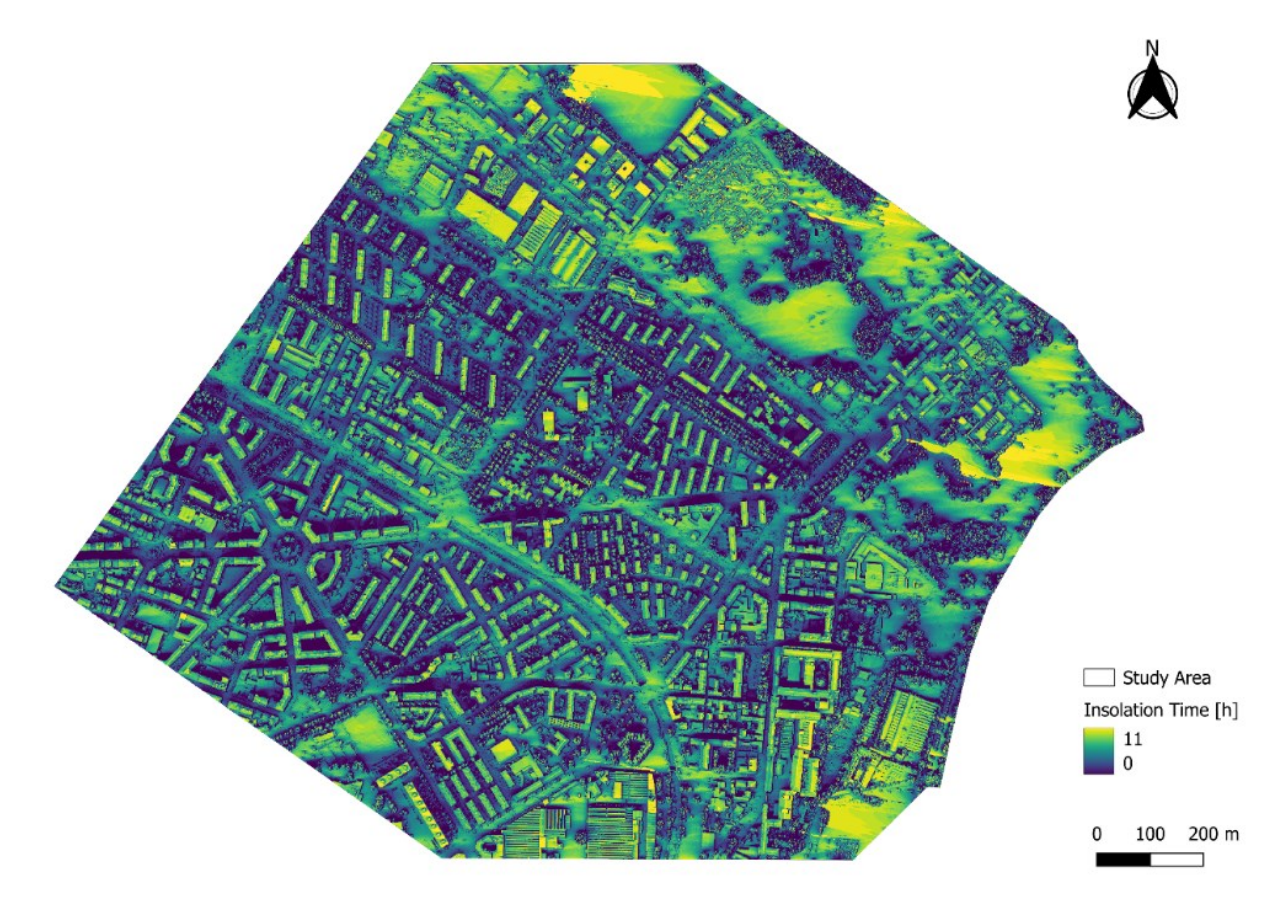


Figure 6.5 - Total insolation time

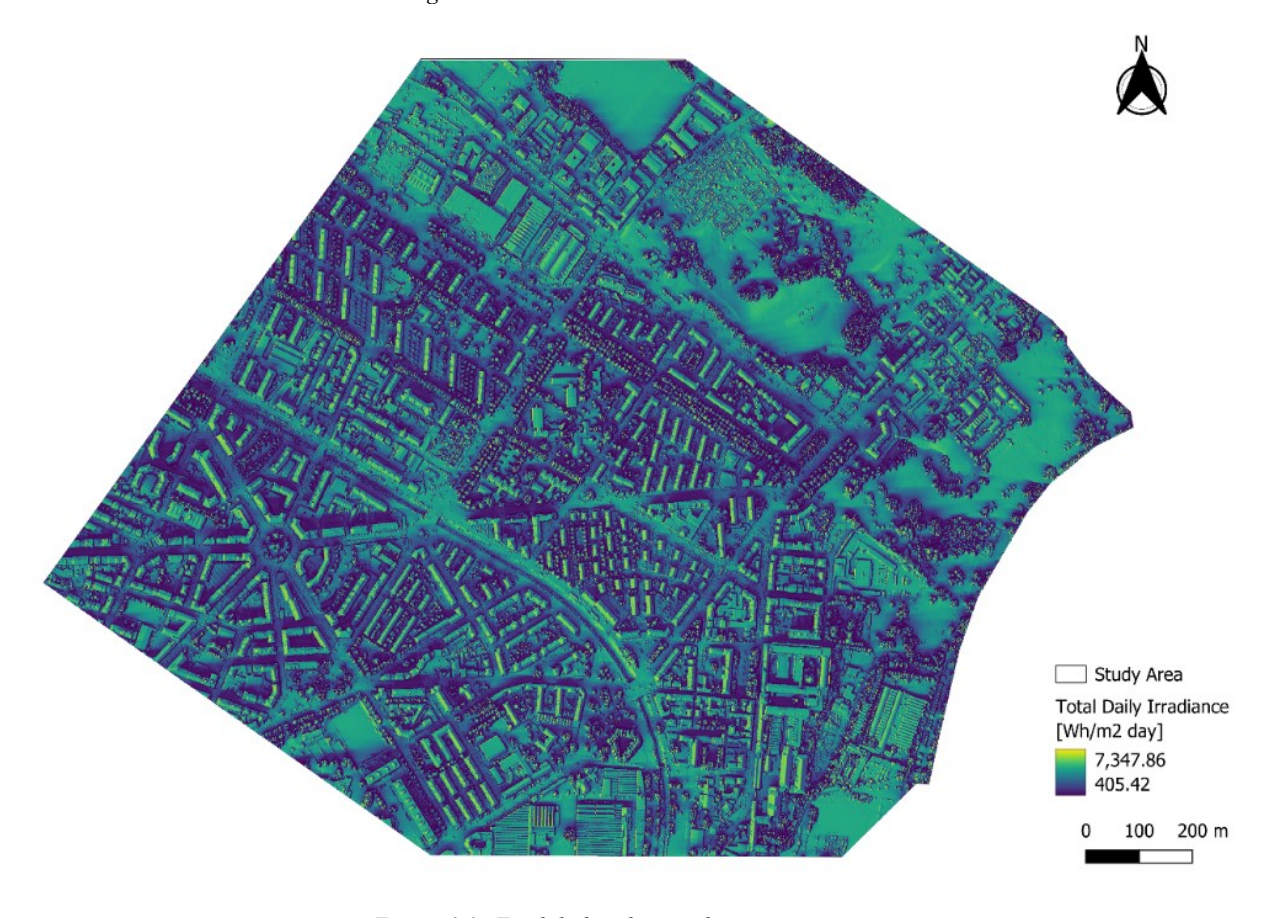


Figure 6.6 - Total daily solar irradiance

# 7. Thermal Remote Sensing

### 7.1 Principles of Thermal Remote Sensing

Thermal remote sensing is a type of passive remote sensing that refers to the measurement of energy emitted by the Earth's surface. This energy does not include the energy reflected by the surface. Thermal remote sensing is based on the infrared (IR) portion of the electromagnetic spectrum, more specifically the longwave infrared region. The IR spectrum is divided into several sub bands based on wavelength and source, specifically whether the radiation is reflected or emitted. The Near-Infrared (NIR) ranges from 0.7 to 1.3 µm, the Short-Wave Infrared (SWIR) from 1.3 to 3 µm, the Mid-Wave Infrared (MIR) from 3 to 5 μm, the Long-Wave or Thermal Infrared (TIR/LWIR) from 8 to 14 μm, and finally the Very Long-Wave Infrared (VLWIR) from 14 to about 1000 μm. Most thermal sensing is performed in the 8-14 µm region because it contains the peak energy emissions of most of the Earth's surface features. Reflected infrared (NIR and SWIR) originates from sunlight bouncing off the Earth's surface, while emitted infrared (MIR, TIR, and VLWIR) comes from the heat of the objects themselves. These characteristics are resumed in Table 7.1. Every object with a temperature above absolute zero (-273.15°C or 0 K) emits energy in the form of electromagnetic radiation (Prakash, 2000). This fundamental principle of physics can be described by Planck's radiation law (Planck, 1914), a mathematical relationship formulated in 1900 by German physicist Max Planck, which quantifies the spectral-energy distribution of radiation emitted by a blackbody according to the formula:

$$E_{\lambda}(\lambda, T) = \frac{2\pi hc^2}{\lambda^5 \left[ \exp\left(\frac{hc}{k_B \lambda T}\right) - 1 \right]}$$
 (Eq. 7.1)

Where:

- $h = 6.626 \times 10^{-34}$  J·s is Planck's constant;
- $c = 2.998 \times 10^8$  m/s is the speed of light;
- $k_B = 1.381 \times 10^{-23}$  J/K is the Boltzmann constant;
- $\lambda$  is the wavelength in  $\mu$ m;
- *T* is the absolute temperature of the object in K.

Most of the radiation released by a black body at temperatures of several hundred degrees Kelvin is infrared. Higher temperatures cause emissions at shorter wavelengths which occur within the visible spectrum (Nguyen et al., 2021).

Table 7.1 - Summary of infrared spectral regions

IR Band	Wavelength Range (µm)	Radiation Type	Source
NIR	0.7 - 1.3	Reflected	Solar
SWIR	1.3 - 3.0	Reflected	Solar
MIR	3.0 - 5.0	Reflected + Emitted	Solar + Thermal
TIR / LWIR	8.0 - 14.0	Emitted	Thermal
VLWIR	14.0 - ~1000	Emitted	Thermal

Thermal remote sensing estimates the object's radiant temperature  $T_R$ , also known as "brightness temperature". Specifically, it is the temperature a black body would need to match the observed radiative intensity of a grey body object.

This temperature is not directly measured by the thermal camera. The acquisition process initially measures the infrared radiation emitted by the object at the surface and converts it into an electrical signal proportional to the intensity of energy received by the sensor. This signal is then processed using algorithms based on the Planck and Stefan-Boltzmann laws to obtain the associated radiant temperature and generate the thermal image. It is important to note that the radiant temperature does not always coincide with the kinetic temperature  $T_K$  of an object. The latter, also known as "true temperature", represents the temperature generated by the vibration of molecules within objects and is measured by thermometers using conventional temperature scales (°F, °C, K). However, the two temperatures are related to each other via emissivity ( $\epsilon$ ) (Sabins & Ellis, 2020), as shown in the following formula:

$$T_R = \sqrt[4]{\varepsilon} \, T_K \tag{Eq. 7.2}$$

This means that the two temperatures coincide only when the investigated object is a blackbody, with an emissivity of 1. In reality, no body behaves perfectly like a blackbody,

and therefore will have emissivity values lower than 1. Therefore, the true temperature of an object will always be higher than its radiant temperature. However, in cases of surfaces with high emissivity and absence of reflections the radiant temperature is a good approximation of the kinetic temperature of the same object, while in many practical applications these temperatures differ, especially when the surface of the investigated object has very low emissivity values and high reflection. In these cases, to obtain a more accurate estimate of the object's true temperature, the measurement should be corrected and compensated using the object's emissivity (Dash et al., 2002).

The two main categories of factors influencing the kinetic temperature are the thermal characteristics of the materials and the heat energy budget. Heat energy budget includes factors such as solar heating, longwave upwelling and downwelling radiations, heat transfer at the earth-atmosphere interface and active thermal sources. A material's thermal conductivity, specific heat, density, heat capacity, thermal diffusivity, and thermal inertia are examples of its thermal properties (Prakash, 2000). In addition to the material of emitting objects, other factors that should be considered include the temperature, humidity, reflective surfaces, wind and convection airflow of the intended operational environments. Cloud, rain and dust are likely to affect thermal cameras as they reduce visibility through scattering caused by particles present in the atmosphere. However, since infrared radiation has a longer wavelength than visible light, it is less attenuated by denser media.

An other important law in remote sensing is Wien's displacement law, published in 1893. It allows calculating, for any temperature  $T_R$ , the wavelength  $\lambda_{max}$  at which the emitted power of a blackbody is maximal (Payra et al., 2023; Wien, 1893). This law is expressed by the following equation:

$$\lambda_{max} = \frac{k}{T_R}$$
 (Eq. 7.3)

Where k is a constant equal to 2898  $\mu$ m·K and  $T_R$  is the radiant temperature expressed in K. In Figure 7.1, the emissive power spectrum obtained using the Planck's equation is shown, along with the locus of Wien's equation.

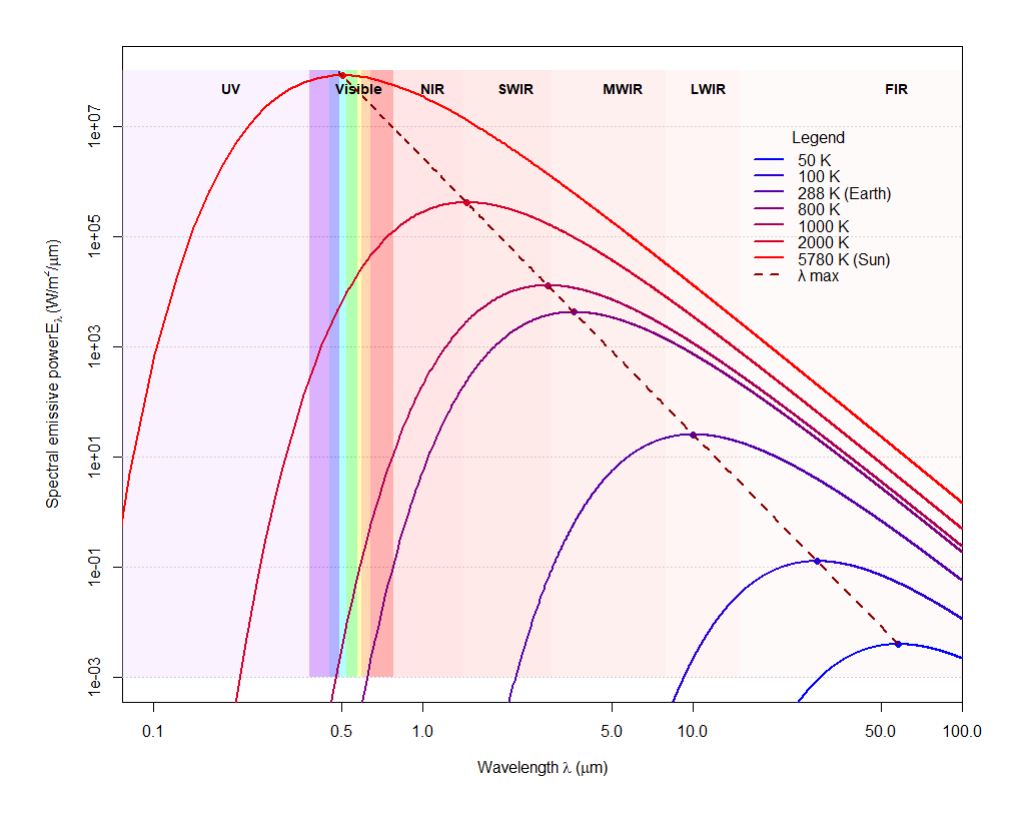


Figure 7.1 – Spectral emissive power vs wavelength

It can be observed that as the emitted power increases,  $\lambda_{max}$  shifts toward shorter wavelengths and the temperature increases. The dominant wavelength  $\lambda_{max}$  helps determine the most appropriate wavelength for the detection instruments used in remote sensing, according to the temperature of the observed object. For example, considering the Sun's surface as a blackbody, it emits at a temperature of about 5800 K, with a peak around 0.5  $\mu$ m, corresponding to the visible yellow/green band. In contrast, objects with lower temperatures exhibit peak emission at longer wavelengths. In fact, the Earth's surface, with an average temperature of about 288 K, emits mostly around 10  $\mu$ m, in the TIR range.

### 7.2 Resolution of Thermal Images

The quality of thermal images obtained through remote thermal surveys depends heavily on their spatial and radiometric resolution. These two resolutions are closely linked. Specifically, they have an inverse relationship, meaning that improving one necessarily reduces the other. A crucial factor in influencing resolutions is the Instantaneous Field of View (IFOV), which represents the smallest target size detectable by an imaging system and represents one pixel

of the sensor array, determining the smallest resolvable object size. The IFOV can be calculated using the following formula (Massimo Micieli, 2019):

$$IFOV = \frac{p}{f} \tag{Eq. 7.4}$$

Where p is the side dimension of the pixel element (expressed in mm) and f is the focal length of the sensor (expressed in mm). The generated IFOV is typically measured in radians or milliradians, representing the solid angle through which the individual pixel "looks" at the scene. When considering resolution, it is important to consider the ground area covered by each pixel, also known as Ground Sample Distance (GSD), which is a function of the distance from the sensor (h) and the IFOV, through the relationship (Massimo Micieli, 2019):

$$GSD = h \cdot IFOV \tag{Eq. 7.5}$$

GSD is typically expressed in m/pixel. It is observed that at a constant distance from the object, the wider the IFOV, the larger the GSD. This leads to a decrease in spatial resolution and an increase in radiometric resolution, as the sensor receives a more intense and detailed thermal signal, as the pixel contains the radiation emitted by a larger surface, and increases the signal-to-noise ratio (SNR). Conversely, smaller IFOVs result in smaller ground areas (lower GSDs) and increase visible detail, generating a better spatial resolution. In this case, the SNR captured on a smaller surface increases, and it shows a negative impact on the radiometric resolution (ODonohue, 2023).

# 7.3 Acquisition and Processing of High-Resolution Thermal and Multispectral Data

Thermal remote sensing, as previously mentioned, is one of the most suitable techniques for studying medium to large scale thermal phenomena. It allows for a better understanding of energy balances, providing useful information regarding the behaviour of different soil types, whether man-made or natural, permeable or impermeable, and different materials that respond according to their characteristics. These acquisitions are essential for a comprehensive understanding of UHIs, as they can detect surface temperatures effectively and accurately.

In this study, the thermal and multispectral data useful for studying the thermal behaviour of the Turin area were acquired on August 15th and 16th, during one of the most significant HWs in the region in 2025, during day and night conditions, respectively. Furthermore, the night of August 16th has already been classified as a tropical night by the analyses carried out in Section 2.2.3. The presence of data acquired during both night and day hours allows to better understand the behaviour of these systems during the hottest periods of the year. The acquisition campaigns were conducted using a CESSNA 4004 aircraft (Figure 7.2), operated by ATV Airborne Sensing Italia Srl, which is specialised in high-precision and high-resolution aerial surveys. The aircraft was equipped with a Dual Digi-THERM (IGI) thermal system (Figure 7.3) consisting of:

- Two Infratec VarioCam HD thermal cameras, sensitive in the 7.5-14 μm range;
- A PhaseOne iXM150 multispectral sensor, for high-resolution RGB imaging.

The survey was designed to capture both thermal and multispectral data over the Municipality of Turin, enabling the analysis of UHI distribution and the detailed mapping of the territory. Specifically, thermal cameras acquired the radiant temperature of surfaces, while the multispectral sensor provided high-resolution RGB images.



Figure 7.2 - Aerial survey aircraft (CESSNA 4004)



Figure 7.3 - Dual Digi-THERM (IGI) thermal system

Table 7.2 summarises the main characteristics of the flight plan, including both the technical aspects and the operational parameters adopted during the acquisitions.

The coverage provided by the 12 flight lines is continuous, and the overlap values allow for the reconstruction of detailed maps of the city. Figure 7.4 shows the 12 flight paths flown by the aircraft during the day and at night, respectively. Thermal images acquired at a flight altitude of approximately 6,300 ft (~ 1,920 m) have a GSD of approximately 100 cm. Each pixel corresponds to about 1 meter on the ground. This resolution allows for the identification of features such as building roofs, roads, or industrial buildings, making it suitable for the purposes of this study. Multispectral images have a lower GSD of approximately 16 cm, corresponding to a higher spatial resolution, with much more detailed pixels that allow for the identification of smaller features. Finally, the quality of satellite positioning was guaranteed using the permanent GNSS TORI and TOGR stations, equipped with LEICA GR30 receivers and precision antennas.

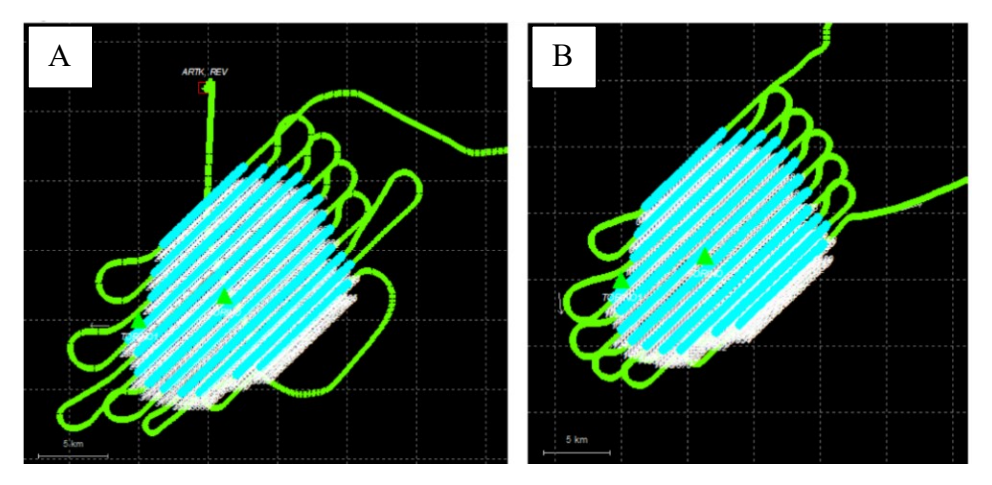


Figure 7.4 - Flight paths for the study: (A) Daytime flight; (B) Nighttime flight

Table 7.2 - Main technical and operational parameters of the flight plan

Parameter	Specification	
Project area	Municipality of Turin	
Aircraft	CESSNA 404	
Flight altitude	~ 6,300 ft	
Number of flight lines	12	
Thermal imaging system	Dual Digi-THERM  (2 × Infratec VarioCam HD,  7.5-14.0 μm, 30 mm, 1024 × 768 px)	
Multispectral sensor	PhaseOne iXM150 (RGB, CMOS, 150 mm, 14,204 × 10,652 px)	
Stabilization platform	Somag GSM	
Navigation system	GPS/INS AeroControl + CCNS-5	
Thermal imagery GSD	~ 100 cm	
Thermal image overlap	77% forward / 40% side	
Multispectral imagery GSD	~ 16 cm	
Multispectral image overlap	90% forward / 50% side	
Daytime survey	15 August 2025 - 12:45 to 14:45 (local time)	
Nighttime survey	16 August 2025 - 03:45 to 05:50 (local time)	
GNSS reference stations	TORI (Turin) and TOGR (Turin MAN INT), equipped with LEICA GR30 receivers	

Once the images captured by the airborne system are obtained, a portion of the study area is selected to carry out the thermal analysis. This approach is chosen because, for the subsequent analyses to be conducted, only the portion of the images that depict the underlying terrain in a way very close to an orthophoto is used. This is due to the insufficient overlap between lateral shots, which prevents the creation of a sufficiently accurate orthophoto of the entire study area for metric or centimeter-level analysis. In general, the construction of an orthophoto is possible, but in this study, due to the required level of

accuracy, it is preferred to select an area that is visually compatible with an orthophoto, where geometric distortions are less significant. This is done by cropping the originally acquired images, keeping only 35% of the original width, starting from the side corresponding to the camera acquisition, which can be either right or left.

In the specific case of this study, the following thermal images falling within the study area are selected:

- TR 07 3041, Flight strip 7, image N. 20, camera right (daytime acquisition 15/08);
- TR 07 3045, Flight strip 7, image N. 24, camera right (daytime acquisition 15/08);
- TR 07 3049, Flight strip 7, image N. 28, camera right (daytime acquisition 15/08);
- TR 07 1377, Flight strip 7, image N. 21, camera right (nighttime acquisition 16/08);
- TR\_07\_1381, Flight strip 7, image N. 25, camera right (nighttime acquisition 16/08);
- TR 07 1385, Flight strip 7, image N. 29, camera right (nighttime acquisition 16/08).

Daytime thermal images on the selected area are acquired at 13:46 local time, while nighttime thermal images are taken at 04:40 local time. The fact that the daytime acquisition time is very close to the solar noon on that specific day (occurring at 13:34) allows for a minor approximation of about ten minutes, enabling the thermal data to be considered as captured during the daily solar peak. This supports the use of the previously calculated shading and irradiation models.

The choice of this area is also influenced by the availability of corresponding images acquired at different times. This enables a focused study of the differences in thermal behaviour throughout the day. A further crop is applied to the thermal images to select only the area corresponding to both the daytime and nighttime acquisitions, resulting in a final examined area of 0.43 km², corresponding to approximately 20% of the original study area. This surface portion includes various land cover classes, distributed in a sufficiently homogeneous way to consider the area a good sample for analysing the characteristics of different urban zones.

The thermal images are georeferenced using QGIS. To georeferenced the images acquired on August 15th, a total of 282 ground control points are used, while for the nighttime acquisition on August 16th, 339 ground control points are used. The used GCPs can be visualised in Figure 7.5 and a more detailed description is available in Table 7.3.

The selection of ground control points is done visually using the available orthophoto, with recognizable buildings, roads, and other surfaces as references. The georeferencing method used is a third-degree polynomial transformation, which visually produces the best results among the available options, but requires many ground control points distributed across the entire area to be georeferenced. This method is chosen due to the need to correct the slight deformations in the images, especially on the outer edges, since the images are not orthorectified.

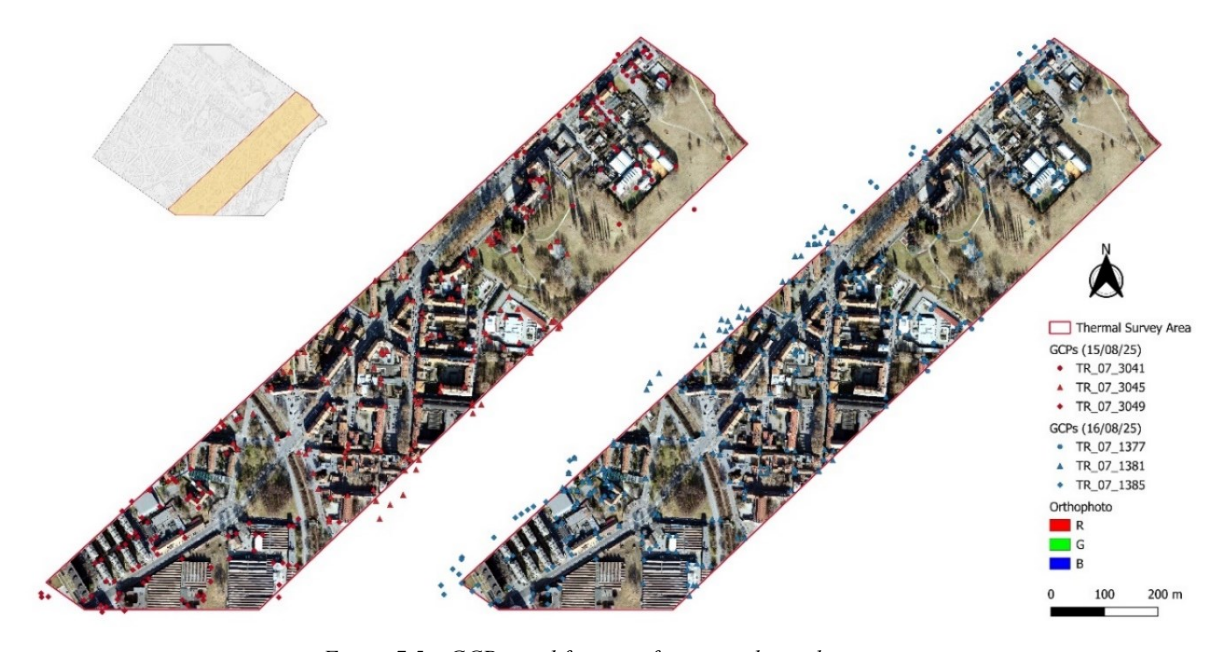


Figure 7.5 – GCPs used for georeferencing thermal imagery

Table 7.3 - Characteristics of GCPs

Time	Total GCPs	ID	Count
Day (13:46)	282	TR_07_3041	67
		TR_07_3045	134
		TR_07_3049	81
Night (04:40)	339	TR_07_1377	101
		TR_07_1381	172
		TR_07_1385	66

Georeferencing process is performed in the reference system EPSG:32632 (WGS 84 / UTM Zone 32N). In Figure 7.6, the spatial distribution of the temperatures acquired during the daytime flight is shown. It is visually possible to distinguish areas with lower surface temperature from those with higher surface temperature. Specifically, it is visible how trees and green areas are cooler than roads and buildings. The maximum temperature recorded in this analysed area is 62.1 °C, while the minimum temperature is 24.7 °C. Further information and detailed statistical analyses are discussed in the next chapter.

Figure 7.7 shows the spatial distribution of the temperatures acquired during the nighttime flight. In this case, the scenario is different. Buildings, green areas, and trees show lower temperatures, while roads show high temperatures. The maximum temperature recorded in this area is 28.4 °C, while the minimum temperature is 11.1 °C. As previously explained, the temperatures do not correspond exactly to the ground temperature, but represent the temperatures as detected by the sensor. However, considering very high surface emissivity values, the recorded temperature can be approximated to the true surface temperature. Finally, it is interesting to see how the temperatures recorded at corresponding points change between nighttime and daytime. This variation mostly depends on the thermal behaviour of the surfaces, but can also be influenced by the SVF. As already mentioned in previous chapters, areas with very high SVF values can reach very high temperatures during the day, and reach very low minimums at night due to heat dissipation. Areas with very low SVF values tend to have a much smaller temperature variation between day and night, since they are more shaded during the day and at night heat dissipation is limited by surrounding obstacles. This behaviour is visible in Figure 7.8, where the temperature variation between day and night shows a minimum value of 3.2 °C and a maximum value of 41.8 °C. The largest temperature differences occur over buildings, while lower values occur over roads and trees. Further statistical investigations confirm what is observed in the figures.



Figure~7.6 - Daytime~temperature

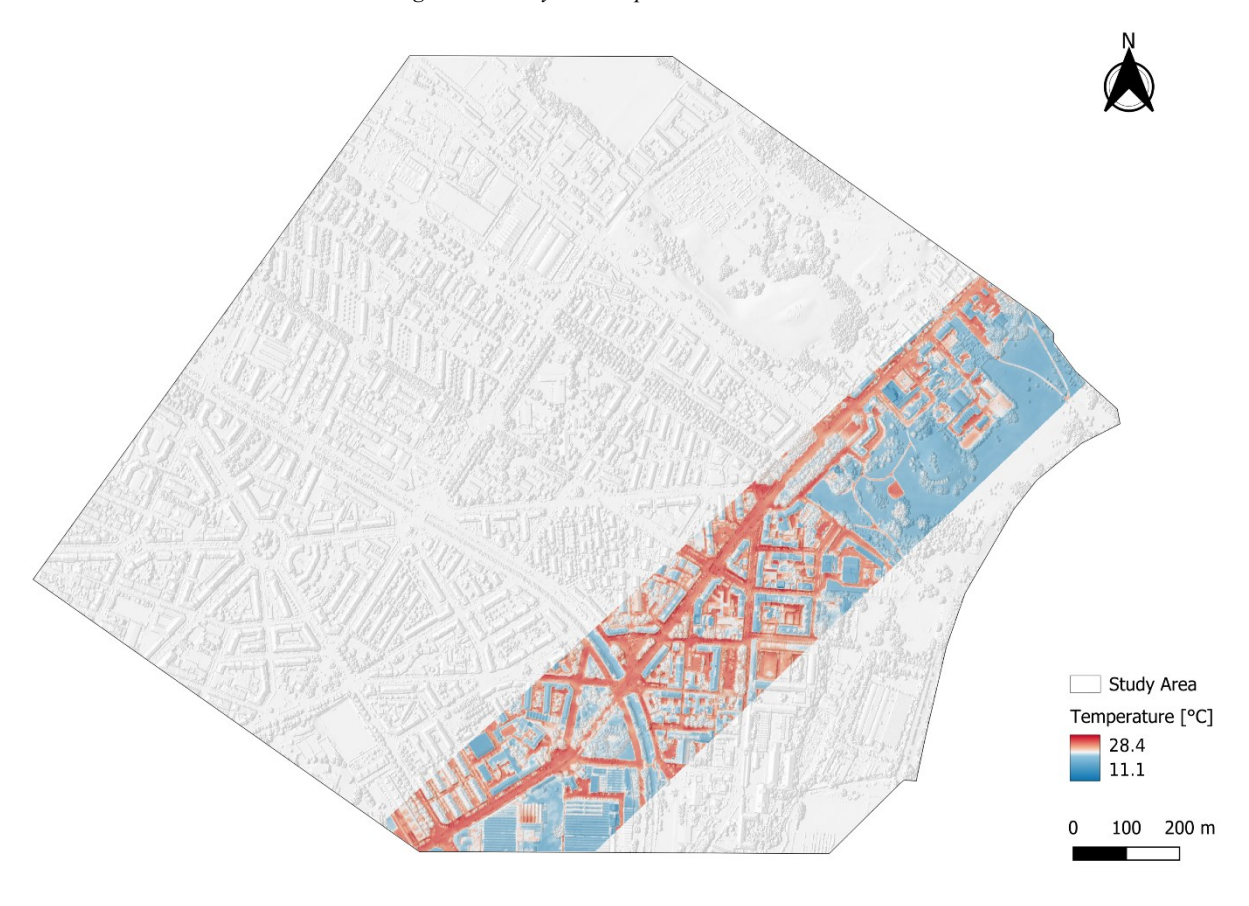


Figure 7.7 - Nighttime temperature



Figure 7.8 -  $\Delta T$  (day-night temperature difference)

An important step involves verifying that the areas classified as shaded through previous modelling correspond to surfaces with lower temperatures. This can be observed in Figure 7.9, which provides a visual comparison confirming that the shading model aligns with both the data acquisition time and the actual shape of the shadow. This correspondence validates the accuracy of the model and supports the continuation of the shading analysis, as lower surface temperatures are clearly concentrated within the areas identified as shaded.

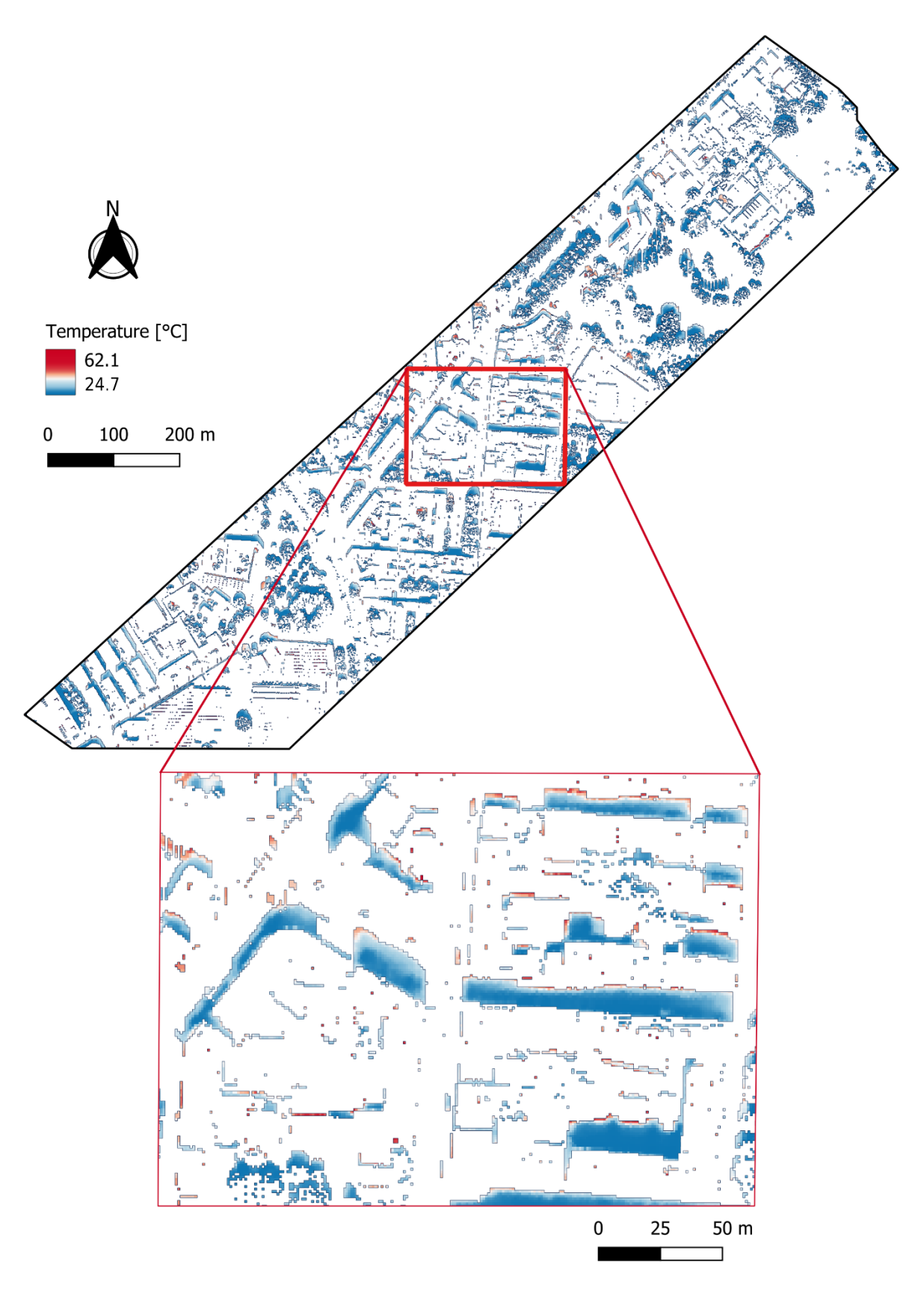


Figure 7.9 - Visual validation of the shading model

# 8. Statistical Analysis

In this section of the study, it is analysed in detail, through appropriate statistical analyses, the relationships between temperature, solar irradiance, and Sky View Factor. In particular, all this is also analysed through the different soil classes in which the points fall, or through the previously classified SVF and solar irradiance classes. Specifically, for all these analysed variables, a statistical analysis was performed to calculate descriptive statistics such as mean, median, standard deviation, minimum and maximum values, quartiles and the interquartile range. Then, comparisons between the means of the different groups considered were also carried out, depending on the phenomenon considered, to verify if statistically significant differences exist between the means. Preliminary analyses showed that temperature, SVF and solar irradiance data present strong spatial autocorrelation. Therefore, classical and typical analyses for mean comparison such as ANOVA can not be applied. Moreover, for all classes, the assumptions of normality and homogeneity of the data are not satisfied. For this reason, another type of analysis was used to verify the significance of the difference between the means of the various subgroups or groups, using GLS (Generalised Least Squares), which takes into account autocorrelation and therefore does not underestimate the obtained p-value, making it a much more appropriate methodology for this type of data. Statistics were applied to all points in the analysis, while the calculation of the difference in means between classes and the application of GLS used a smaller subsample, for computational reasons. The fact that a reduced sample of 2,000 points per class was used may result in slight differences in the mean differences observed compared to those generated with the full sample, but in statistical terms, this does not affect the significance of the difference.

## 8.1 Day vs Night Temperature Analysis

The first groups analysed were divided into two classes: day and night, in order to observe the temperature differences in the analysed area between daytime and nighttime thermal data. The results are visible in Figure 8.1 and Table 8.1 and Table 8.2. It is evident that the temperatures recorded during the day are much higher than those recorded at night, with an average of 39.7 °C compared to 22.6 °C recorded at night, and a mean difference of 16.9 °C, which is statistically significant.

Table 8.1 - Descriptive statistics of temperature for daytime and nighttime acquisitions

Class	Mean (°C)	Median (°C)	SD	Min (°C)	Q1 (°C)	Q3 (°C)	Max (°C)	IQR (°C)
Day	39.7	40.2	6.03	24.7	34.3	43.9	62.1	9.57
Night	22.6	22.5	1.99	11.1	21.2	24.3	28.4	3.07

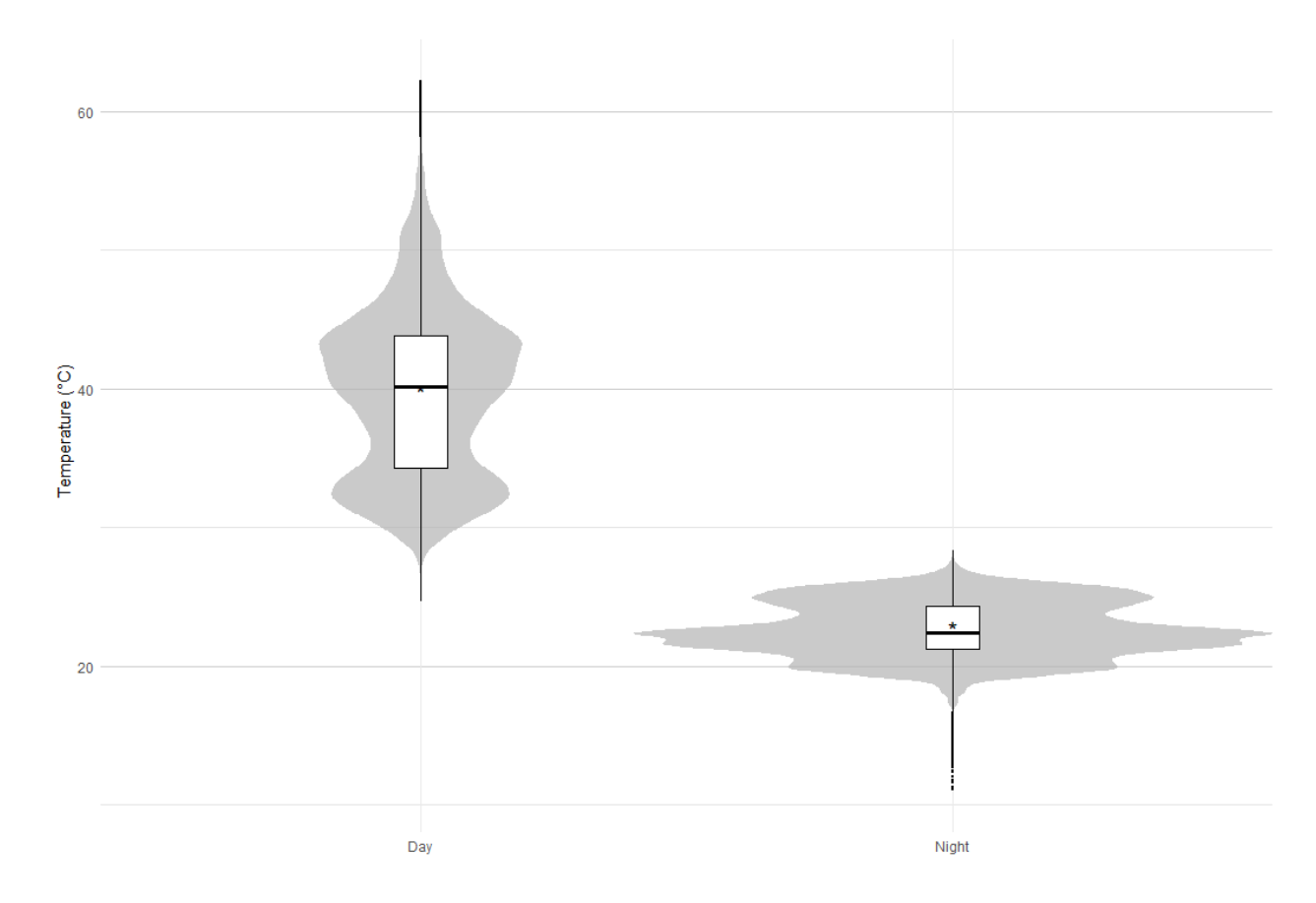


Figure 8.1 - Temperature distribution: Day vs Night

Table 8.2 - Mean temperature difference between day and night

Comparison	Estimate (°C)	SE	t-ratio	p-value
Day - Night	16.9	0.265	63.852	<0.0001 ***

#### 8.2 Temperature by Land Cover Class

The data were also divided into subsections to observe the temperature differences among different land use types such as trees, green areas, roads, and buildings, during the day (Figure 8.2, Table 8.3 and Table 8.4) and during the night (Figure 8.3, Table 8.5 and Table 8.6).

In the first case it is possible to observe that the coolest class on average is that of trees, with a mean of 33.1 °C, followed by green areas, roads, and buildings. The latter class has the highest mean temperature of around 45 °C and also the maximum value recorded in the sample of 62.1 °C. All mean differences between these classes are statistically significant, showing that the temperatures recorded for each class behave differently depending on the type of soil.

The behaviour at night is different, as the class with the lowest mean temperature is no longer that of trees, but green areas, with a mean of around 21.0 °C, followed on average by buildings, trees and roads. It is possible to see how roads at night represent the class with the highest mean temperature, with average values around 25 °C. In this case, all differences between classes are statistically significant except for the mean difference between buildings and green areas.

Table 8.3 - Daytime temperature statistics for different soil classes

Class	Mean (°C)	Median (°C)	SD	Min (°C)	Q1 (°C)	Q3 (°C)	Max (°C)	IQR (°C)
Trees	33.1	32.5	2.88	24.7	31.5	33.8	52.4	2.29
Green Areas	37.2	37.7	4.31	26.6	33.7	40.5	55.5	6.70
Roads	40.0	41.4	4.41	27.6	37.7	43.3	51.6	5.62
Buildings	45.0	45.3	5.35	26.6	41.7	48.7	62.1	6.95

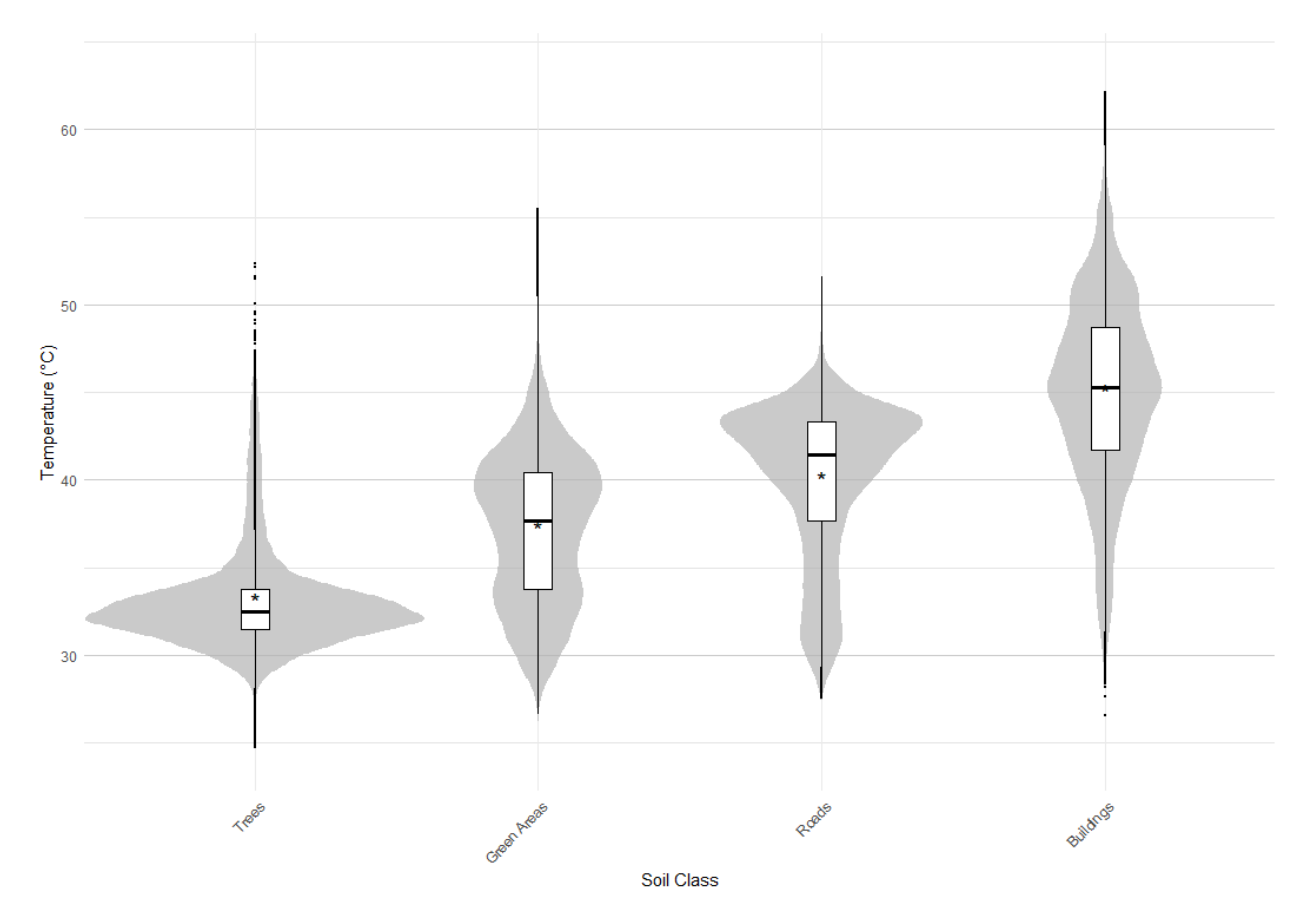


Figure 8.2 - Daytime temperature distribution by soil class

Table 8.4 - Daytime temperature differences between soil classes

Comparison	Estimate (△°C)	SE	t-ratio	p-value
Trees - Green Areas	-4.1	0.50	-8.20	<0.0001 ***
Trees - Roads	-6.9	0.52	-13.27	<0.0001 ***
Trees - Buildings	-11.9	0.46	-25.66	<0.0001 ***
Green Areas - Roads	-2.8	0.48	-5.83	<0.0001 ***
Green Areas - Buildings	-7.8	0.43	-18.14	<0.0001 ***
Roads - Buildings	-5.1	0.42	-12.13	<0.0001 ***

Table 8.5 - Nighttime temperature statistics for different soil classes

Class	Mean (°C)	Median (°C)	SD	Min (°C)	Q1 (°C)	Q3 (°C)	Max (°C)	IQR (°C)
Trees	22.2	22.2	0.97	18.7	21.6	22.7	27.2	1.01
Green Areas	21.0	20.7	1.40	18.2	19.9	21.9	27.7	2.07
Roads	25.0	25.1	1.03	18.5	24.4	25.7	28.4	1.24
Buildings	21.8	21.8	1.51	11.1	21.0	22.8	27.6	1.76

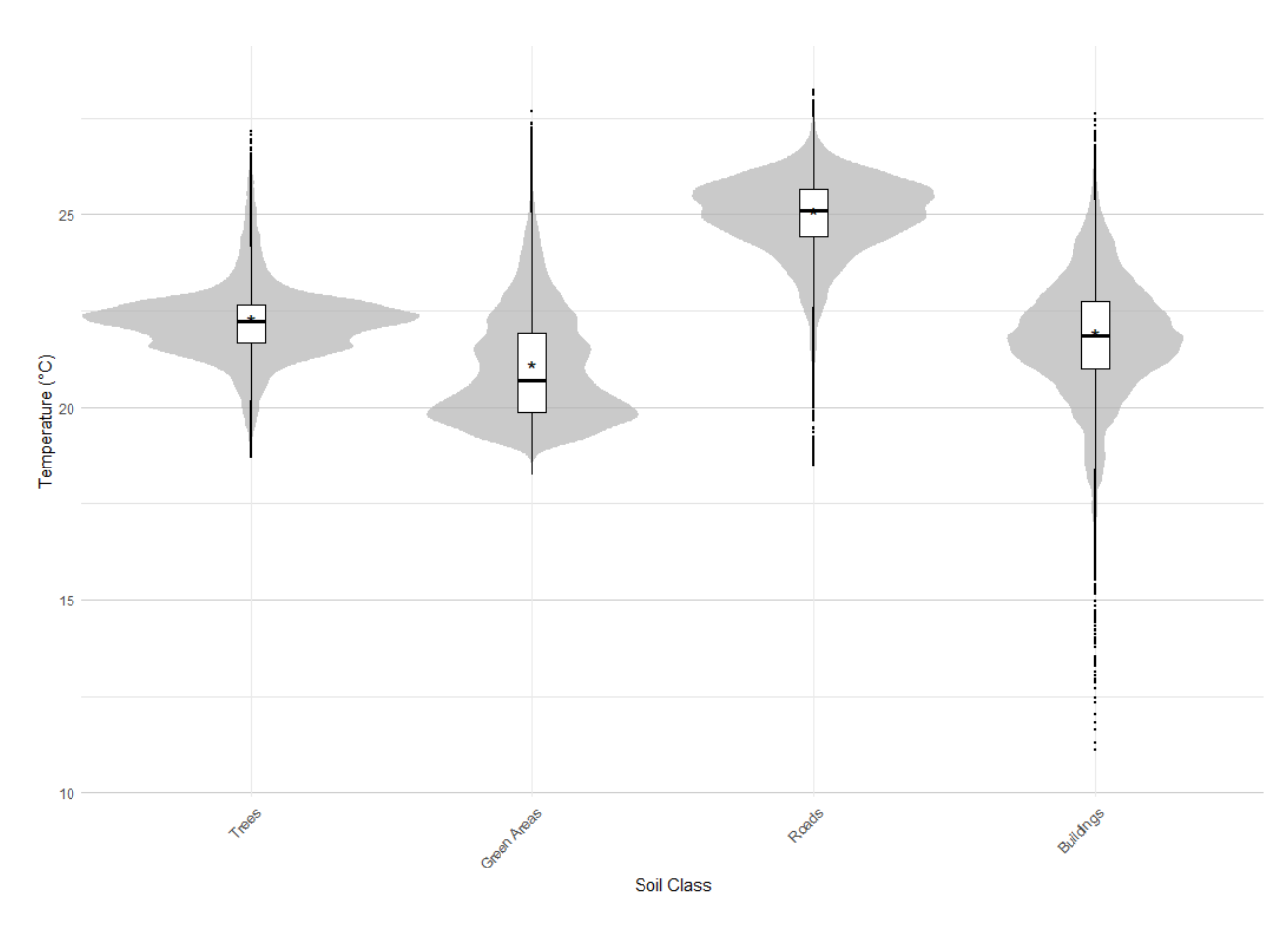


Figure 8.3 - Nighttime temperature distribution by soil class

Table 8.6 - Nighttime temperature differences between soil classes

Comparison	Estimate ( $\Delta$ °C)	SE	t-ratio	p-value
Trees - Buildings	0.849	0.122	6.960	<0.0001 ***
Trees - Roads	-2.345	0.123	-19.087	<0.0001 ***
Trees - Green Areas	0.557	0.111	5.008	<0.0001 ***
Buildings - Roads	-3.193	0.107	-29.826	<0.0001 ***
Buildings - Green Areas	-0.292	0.117	-2.490	0.0622
Roads - Green Areas	2.901	0.124	23.380	<0.0001 ***

## 8.3 Day-Night Temperature Differences by Land Cover

The difference in temperature between daytime and nighttime was then analysed for the different soil classes to evaluate how temperatures vary within the various types of land cover depending on their thermal properties (Figure 8.4, Table 8.7 and Table 8.8). As expected, the smallest thermal differences between day and night were observed within the tree class, with a mean temperature difference of about 10.9 °C, followed by roads, green areas, and buildings. Specifically, roads have a mean temperature difference of around 16.2 °C and, also being the warmest class at night, this means they tend to retain heat longer and dissipate it more slowly. Buildings, on the other hand, show the highest ΔT between day and night, with a mean difference of about 23.2 °C, a very high value. This is influenced by the fact that, unlike roads which have low SVF values and are built with materials such as asphalt and concrete that prevent heat dispersion, buildings are located at higher elevations, with much higher SVF and release heat much more easily when there is no solar irradiance. In this case, all mean differences are statistically significant except for the difference in mean between roads and green areas.

Table 8.7 - Descriptive statistics of  $\Delta T$  between soil classes

Class	Mean (°C)	Median (°C)	SD	Min (°C)	Q1 (°C)	Q3 (°C)	Max (°C)	IQR (°C)
Trees	10.9	10.3	2.74	3.3	9.33	11.5	30.6	2.17
Green Areas	16.2	16.9	4.73	5.0	12.2	20.1	33.6	7.87
Roads	15.1	16.3	3.94	3.2	13.0	17.8	27.1	4.78
Buildings	23.2	23.5	5.80	3.7	19.6	27.0	41.8	7.37

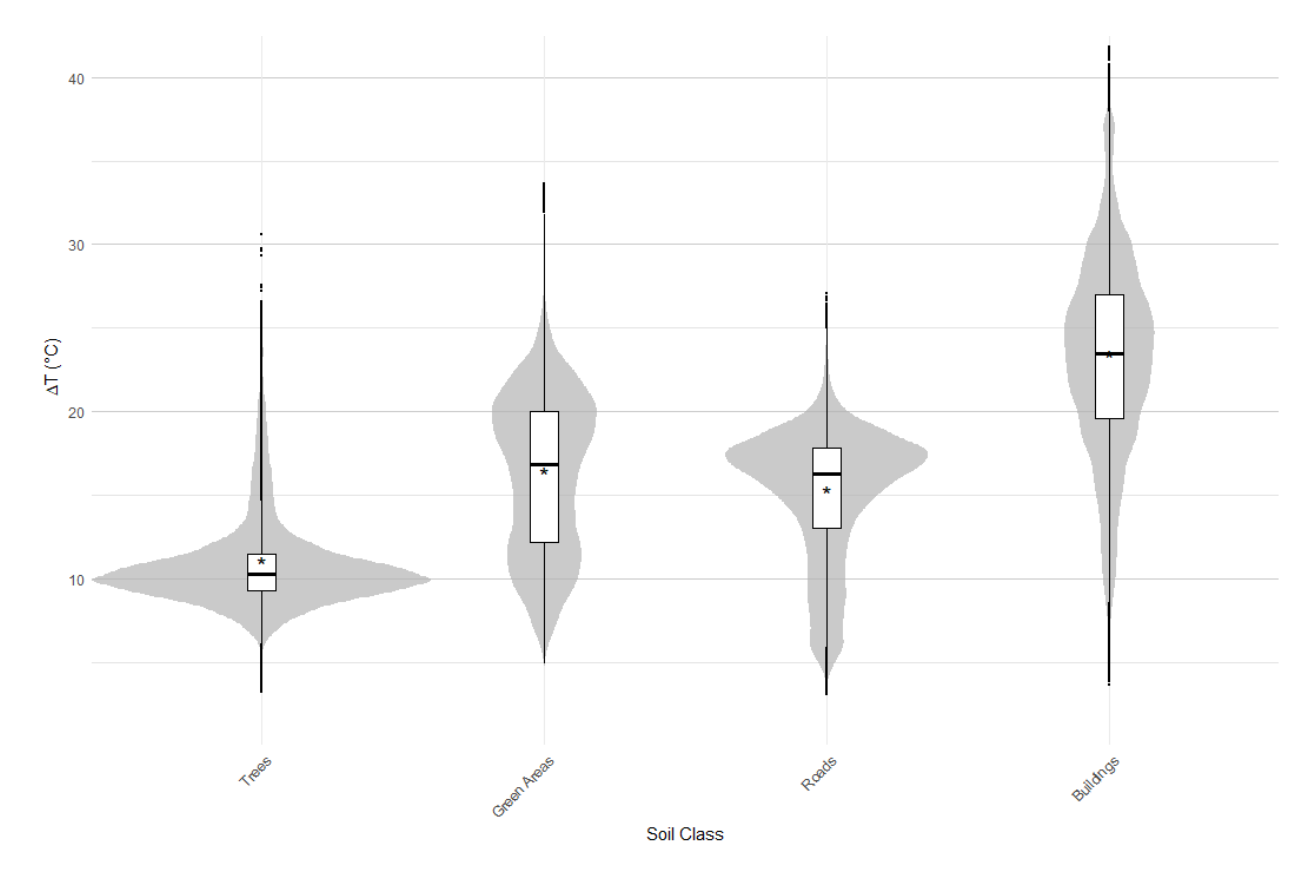


Figure 8.4 -  $\Delta T$  Day-Night distribution by soil class

Table 8.8 - Day-night  $\Delta T$  between soil classes

Comparison	Estimate (°C)	SE	t-ratio	p-value
Trees - Buildings	-12.273	0.492	-24.946	<0.0001 ***
Trees - Roads	-4.033	0.511	-7.896	<0.0001 ***
Trees - Green Areas	-3.858	0.458	-8.422	<0.0001 ***

Buildings - Roads	8.240	0.445	18.537	<0.0001 ***
Buildings - Green Areas	8.415	0.456	18.437	<0.0001 ***
Roads - Green Areas	0.176	0.500	0.351	0.9851

### 8.4 Effect of Shading on Surface Temperature

It is also calculated how shading during daytime hours influences surface temperature. As shown in Figure 8.5, Table 8.9 and Table 8.10, it is possible to see that temperatures in unshaded areas are much higher compared to shaded areas, emphasising the importance of shadow in influencing temperature. The mean temperature recorded in unshaded areas is about 40.8 °C, compared to 34.1 °C in shaded areas, with a statistically significant difference. Furthermore, the influence of shading on the different land cover types was analysed in more detail, as shown in the various violin plots in Figure 8.6 and in Table 8.11 and Table 8.12. All mean differences between shaded and unshaded land cover types are statistically significant, except for the tree class, showing that differences in irradiance on dense vegetation do not significantly influence their surface temperature.

Table 8.9 - Descriptive statistics of temperatures in shaded versus unshaded areas

Class	Mean (°C)	Median (°C)	SD	Min (°C)	Q1 (°C)	Q3 (°C)	Max (°C)	IQR (°C)
Non-Shadow	40.8	41.2	5.70	24.7	36.6	44.5	62.1	7.86
Shadow	34.1	32.8	4.33	24.7	31.0	36.4	56.5	5.39

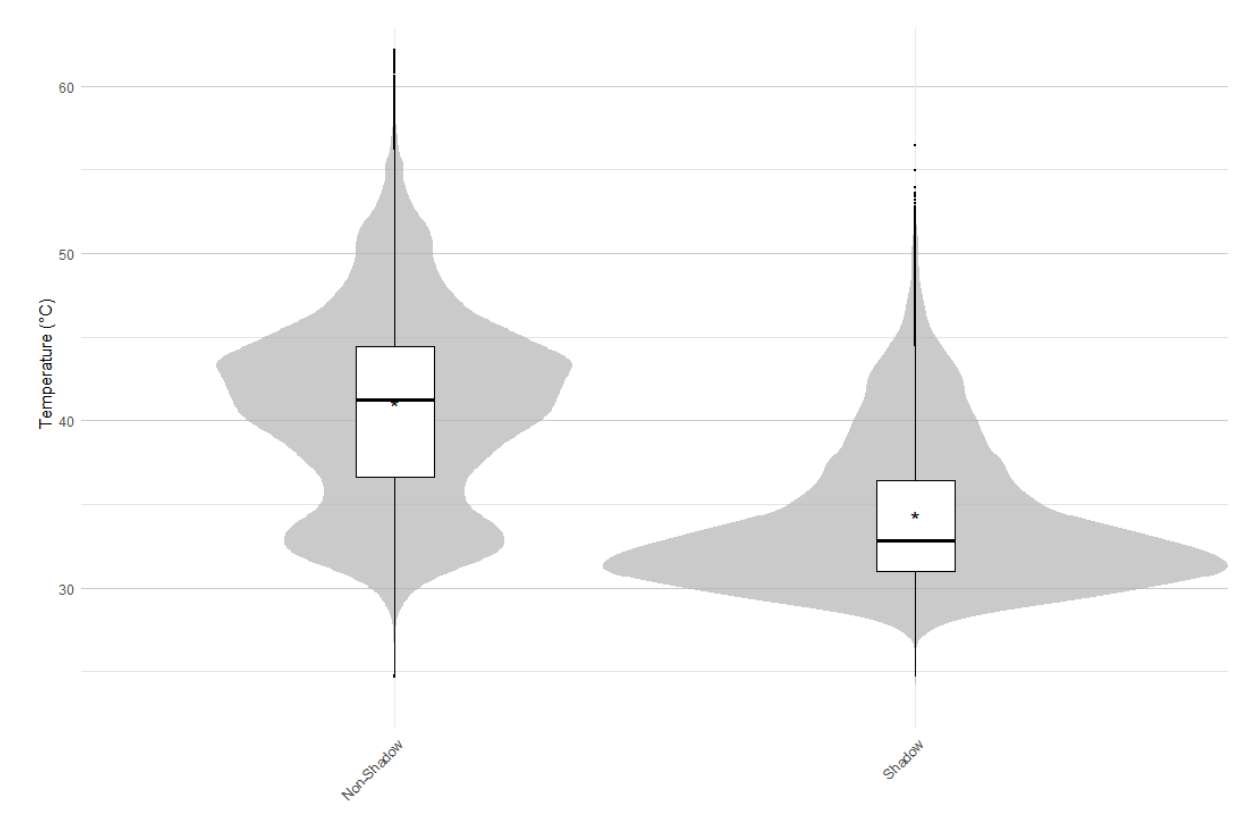


Figure 8.5 - Daytime Temperature: Non-Shadow vs Shadow Areas

 $\it Table~8.10-Comparison~of~temperatures~for~non-shadow~versus~shadow~areas$ 

Comparison	Estimate (°C)	SE	t-ratio	p-value
Non-Shadow - Shadow	6.23	0.453	13.749	<0.0001 ***

Table 8.11 - Descriptive statistics of daytime temperature by soil class and shade

Class	Mean (°C)	Median (°C)	SD	Min (°C)	<i>Q1</i> (°C)	<i>Q3</i> (°C)	<i>Max</i> (° <i>C</i> )	IQR (°C)
Trees,Non-Shadow	33.3	32.7	2.92	24.7	31.7	34.0	52.4	2.29
Trees Shadow	32.7	32.0	3.17	24.8	30.8	33.4	52.4	2.53
Green Areas Non-Shadow	38.1	38.6	3.87	26.7	35.2	40.8	55.5	5.60
Green Areas Shadow	32.9	32.0	3.60	26.6	30.4	34.4	52.5	4.05
Roads Non-Shadow	41.4	42.2	3.23	27.9	40.0	43.6	51.6	3.61
Roads Shadow	34.3	33.3	4.09	27.6	31.0	36.9	48.1	5.91

Buildings Non-Shadow	45.3	45.5	5.12	26.6	42.1	48.8	62.1	6.72
Buildings Shadow	38.3	37.7	5.73	28.2	33.5	42.5	56.5	9.05

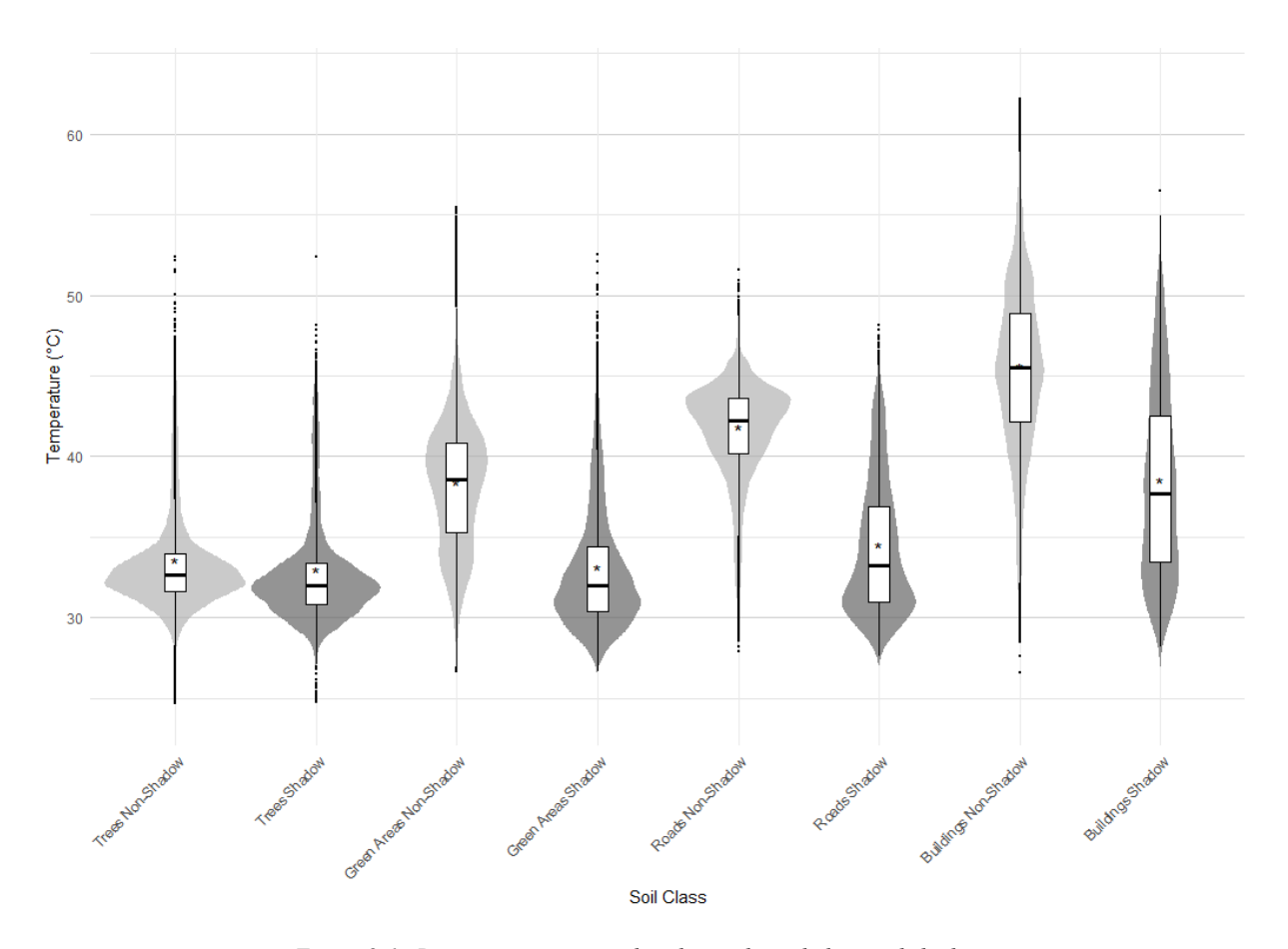


Figure 8.6 - Daytime temperature distribution by soil class and shadow

 $\it Table~8.12-Differences~in~temperature~shadow~vs~non-shadow~areas~between~soil~classes$ 

Contrast	Estimate	SE	t.ratio	p.value
Buildings Non-Shadow - Buildings Shadow	6.08	0.94	6.50	<0.0001 ***
Buildings Non-Shadow - Green Non- Shadow	6.68	0.46	14.63	<0.0001 ***
Buildings Non-Shadow - Green Shadow	10.36	0.68	15.34	<0.0001 ***
Buildings Non-Shadow - Roads Non- Shadow	2.72	0.43	6.28	<0.0001 ***

Buildings Non-Shadow - Roads Shadow	9.60	0.64	15.01	<0.0001 ***
Buildings Non-Shadow - Trees Non- Shadow	10.21	0.45	22.80	<0.0001 ***
Buildings Non-Shadow - Trees Shadow	10.21	0.66	15.43	<0.0001 ***
Buildings Shadow - Green Non- Shadow	0.60	1.01	0.59	0.9990
Buildings Shadow - Green Shadow	4.28	1.13	3.78	0.0041 **
Buildings Shadow - Roads Non- Shadow	-3.36	1.00	-3.37	0.0180 *
Buildings Shadow - Roads Shadow	3.52	1.09	3.22	0.0291 *
Buildings Shadow - Trees Non- Shadow	4.13	1.01	4.09	0.0012 **
Buildings Shadow - Trees Shadow	4.13	1.12	3.68	0.0060 **
Green Non-Shadow - Green Shadow	3.69	0.67	5.47	<0.0001 ***
Green Non-Shadow - Roads Non- Shadow	-3.96	0.50	-7.86	<0.0001 ***
Green Non-Shadow - Roads Shadow	2.92	0.71	4.14	0.0010 **
Green Non-Shadow - Trees Non- Shadow	3.53	0.45	7.81	<0.0001 ***
Green Non-Shadow - Trees Shadow	3.54	0.67	5.30	<0.0001 ***
Green Shadow - Roads Non-Shadow	-7.65	0.71	-10.75	<0.0001 ***
Green Shadow - Roads Shadow	-0.76	0.86	-0.88	0.9877
Green Shadow - Trees Non-Shadow	-0.16	0.67	-0.23	1.0000
Green Shadow - Trees Shadow	-0.15	0.81	-0.19	1.0000
Roads Non-Shadow - Roads Shadow	6.89	0.64	10.71	<0.0001 ***
Roads Non-Shadow - Trees Non- Shadow	7.49	0.48	15.76	<0.0001 ***
Roads Non-Shadow - Trees Shadow	7.50	0.68	11.09	<0.0001 ***

Roads Shadow - Trees Non-Shadow	0.61	0.69	0.88	0.9880
Roads Shadow - Trees Shadow	0.61	0.84	0.73	0.9962
Trees Non-Shadow - Trees Shadow	0.00	0.64	0.01	1.0000

## 8.5 SVF by Land Cover Class

In the following analyses, the SVF is analysed in more detail. In particular, the graph shown in Figure 8.7 and the tables below (Table 8.13 and Table 8.14) display the distribution of SVF values across different land cover classes. On average, the lowest SVF values are recorded for roads, while the highest are recorded in the buildings class. All differences in means are statistically significant, except for the difference between roads and green areas.

Table 8.13 - Descriptive statistics of SVF by soil class

Class	Mean	Median	SD	Min	Q1	Q3	Max	IQR
Trees	0.672	0.711	0.227	0.0109	0.533	0.855	1	0.322
Green Areas	0.661	0.711	0.235	0.0109	0.503	0.856	1	0.354
Roads	0.614	0.633	0.168	0.0109	0.501	0.740	0.986	0.239
Buildings	0.827	0.882	0.158	0.0109	0.768	0.934	1	0.166

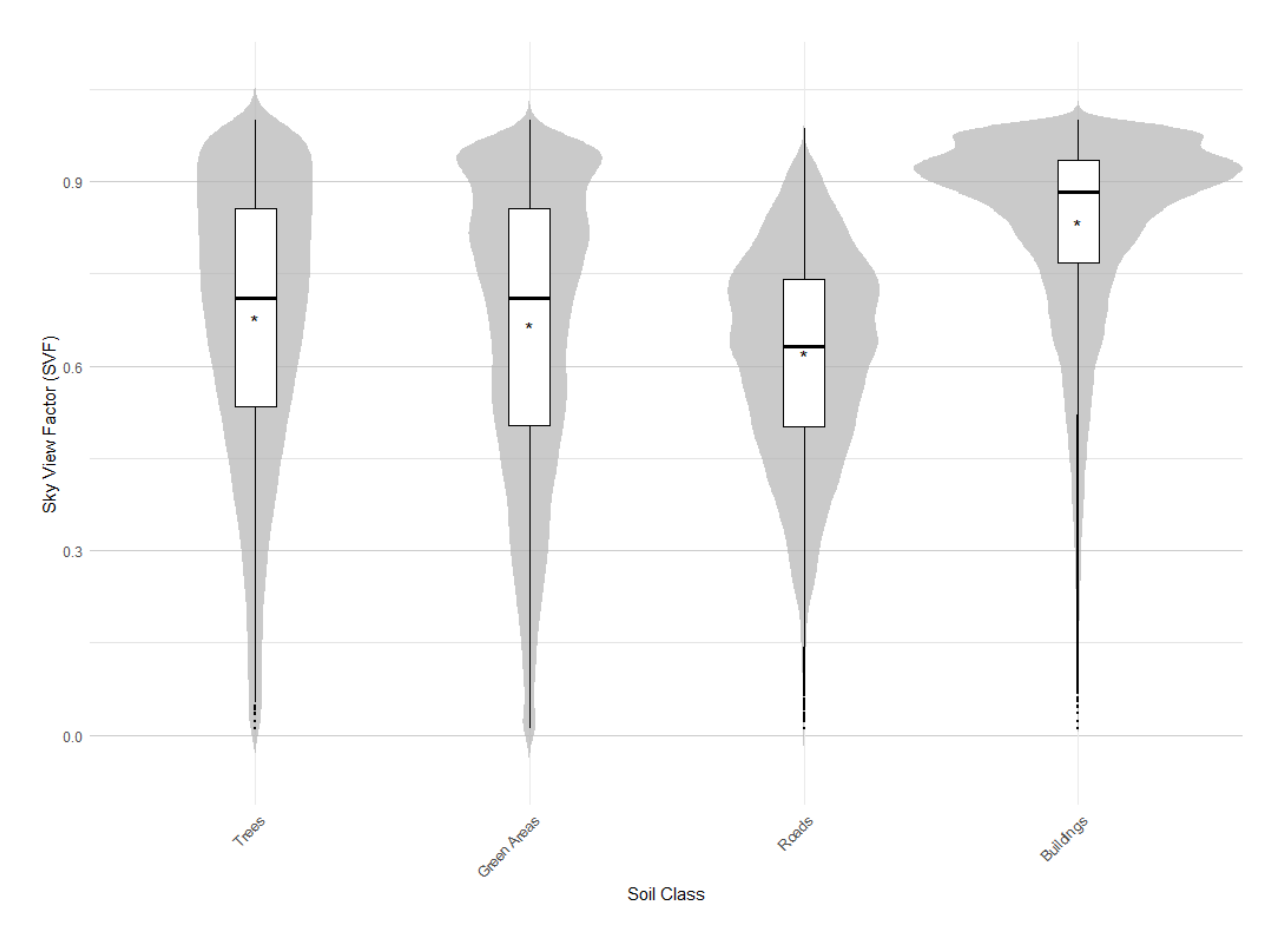


Figure 8.7 - SVF distribution by soil class

Table 8.14 - SVF differences between soil classes

Comparison	Estimate	SE	t-ratio	p-value
Trees - Buildings	-0.1645	0.0203	-8.121	<0.0001 ***
Trees - Roads	0.0915	0.0206	4.445	0.0001 ***
Trees - Green Areas	0.1264	0.0207	6.095	<0.0001 ***
Buildings - Roads	0.2560	0.0185	13.864	<0.0001 ***
Buildings - Green Areas	0.2910	0.0202	14.396	<0.0001 ***
Roads - Green Areas	0.0349	0.0216	1.618	0.3691

#### 8.6 Temperature by SVF Class

Figure 8.8 represent the temperature values based on the SVF class in which the observations fall, separated into daytime temperature (Table 8.15 and Table 8.18), nighttime temperature (Table 8.16 and Table 8.19), and day-night  $\Delta T$  (Table 8.17 and Table 8.20). It is visible that during the day, mean temperature values increase with increasing SVF class, with average values of 34.4 °C in the "Very Low" class and 42.8 °C in the "Very High" class. The same trend is observed in the day-night  $\Delta T$ . A different behaviour is seen in nighttime temperatures. In this case, the highest average temperatures are observed in the "Low" and "Moderate" SVF classes, while the lowest are in the "Very High" class. This emphasises that points with low SVF tend to have smaller average temperature variations between day and night, as there are obstacles that prevent significant cooling. On the other hand, areas with very high SVF (more exposed to the sky) show greater temperature differences between day and night, higher average daytime temperature and lower average nighttime temperatures. This is also demonstrated by Figure 8.9 and Table 8.21, which highlight the presence of a linear relationship between temperature and SVF, that is positive during the day, negative at night, and positive for  $\Delta T$ .

Table~8.15 - Descriptive~statistics~of~day time~temperature~by~SVF~class

Class	Mean (°C)	Median (°C)	SD	Min (°C)	Q1 (°C)	Q3 (°C)	Max (°C)	IQR (°C)
Very Low	34.4	33.1	4.23	24.8	31.4	37.0	56.5	5.61
Low	36.9	36.2	5.23	24.7	32.4	41.1	56.9	8.65
Moderate	39.0	39.5	5.32	24.8	34.3	43.0	61.1	8.68
High	40.9	41.4	5.60	25.1	36.9	44.3	62.1	7.46
Very High	42.8	42.9	6.14	25.1	39.1	46.8	60.6	7.77

Table 8.16 - Descriptive statistics of nighttime temperature by SVF class

Class	Mean (°C)	Median (°C)	SD	Min (°C)	Q1 (°C)	Q3 (°C)	Max (°C)	IQR (°C)
Very Low	22.9	22.7	1.35	13.5	22.0	23.9	27.9	1.90
Low	23.4	23.5	1.63	13.9	22.2	24.7	28.2	2.47
Moderate	23.4	23.4	1.89	14.0	21.9	25.0	28.3	3.11
High	22.4	22.2	2.03	13.1	20.8	24.2	27.5	3.34
Very High	21.3	21.4	1.63	12.6	19.9	22.4	27.7	2.43

Table 8.17 - Descriptive statistics of  $\Delta T$  by SVF class

Class	Mean (°C)	Median (°C)	SD	Min (°C)	Q1 (°C)	Q3 (°C)	Max (°C)	IQR (°C)
Very Low	11.5	10.5	3.78	3.30	8.98	13.5	36.5	4.49
Low	13.5	12.9	4.68	3.18	9.75	16.9	35.3	7.13
Moderate	15.6	15.7	4.85	3.27	11.9	18.6	39.8	6.75
High	18.5	18.1	5.65	3.62	14.9	21.9	41.7	6.97
Very High	21.4	21.6	6.49	3.68	17.9	25.5	39.3	7.58

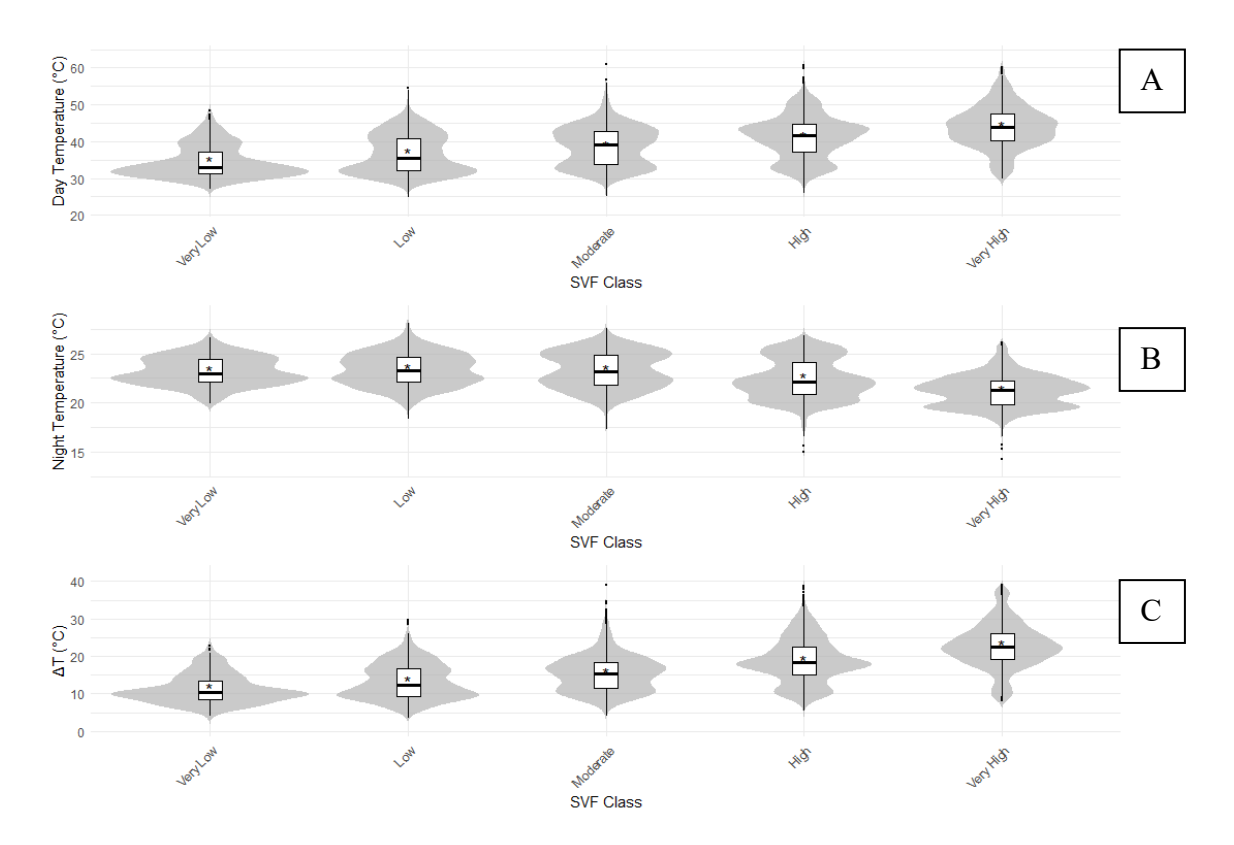


Figure 8.8 - Surface temperature distribution by SVF class: (A) Daytime; (B) Nighttime; and (C)  $\Delta T$ 

Table 8.18 - Daytime temperature differences between SVF classes

Comparison	Estimate (°C)	SE	t-ratio	p-value
Very Low - Low	-1.50	0.773	-1.935	0.2995
Very Low - Moderate	-3.72	0.738	-5.047	<0.0001 ***
Very Low - High	-5.39	0.701	-7.691	<0.0001 ***
Very Low - Very High	-7.09	0.755	-9.388	<0.0001 ***
Low - Moderate	-2.23	0.583	-3.820	0.0013 ***
Low - High	-3.90	0.536	-7.269	<0.0001 ***
Low - Very High	-5.59	0.605	-9.247	<0.0001 ***
Moderate - High	-1.67	0.483	-3.449	0.0053 **
Moderate - Very High	-3.36	0.559	-6.019	<0.0001 ***
High - Very High	-1.69	0.509	-3.331	0.0080 **

Table 8.19 - Nighttime temperature differences between SVF classes

Comparison	Estimate (°C)	SE	t-ratio	p-value
Very Low - Low	-0.305	0.249	-1.229	0.7347
Very Low - Moderate	-0.463	0.237	-1.951	0.2912
Very Low - High	0.651	0.225	2.888	0.0323 *
Very Low - Very High	1.612	0.243	6.643	<0.0001 ***
Low - Moderate	-0.157	0.188	-0.839	0.9183
Low - High	0.956	0.172	5.551	<0.0001 ***
Low - Very High	1.917	0.194	9.866	<0.0001 ***
Moderate - High	1.114	0.155	7.166	<0.0001 ***
Moderate - Very High	2.075	0.180	11.555	<0.0001 ***
High - Very High	0.961	0.164	5.876	<0.0001 ***

Table 8.20 -  $\Delta T$  between SVF classes

Comparison	Estimate (°C)	SE	t-ratio	p-value
Very Low - Low	-1.19	0.761	-1.564	0.5207
Very Low - Moderate	-3.26	0.726	-4.490	0.0001 ***
Very Low - High	-6.04	0.690	-8.757	<0.0001 ***
Very Low - Very High	-8.70	0.743	-11.708	<0.0001 ***
Low - Moderate	-2.07	0.574	-3.607	0.0030 **
Low - High	-4.85	0.527	-9.199	<0.0001 ***
Low - Very High	-7.51	0.595	-12.618	<0.0001 ***
Moderate - High	-2.78	0.476	-5.845	<0.0001 ***
Moderate - Very High	-5.44	0.550	-9.889	<0.0001 ***
High - Very High	-2.66	0.501	-5.303	<0.0001 ***

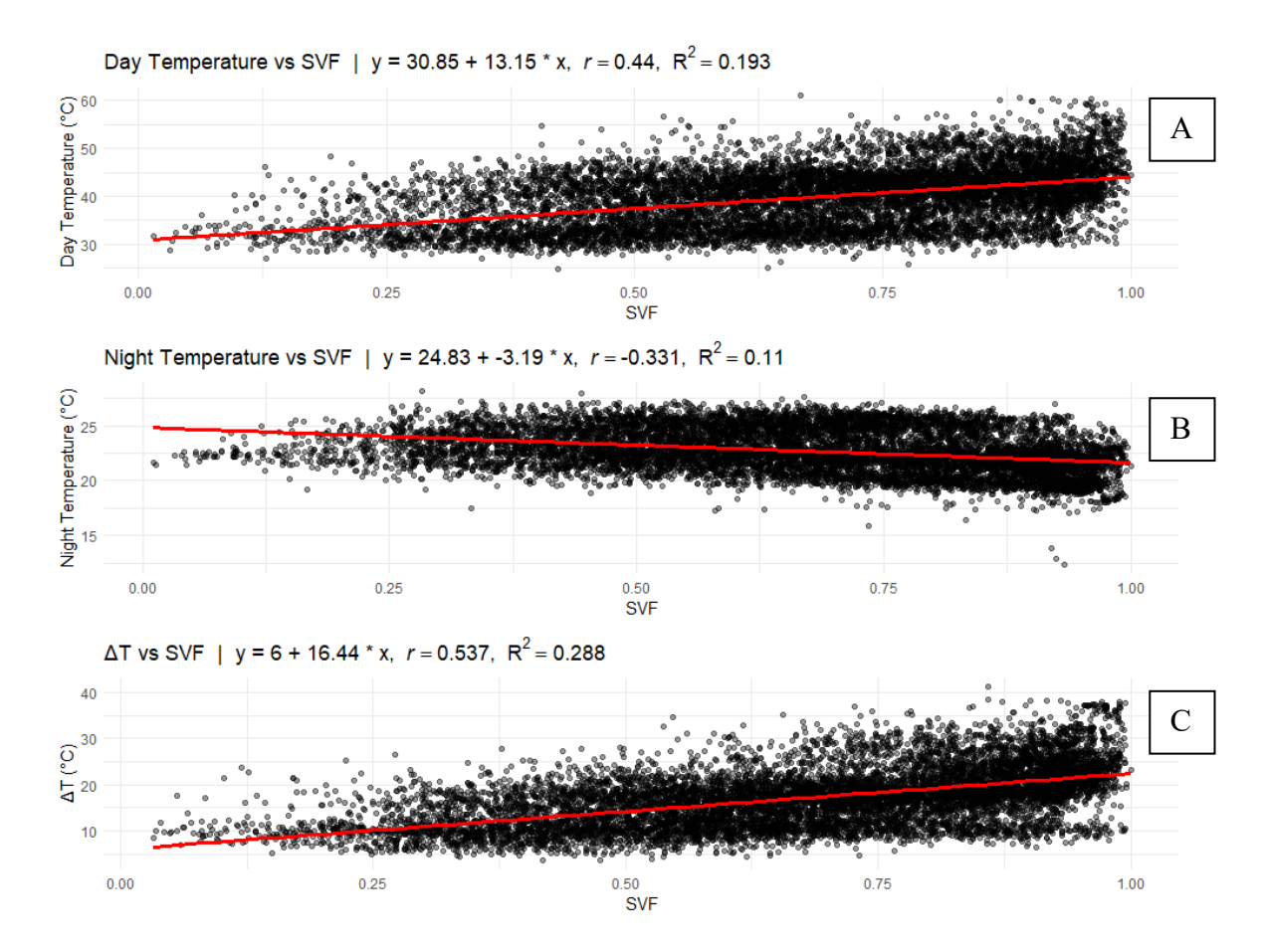


Figure 8.9 - Surface temperature distribution by SVF values with linear regression: (A) Daytime; (B) Nighttime; (C)  $\Delta T$ 

Table 8.21 - Linear regression parameters and t-test for slope of temperature vs SVF

Dataset	Intercept	Slope	t-value (slope)	p-value (slope)	$R^2$	Pearson r
Day Temperature	30.85	13.15	48.93	0 ***	0.193	0.44
Night Temperature	24.83	-3.19	-35.09	1.61e-254 ***	0.11	-0.331
$\Delta T$	6	16.44	63.62	0 ***	0.288	0.537

#### 8.7 Solar Irradiance by Land Cover Class

In this section, the distribution of solar irradiance across soil classes is analysed. The results are shown in Figure 8.10 through the violin plot and in Table 8.22 and Table 8.23. In this case, the presence of shaded and unshaded areas results in a non-unimodal distribution, with two peaks corresponding respectively to very low solar irradiance (in shaded areas) and to higher irradiance (in sun-exposed areas). In this case, the median better describes the variable's behaviour than the mean. Despite this, considering also the mean values, differences in means between the various subgroups of soil classes were analysed, and statistically significant differences were found between trees and buildings, between trees and roads, between trees and green areas and between buildings and green areas. This means that the differences between buildings and roads, and between roads and green areas, do not show statistically significant mean differences, due to the similarity in their distribution of solar irradiance values.

Table 8.22 - Descriptive statistics of total solar irradiance by soil class

Class	$Mean$ $(W/m^2)$	Median (W/m²)	SD	$Min$ $(W/m^2)$	$Q1 \over (W/m^2)$	$Q3 \\ (W/m^2)$	$Max$ $(W/m^2)$	$IQR$ $(W/m^2)$
Trees	435	388	349	49.8	66.8	767	1077	700
Green Areas	695	897	343	50.0	497	913	1076	416
Roads	662	901	365	50.1	106	914	1076	807
Buildings	720	838	307	50.2	607	927	1077	320

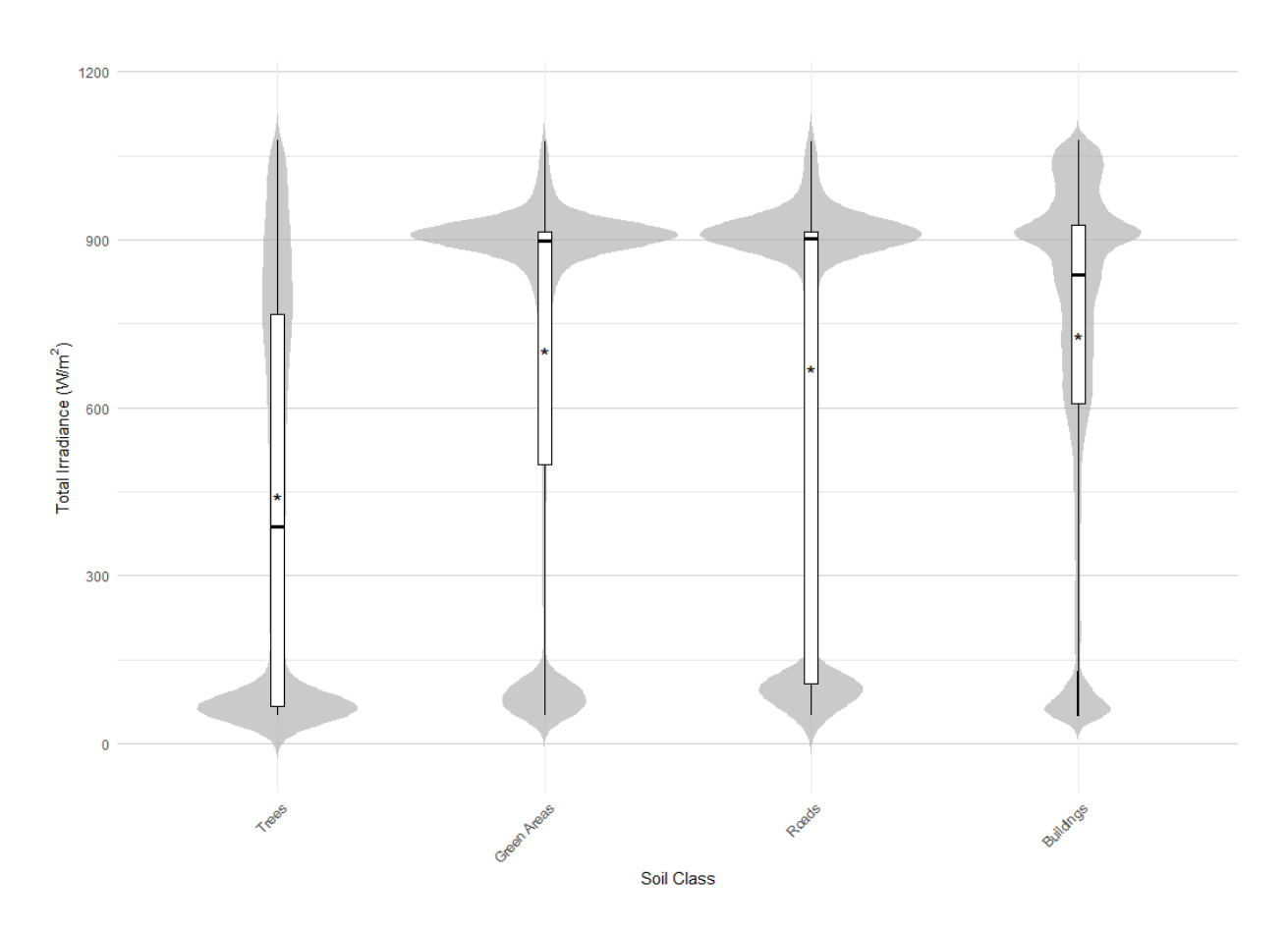


Figure 8.10 - Total solar irradiance distribution by soil class

Table 8.23 - Differences of total solar irradiance between soil classes

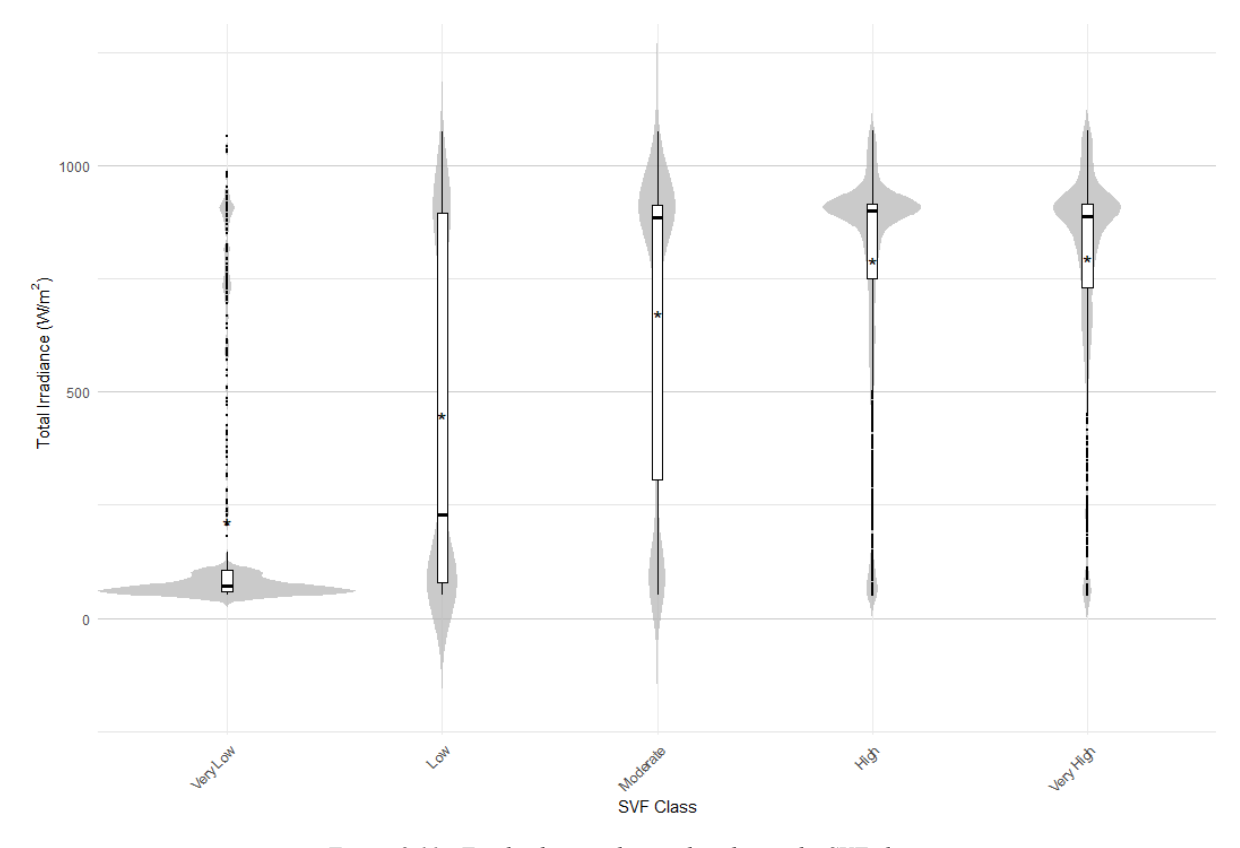
Comparison	Estimate $(W/m^2)$	te $(W/m^2)$ SE		p-value
Trees - Buildings	-296.08	32.7	-9.063	<0.0001 ***
Trees - Roads	-221.41	35.3	-6.272	<0.0001 ***
Trees - Green Areas	-217.63	34.0	-6.393	<0.0001 ***
Buildings - Roads	74.67	30.4	2.459	0.0674
Buildings - Green Areas	78.44	29.7	2.640	0.0437 *
Roads - Green Areas	3.77	33.3	0.113	0.9995

#### 8.8 Solar Irradiance by SVF Class

Finally, the trend of total solar irradiance across the different SVF classes is analysed. According to Figure 8.11, Table 8.24 and Table 8.25, it is visible that the class with a very low SVF shows the lowest irradiance values, with a mean of about 209 W/m². The highest values of total solar irradiance are recorded, as expected, in the very high SVF class, with an average of 783 W/m². All mean differences in total irradiance between the various SVF subclasses are statistically significant except for the mean difference between the "High" and "Very High" classes, which show a similar trend and average values.

Table 8.24 - Descriptive statistics of total solar irradiance by SVF class

Class	Mean (W/m²)	Median (W/m²)	SD	$Min$ $(W/m^2)$	$Q1 \over (W/m^2)$	$Q3  (W/m^2)$	$Max$ $(W/m^2)$	$IQR$ $(W/m^2)$
Very Low	209	71.5	287	50.5	58.8	106	1076	47.3
Low	429	161	382	50.6	75.9	889	1076	813
Moderate	658	876	352	50.6	282	913	1076	632
High	782	900	255	50.6	745	916	1077	171
Very High	783	892	248	50.5	718	916	1077	198



Figure~8.11 - Total~solar~irradiance~distribution~by~SVF~class

Table 8.25 - Differences of total solar irradiance between SVF classes

Comparison	Estimate $(W/m^2)$	SE	t-ratio	p-value
Very Low - Low	-156.30	46.9	-3.336	0.0078 **
Very Low - Moderate	-413.38	45.0	-9.176	<0.0001 ***
Very Low - High	-540.40	43.7	-12.353	<0.0001 ***
Very Low - Very High	-531.29	46.4	-11.443	<0.0001 ***
Low - Moderate	-257.08	30.6	-8.399	<0.0001 ***
Low - High	-384.10	28.7	-13.404	<0.0001 ***
Low - Very High	-374.99	32.6	-11.500	<0.0001 ***
Moderate - High	-127.03	25.6	-4.961	<0.0001 ***
Moderate - Very High	-117.92	30.0	-3.936	0.0008 ***
High - Very High	9.11	28.0	0.326	0.9976

## 8.9 Daytime Temperature by Solar Irradiance Class

The graph in Figure 8.12 and the tables in Table 8.26 and Table 8.27 also analyse the trend of daytime temperature as a function of solar irradiance class. It is possible to observe an increase in temperature with increasing irradiance class. The lowest average values are recorded in the "Very Low" irradiance class, with 34.4 °C, while the highest are in the "Very High" class, with an average temperature of 42.0 °C. Most differences in mean temperatures between irradiance classes are statistically significant, except for the contrasts Very Low - Low, Low - Moderate, and Moderate - High.

Table 8.26 - Descriptive statistics of daytime temperature by solar irradiance class

Class	Mean (°C)	Median (°C)	SD	Min (°C)	Q1 (°C)	Q3 (°C)	Max (°C)	IQR (°C)
Very Low	34.4	33.0	4.66	24.7	31.1	36.8	61.3	5.64
Low	36.8	35.0	5.37	24.8	32.4	40.7	60.0	8.32
Moderate	38.4	37.9	5.82	24.7	33.1	43.2	59.7	10.1
High	40.4	41.0	5.93	25.0	35.0	44.9	62.1	9.86
Very High	42.0	42.0	5.20	25.0	38.8	44.8	62.1	5.96

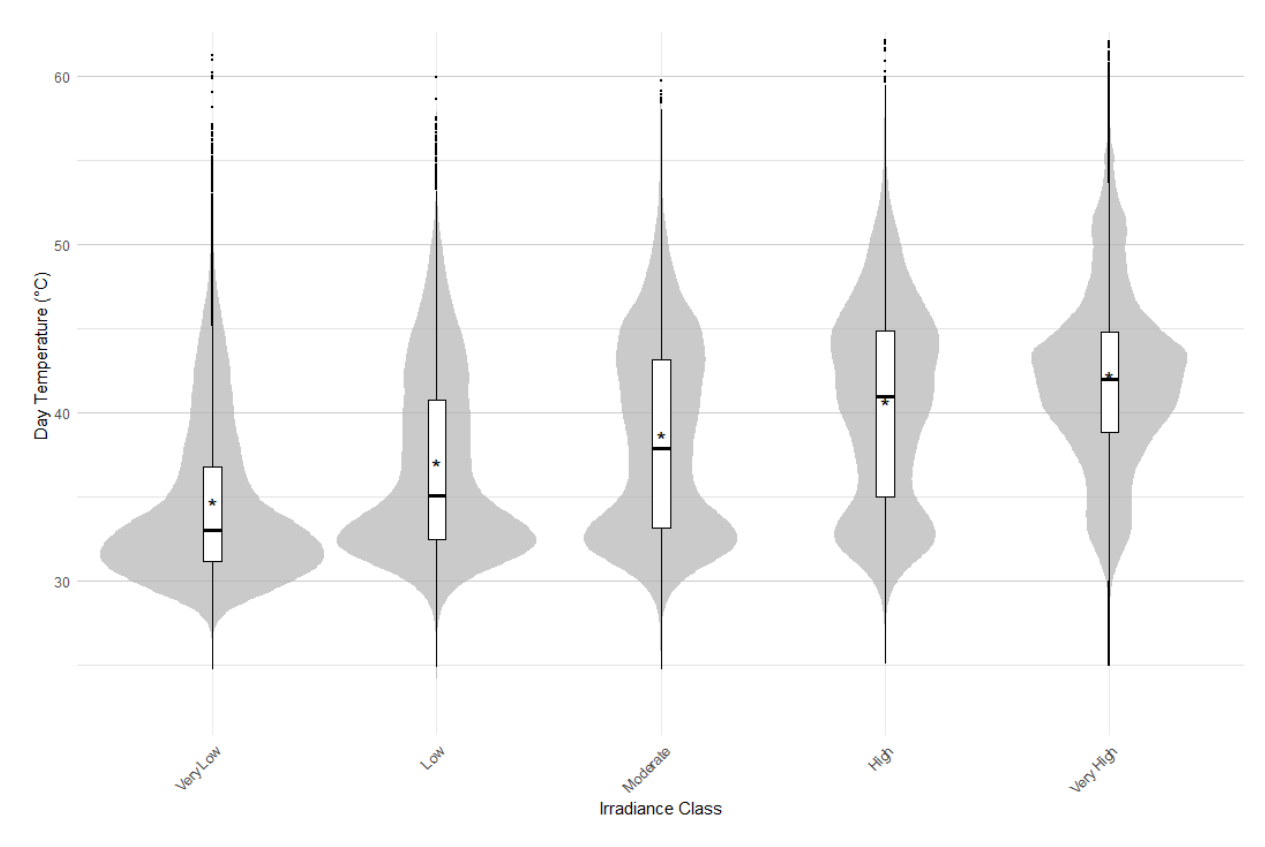


Figure 8.12-Daytime temperature distribution by total solar irradiance class

Table 8.27 - Differences of daytime temperature between solar irradiance classes

Comparison	Estimate (°C)	SE	t-ratio	p-value
Very Low - Low	-1.92	0.796	-2.412	0.1129
Very Low - Moderate	-2.97	0.657	-4.512	0.0001 ***
Very Low - High	-4.29	0.520	-8.246	<0.0001 ***
Very Low - Very High	-5.78	0.364	-15.904	<0.0001 ***
Low - Moderate	-1.05	0.947	-1.104	0.8043
Low - High	-2.37	0.852	-2.782	0.0438 *
Low - Very High	-3.87	0.765	-5.050	<0.0001 ***
Moderate - High	-1.33	0.727	-1.825	0.3600
Moderate - Very High	-2.82	0.622	-4.532	0.0001 ***
High - Very High	-1.49	0.469	-3.183	0.0131 *

A further analysis considers the distribution of irradiance values in relation to the corresponding surface temperature values as continuous variables, represented through a scatter plot that clearly illustrates the relationship between the two variables under investigation (Figure 8.13). The plot uses a sample of 50,000 points to facilitate the visualisation of the distribution. To further aid interpretation, a different colour was assigned to each point according to the pixel's class, distinguishing between shaded and non-shaded areas. The domain characterised by lower total irradiance values is predominantly composed of points classified as shaded. In this region, irradiance values are very low, with a distinct transition occurring around approximately 106 W/m². The second part of the plot, which represents points directly exposed to solar radiation, shows as already highlighted previously a predominant density around 900 W/m². In this section, the temperature range is broader. The mean values between shaded and non-shaded classes differ, as already observed in Section 8.4, in a statistically significant way.

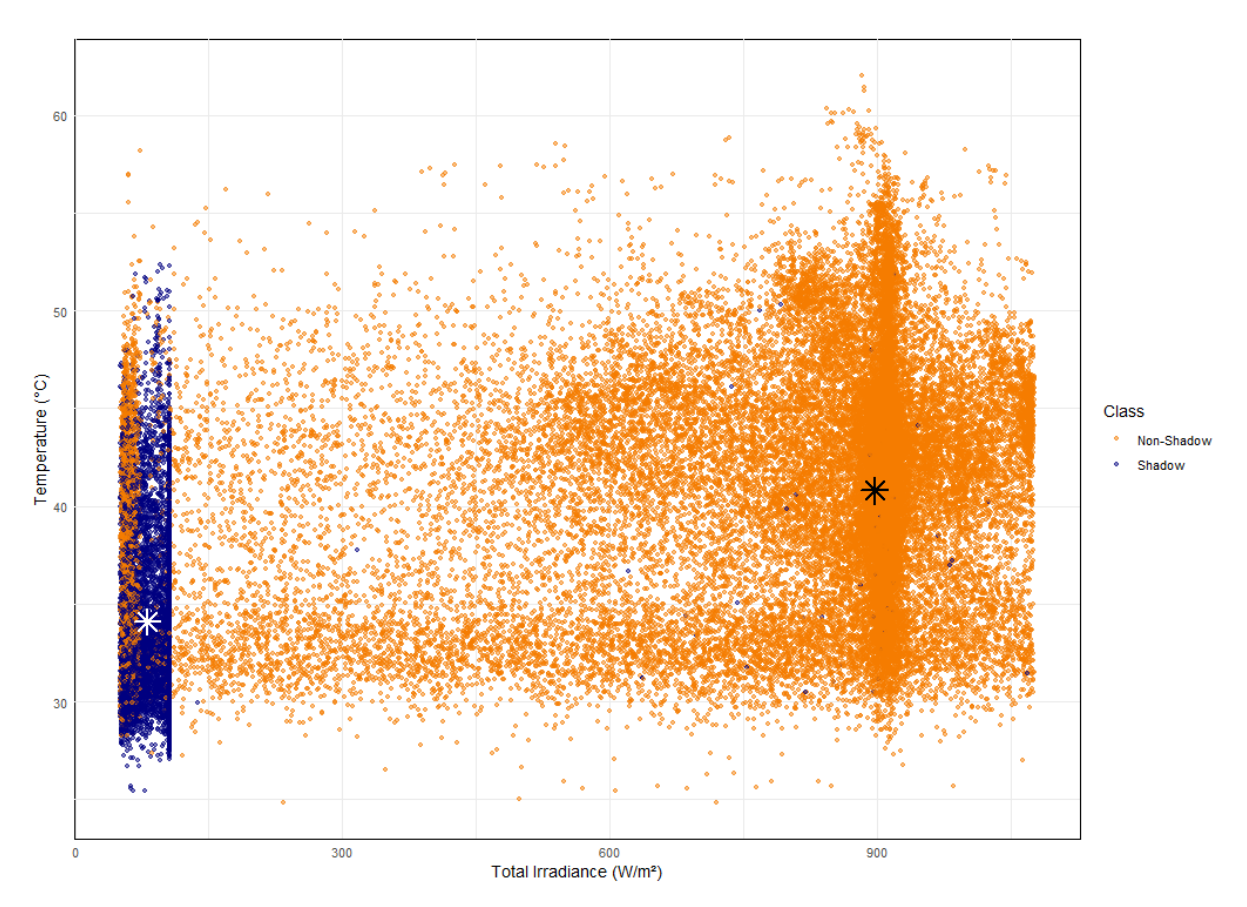


Figure 8.13 - Temperature vs Total Solar Irradiance, classified by shading: shadow and non-shadow areas

# 9. Urban Heat Vulnerability Assessment

This section primarily discusses the study of urban heat vulnerability during a heatwave. Due to the limited extent of the study area and the aim of developing a predominantly methodological approach, a dynamic study is conducted by defining potential routes (for example, a hypothetical route from home to work) to be undertaken without the use of a vehicle, for example, by bicycle or on foot. This approach is based on minimising temperature along the route, thereby ensuring transit through the coolest possible areas.

For the development of this model, QGIS software was used, along with the r.walk.points plugin, and subsequently the r.drain plugin from GRASS. The first plugin generates a raster showing the anisotropic cumulative cost of movement between different geographic positions, based on an input raster whose cell values represent the cost. In the case of our study, initially limited to the restricted area where thermal data are available, the raster considered as the cost is the surface temperature raster. More specifically, the inputs used are the elevation raster (DSM), the temperature raster containing costs (temperature), the starting point and the endpoint. The outputs obtained are the cumulative cost and movement directions. This plugin is highly useful because it accounts for the morphology of the area and the presence of obstacles (the DSM includes the heights of all surfaces, including boundary walls, buildings, and vegetation). A factor that could reduce the accuracy of the obtained routes is the presence of obstacles that are too narrow or small to be accurately represented in the DSM, which may lead to routes entering areas that are actually inaccessible. These errors can be partially mitigated by adjusting the slope factor, which determines the energy cost per unit of elevation and can be configured in the plugin interface.

Once these results are obtained, the second GRASS plugin, r.drain, is applied. Its inputs are the cumulative cost raster, the movement directions raster obtained previously, and a vector containing the start and end points. This plugin then generates the path that minimises the cost factor (in this case, corresponding to temperature).

The results are shown in Figure 9.1. It is evident that the path consistently seeks to minimise temperature, remaining within raster pixels with lower values, and, by limiting the required energy, also considers distance, favouring routes that minimise it. Moreover, it effectively avoids obstacles and follows practically applicable paths.

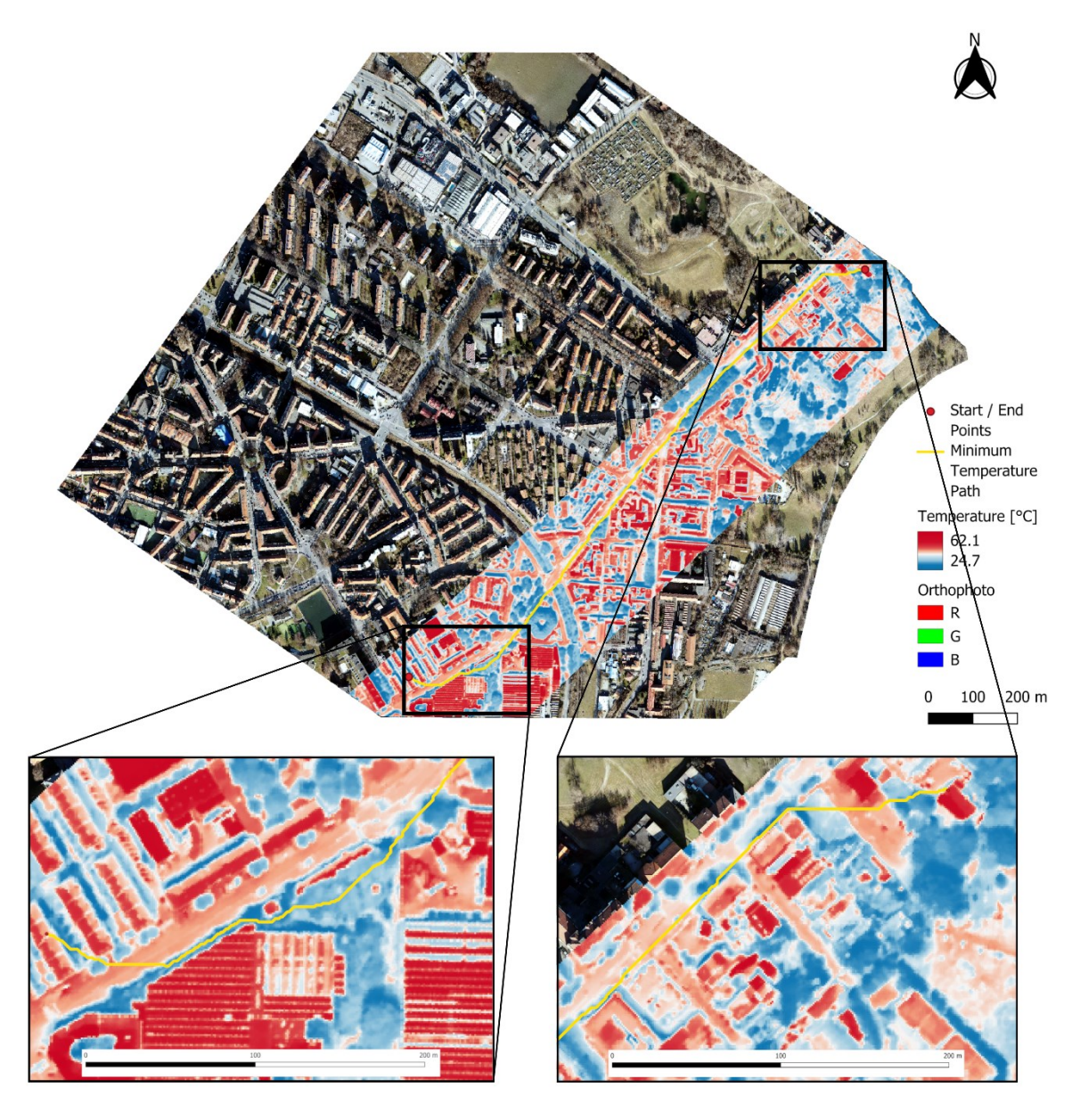


Figure 9.1 - Case 1: Temperature-minimising path

This approach, however, only works if, as in this case, a raster containing temperatures is available. Since this type of data is generally very difficult to obtain at the high geometric resolution, an additional factor that could be considered as cost is used.

Specifically, shading can be easily modelled in space and time using an accurate DSM model. Moreover, results obtained in the previous section demonstrate that shaded areas tend to have statistically significant temperature differences compared to areas exposed to solar radiation. Therefore, shading is used as a cost factor to obtain paths that, instead of minimising the temperature, maximise the shaded area. The results obtained by modelling the path using the shading corresponding to 13:30 on August 15th are shown in Figure 9.2.

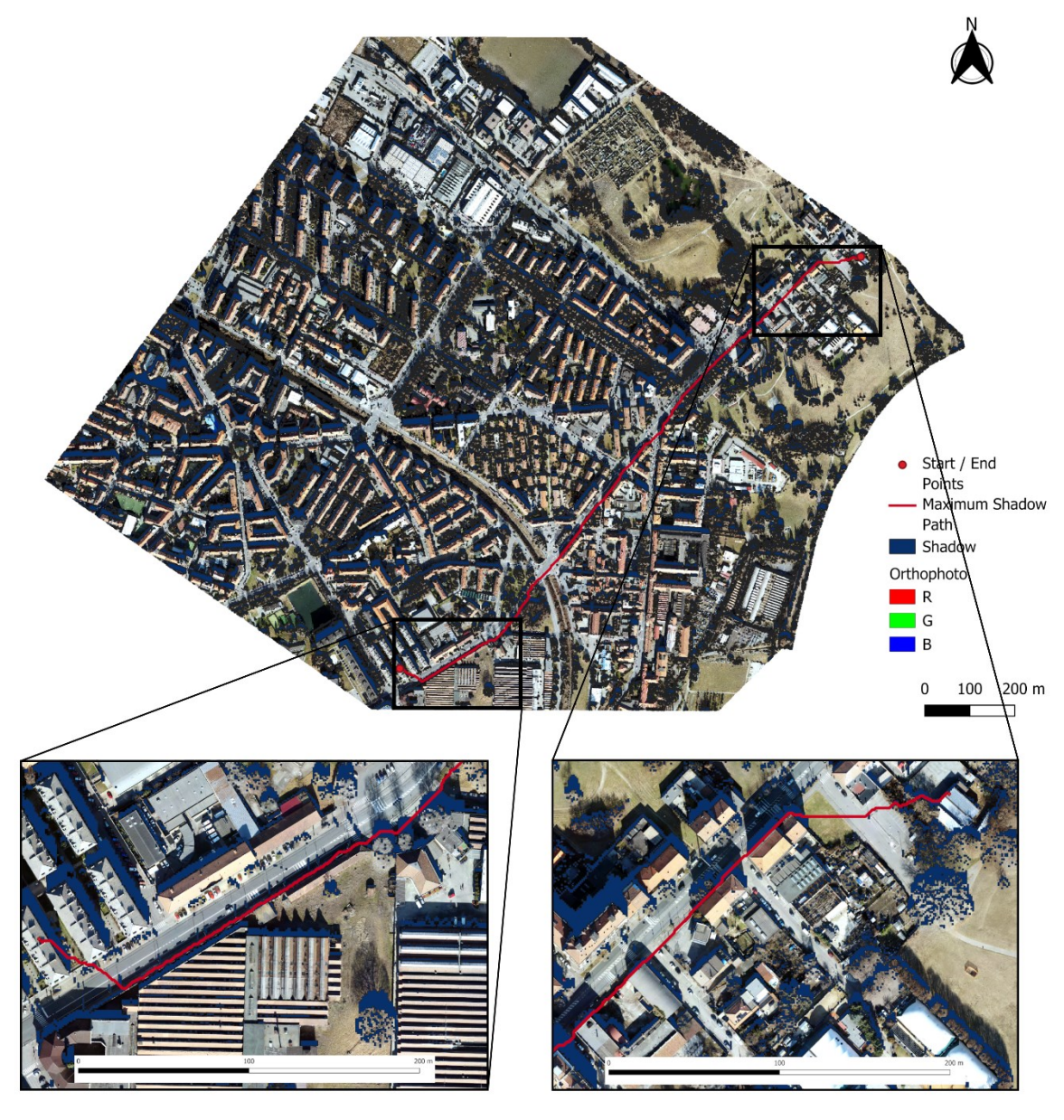


Figure 9.2 - Case 1: Shadow-maximising path

The figure above shows how, in this case, the route preferentially follows shaded areas along the entire path, minimising sun exposure, which increases the thermal comfort perceived by the pedestrian.

A comparison between the two models, the first using temperature and the second using shading as a factor, is provided in Figure 9.3. The two resulting routes are nevertheless very similar and overlap for most of the path, further demonstrating how shaded areas correspond with cooler areas.

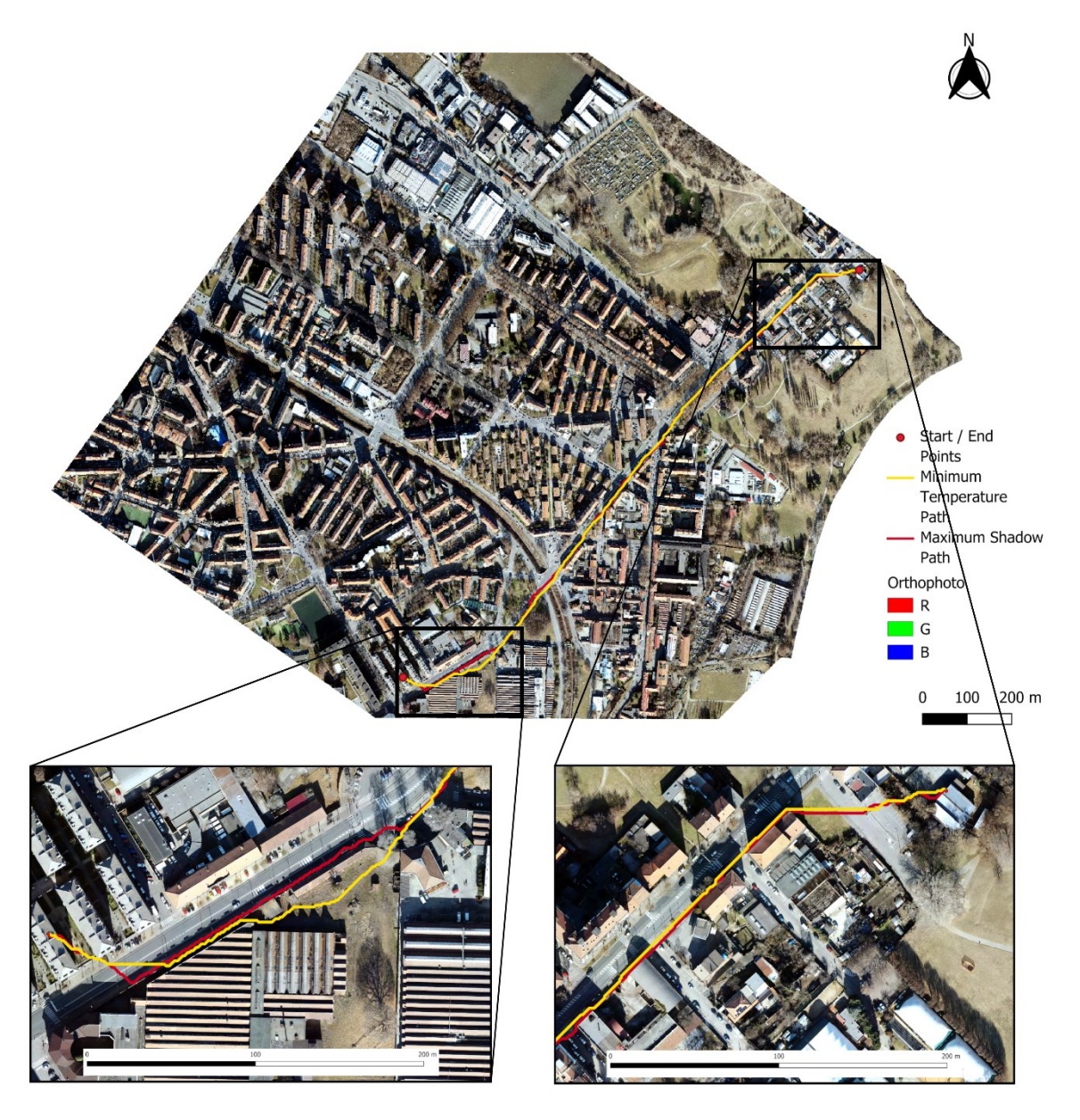


Figure 9.3 - Case 1: Comparison between paths

Given this similar behaviour between the two models, it is natural to expand the approach using a dynamic methodology to observe any changes in routes as the time of day varies, continuing to use shading as the factor to maximise. The results are calculated from the shading models obtained in Section 4, which range from 7:00 to 20:00, with an hourly frequency, and are shown in Figure 9.4 and Figure 9.6. Moreover, Figure 9.5 shows the percentage of shaded area for each path and the corresponding distance.



Figure 9.4 - Case 1: Shadow-maximising paths for each hour

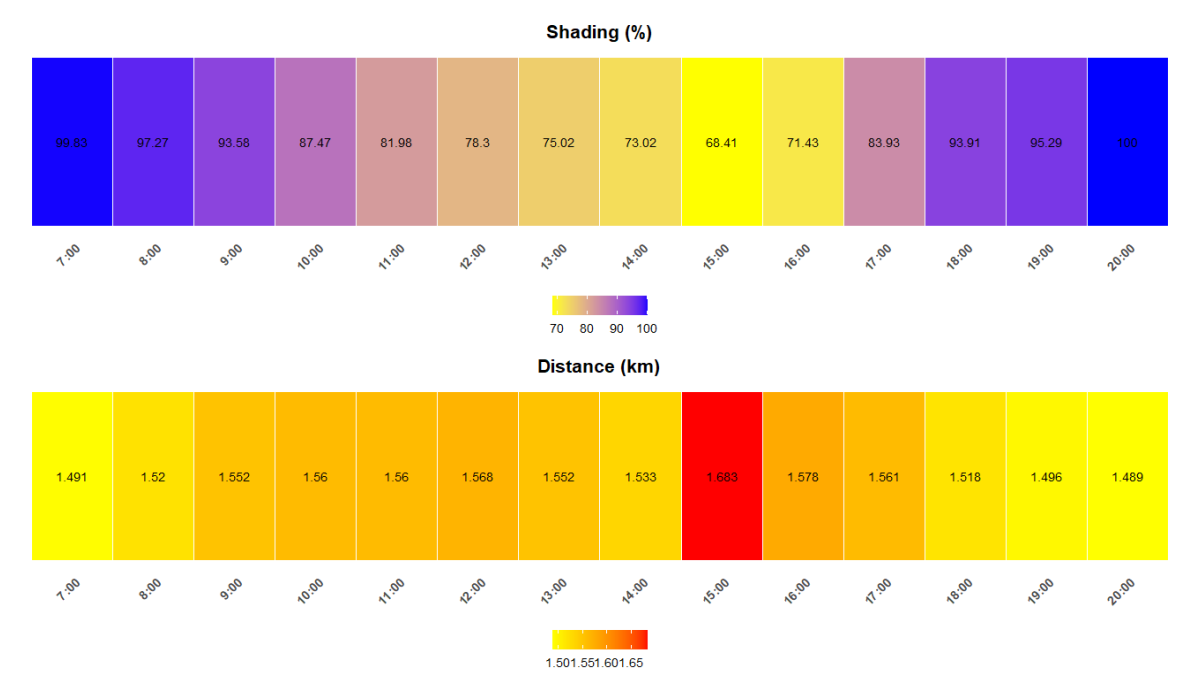


Figure 9.5 - Case 1: Shaded area proportion and corresponding path distances

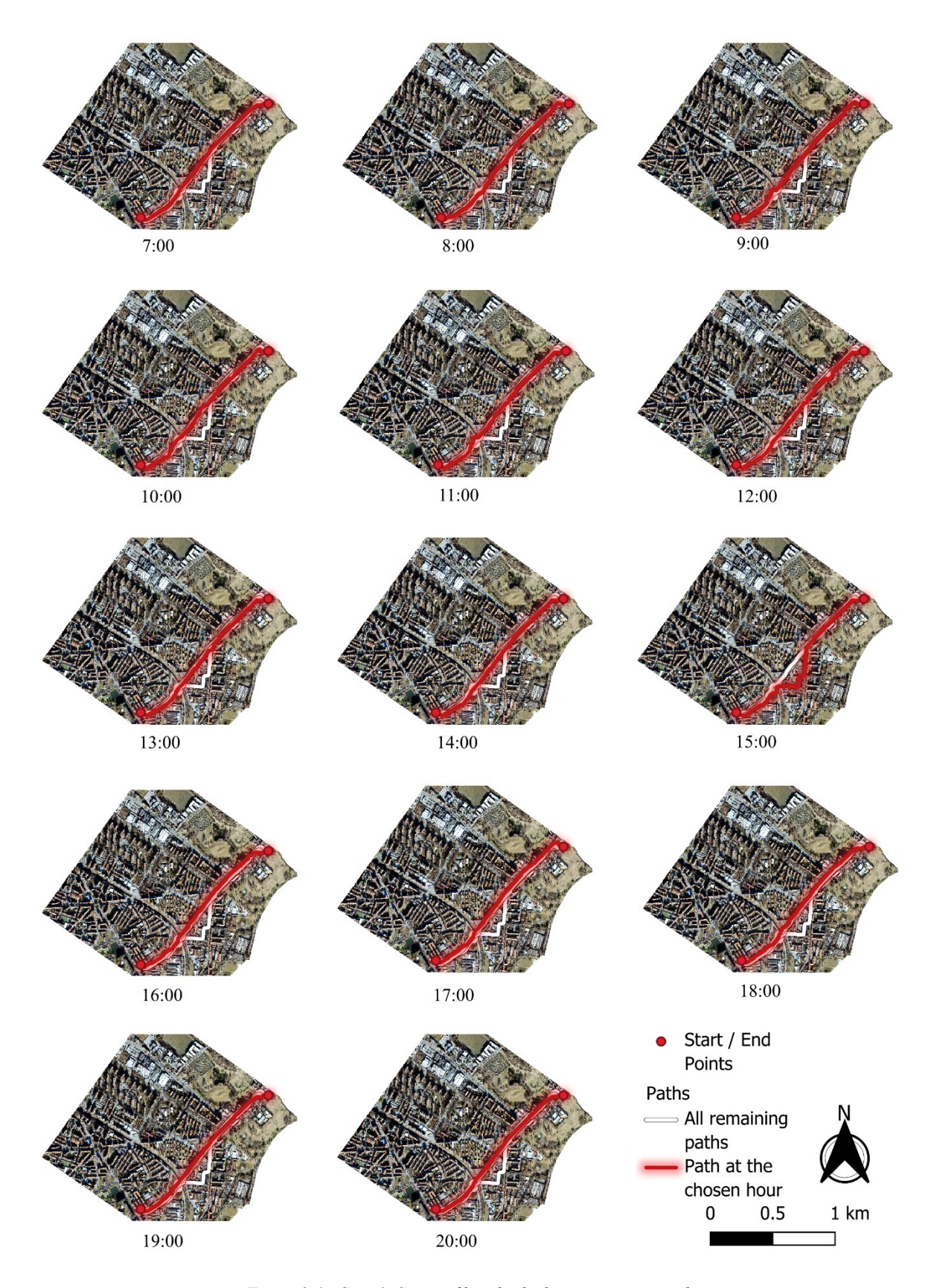


Figure 9.6 - Case 1: Series of hourly shadow-maximising paths

By calculating the percentage of shading present on each path for the corresponding time of day, it can be seen that the paths with the greatest shading are those modelled in the early morning and late afternoon, while the central hours of the day have greater solar exposure, given the limited shading of the area due to the position of the sun in the sky, which necessarily requires brief passage through areas exposed to solar radiation. The shading percentage, in fact, decreases from 99.83% in the early morning (7:00) to a minimum of 68.41% at 15:00, and then increases again towards the late afternoon, reaching 100% of shade at 20:00.

It is noticeable that, in the morning or late afternoon, the distances travelled are shorter and tend to be closer to the minimum possible distance between the starting point and the destination. During the most exposed hours, the model tries to follow continuous shaded areas, and the reduced shading leads to a longer distance to minimise solar exposure.

In general, the main variations observed in this specific case concern the change in side of the road (for example, the left or right side of the road depending on the position of the shade during the day), but in other cases there are much more significant variations, such as the one observed at 15:00, which uses an alternative route, lengthening the total journey. Specifically, the distances range from a minimum of 1.489 km experienced at 20:00 to a maximum of 1.683 km experienced at 15:00, resulting in a maximum difference of 194 m that the pedestrian must walk to reach the destination while maximising thermal comfort.

Obviously, this methodology, once the DSM and shading models are available, can be extended to any area for which data is available. For example, two different route start and end points are now considered, which extend across the original study area. In this case, the morphological structure between the two reference points is slightly more complex and features a denser urban fabric and the absence of a single straight road leading from the origin to the destination. The resulting routes are, in fact, much more variable and complex across the entire daylight period (Figure 9.7 and Figure 9.9) As expected, the routes are influenced by the position of the greatest shade continuity to reach the end point from the starting point and this also depend on the orientation of the buildings, as well as the width of the streets and the height of the buildings themselves. As in the previous case, the periods with the least shade correspond to the central part of the day, with a minimum peak of 72.96% at 13:00, and the distances travelled to reach the destination increase during these times (Figure 9.8). The maximum distances occur at 12:00 (1.514 km) and 14:00 (1.513 km), resulting in a maximum difference of 174 m compared to the minimum distance recorded at 20:00 (1.34 km). This

suggests that these times of day are more susceptible to heat and therefore require interventions to reduce heat vulnerability along the paths.



Figure 9.7 - Case 2: Shadow-maximising paths for each hour



Figure 9.8 - Case 2: Shaded area proportion and corresponding path distances

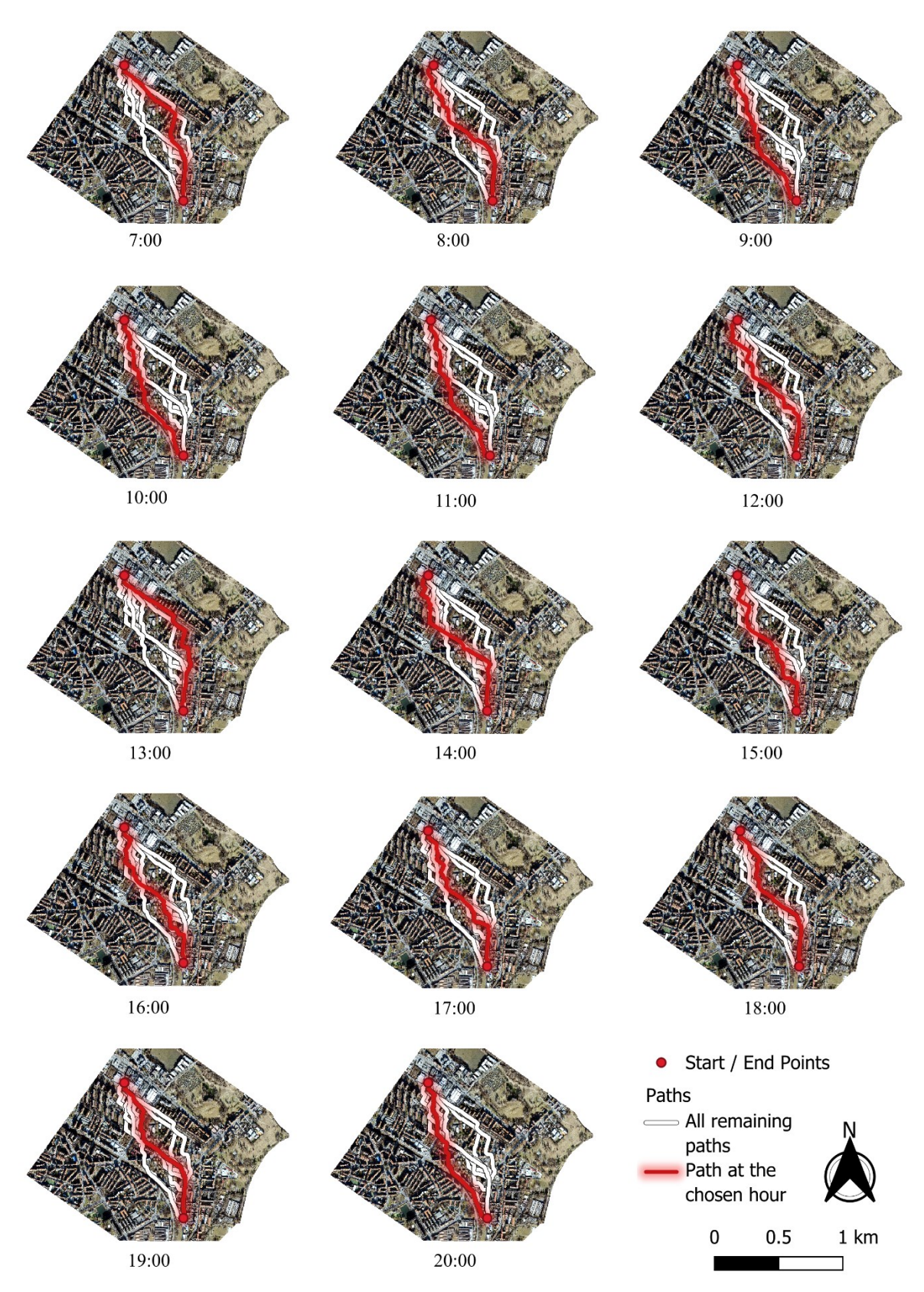


Figure 9.9 - Case 2: Series of hourly shadow-maximising paths

Given the complexity of the urban fabric in this study area, it is always advisable to verify whether a route can be effectively followed without encountering obstacles such as passages through internal courtyards or private gardens. As mentioned, these errors can be mitigated by adjusting the model's inputs.

As demonstrated in these applications, this model can be applied effectively, quickly, and intuitively, helping to counteract vulnerability to UHI during the hottest periods of the year, sometimes corresponding to increasingly frequent heat waves.

Using this approach, it is suggested to investigate, consider, and analyse the activity system, which represents the set of individual, social, and economic behaviours that generate travel demand. The activity system is essentially based on the need to access various urban functions, such as work, education, shopping, and leisure. These needs generate travel patterns that are strongly influenced by how urban spaces are organised. So, by studying and listing the main movements within the area (primarily those that allow for pedestrian movement in easily accessible areas), it is possible to visualise how, over the course of the day, the routes that tend to provide greater thermal comfort vary, although this increases the distance travelled to reach the destination. Through this vulnerability study, it is possible to identify which areas tend to become more vulnerable, especially during the hottest hours, and which are not considered suitable for pedestrian traffic, as they are highly exposed to solar radiation during peak hours. In this way, a pedestrian who needs to travel between different areas of the city can understand which zones to travel through to achieve greater thermal comfort and thus limit damage caused by extreme heat, avoiding points classified as heat hotspots and maximising the route along safe spots between two areas within the urban fabric.

From another perspective, this assessment makes it possible to identify areas where there is a greater need for interventions to reduce vulnerability to heat, for example, by planting trees that reduce temperatures both by providing shade and through evapotranspiration, or by providing additional shields to protect a given path from sun exposure and contribute to effective shading.

## 10. Conclusions

The current study aims to analyse, using high-resolution data, the urban heat island phenomenon during a heatwave in August 2025 in Turin, Italy.

To provide robust climatic considerations for the study, a long-term analysis is initially conducted on a 31-year baseline, from 1995 to 2025, to identify increasing trends in minimum and maximum temperatures recorded at the Torino Caselle weather station. Using the maximum and minimum daily temperature data, the days considered as summer HWs and tropical nights are also identified. These findings show that on 15th August 2025, the day on which the study focuses for the analysis of the UHI phenomenon, Turin is affected by a HW, reinforcing the significance of the findings.

The results obtained from the climatic study show a positive growth trend in maximum temperatures of +0.063 °C/year and in minimum temperatures of +0.060 °C/year. HWs show a positive growth trend at a rate of +0.37 HWs/year, hot days at a rate of +0.56 days/year, and tropical nights at a rate of +0.63 nights/year.

The study uses a 3D model of the urban fabric of a section of District 6, located in the northern part of the city, obtained using data provided by a LiDAR acquisition in 2022, georeferenced in EPSG:32632. The LiDAR point cloud is processed using the ENVI LiDAR software, which produces two DEMs with a spatial resolution of 1 m/pixel, corresponding to the DTM and the DSM. Specifically, the vertical accuracy of the DTM is validated using 142 GCPs obtained through previous topographic surveys, demonstrating high accuracy.

Starting from these models, the extraction of the model representing the CHM is carried out for the representation and classification of points corresponding only to tree cover, as well as the extraction of building heights and human-made volumetric units. Specifically, the extracted tree cover area accounts for approximately 13.71% of the total surface area of the study area, lower than the 24.57% of building cover, the 13.95% of roads, and the 21.93% of green areas without trees. The remaining portion of land, in addition to a very low percentage of water bodies (0.25%), is considered unclassified, as it contains several heterogeneous classes within it.

Using the DSM obtained from the LiDAR acquisition, the study models the factors that most contribute to UHI with a GIS-based approach. These factors include shading and irradiance, which have a greater influence during the daytime hours, and SVF, which determines the degree of urban canyoning. SVF has a greater impact during the nighttime hours due to lower

heat dissipation in areas that are more obstructed compared to the surrounding environment. Using shading simulations on the study area performed with the UMEP-SOLWEIG plugin on QGIS, it can be seen that the shading peaks occur as expected in the early hours of the day and in the late afternoon/evening. The peak of minimum shading occurs around 13:30, corresponding to the position of maximum height of the sun in the sky on the analysed day, 15th August (solar noon at 13:34). Minimum shading is estimated at around 19% in the area. These results are also consistent with the solar irradiance study performed using the r.sun module throughout the day and at solar noon, which indicates very high total irradiance, often exceeding 1000 W/m², that decreases only in shaded areas. Building roofs and urban parks are the locations that receive the highest exposure to solar radiation throughout the day, with

Regarding the SVF, in the study area more than half of the surfaces shows moderate to very high values, close to the maximum value of 1, while less than 8% of the surfaces, mostly road surfaces, have very low SVF values, indicating a tendency to be more shaded during the day and to dissipate heat with greater difficulty at night.

peaks of approximately 11 hours of solar radiation received.

High-resolution airborne thermal remote sensing captures extreme surface temperatures during the August 2025 HW, with one acquisition performed during the day on 15th August and another at night on 16th August. Daytime temperatures reach a maximum surface temperature of 62.1°C on buildings, while green areas and trees remain cooler. Nighttime data show higher temperatures on road surfaces (maximum surface temperature of 28.4°C), than on green areas and buildings (minimum peaking around 11.1°C). This highlights that heat retention occurs mostly on road surfaces, which are the hottest at night. Buildings, on the other hand, exhibit the greatest temperature variations between day and night, with peak differences of up to 41.8°C, indicating that exposure to the sky and the high SVF values attributed to this class contribute to cooling at night but also to greater and faster heating during hours of exposure to sunlight.

Temperature variations are therefore closely related to surface properties and SVF. Areas with high SVF exhibit the largest temperature variations, while roads with low SVF exhibit smaller day-night differences due to shading and limited heat dissipation.

During the day, surface temperature is on average 16.9°C higher than at night. Specifically, during the day, trees are classified as the coolest surfaces (average temperature of 33.1°C), while buildings, with an average of 45.0°C, are the warmest. At night, roads are the warmest surfaces, with an average of 25.0°C, while green areas are the coolest, with an average of 21.0°C.

Moreover, daytime temperatures are strongly influenced by shading. Specifically, temperatures in shaded areas average 34.1°C, compared to 40.8°C in unshaded areas.

Statistical analyses confirm that the effects of shading and SVF are significant across most land covers, meaning that integrating green areas and shading structures can significantly reduce exposure to urban heat.

Finally, a dynamic route simulation is modelled to minimise heat exposure for pedestrians and cyclists travelling between two points within the study area. Temperature and shade are used as costs, integrating urban morphology provided by the DSM. The simulations show that routes modelled in the early morning and late afternoon provide less exposure to solar radiation and minimise distance. Meanwhile, during the central hours of the day, with less shade, routes increase the total distance to avoid areas exposed to the sun. The hourly analysis identifies the timing of the highest risks of heat exposure and the hotspots within the urban area. Furthermore, the model aims to suggest potential urban planning interventions, since it highlights the most vulnerable hours, such as shading through tree planting. Since this is a methodological approach that generates a model that can be easily adapted to different contexts, further studies can be conducted on the subject, also integrating the mitigation strategies mentioned and also verifying the effective reduction of vulnerability in the most vulnerable areas.

## 11. References

- Arévalo, V., González, J., & Ambrosio, G. (2008). Shadow detection in colour high-resolution satellite images. *International Journal of Remote Sensing*, 29(7), 1945–1963. https://doi.org/10.1080/01431160701395302
- ASPRS. (2004). ASPRS Guidelines Vertical Accuracy Reporting for Lidar Data. www.ndep.gov.
- Baccini, M., Biggeri, A., Accetta, G., Kosatsky, T., Katsouyanni, K., Analitis, A., Anderson, H. R., Bisanti, L., D'Iippoliti, D., Danova, J., Forsberg, B., Medina, S., Paldy, A., Rabczenko, D., Schindler, C., & Michelozzi, P. (2008). Heat effects on mortality in 15 European cities. *Epidemiology*, 19(5), 711–719. https://doi.org/10.1097/EDE.0b013e318176bfcd
- Ballester, J., Quijal-Zamorano, M., Méndez Turrubiates, R. F., Pegenaute, F., Herrmann, F. R., Robine, J. M., Basagaña, X., Tonne, C., Antó, J. M., & Achebak, H. (2023). Heat-related mortality in Europe during the summer of 2022. *Nature Medicine*, 29(7), 1857–1866. https://doi.org/10.1038/s41591-023-02419-z
- Baltsavias, E. P. (1999). Airborne laser scanning: basic relations and formulas. In *ISPRS Journal of Photogrammetry & Remote Sensing* (Vol. 54).
- Bretheron. (2023). Surface Energy Balance (lecture 10).
- Buguet, A., Radomski, M. W., Reis, J., & Spencer, P. S. (2023). Heatwaves and human sleep: Stress response versus adaptation. *Journal of the Neurological Sciences*, 454. https://doi.org/10.1016/j.jns.2023.120862
- Collier, C. G. (2006). The impact of urban areas on weather. In *Quarterly Journal of the Royal Meteorological Society* (Vol. 132, Issue 614, pp. 1–25). https://doi.org/10.1256/qj.05.199
- Copernicus. (2024, July 18). *Heatwaves a brief introduction*. Copernicus Climate Change Service. https://climate.copernicus.eu/heatwaves-brief-introduction
- Copernicus. (2025, July 30). What is a tropical night?
- Croneborg, L., Saito, K., Matera, M., McKeown, D., & van Aardt, J. (2020). *Digital Elevation Models*. World Bank, Washington, DC. https://doi.org/10.1596/34445
- Dare, P. M. (2005). Shadow Analysis in High-Resolution Satellite Imagery of Urban Areas.
- Dash, P., Göttsche, F.-M., Olesen, F.-S., & Fischer, H. (2002). Land surface temperature and emissivity estimation from passive sensor data: Theory and practice-current trends. *International Journal of Remote Sensing*, 23(13), 2563–2594. https://doi.org/10.1080/01431160110115041

- De Razza, S., Zanetti, C., De Marchi, M., & Pappalardo, S. E. (2024). Mapping urban heatwaves and islands: the reverse effect of Salento's "white cities." *Frontiers in Earth Science*, 12. https://doi.org/10.3389/feart.2024.1375827
- Deilami, K., Kamruzzaman, M., & Liu, Y. (2018). Urban heat island effect: A systematic review of spatio-temporal factors, data, methods, and mitigation measures. In *International Journal of Applied Earth Observation and Geoinformation* (Vol. 67, pp. 30–42). Elsevier B.V. https://doi.org/10.1016/j.jag.2017.12.009
- EEA. (2025). Europe's environment and climate: knowledge for resilience, prosperity and sustainability Europe's environment 2025 Main report. https://doi.org/10.2800/3817344
- European Commission, & Directorate-General for Climate Action. (n.d.). *Consequences of climate change*. Retrieved October 22, 2025, from https://climate.ec.europa.eu/climate-change/consequences-climate-change en
- Feulner, G. (2015). *Global Challenges: Climate Change*. http://www.ncdc.noaa.gov/sotc/global/201412.
- Geoportale Regione Piemonte. (n.d.). *Geoportale Regione Piemonte*. Retrieved October 6, 2025, from https://geoportale.igr.piemonte.it/cms/
- Guth, P. L., Van Niekerk, A., Grohmann, C. H., Muller, J. P., Hawker, L., Florinsky, I. V., Gesch, D., Reuter, H. I., Herrera-Cruz, V., Riazanoff, S., López-Vázquez, C., Carabajal, C. C., Albinet, C., & Strobl, P. (2021). Digital elevation models: Terminology and definitions. *Remote Sensing*, 13(18). https://doi.org/10.3390/rs13183581
- Hämmerle, M., Gál, T., Unger, J., & Matzarakis, A. (2011). Comparison of models calculating the sky view factor used for urban climate investigations. *Theoretical and Applied Climatology*, 105(3), 521–527. https://doi.org/10.1007/s00704-011-0402-3
- Harlan, S. L., Brazel, A. J., Prashad, L., Stefanov, W. L., & Larsen, L. (2006). Neighborhood microclimates and vulnerability to heat stress. *Social Science and Medicine*, 63(11), 2847–2863. https://doi.org/10.1016/j.socscimed.2006.07.030
- Hayes, A. T., Jandaghian, Z., Lacasse, M. A., Gaur, A., Lu, H., Laouadi, A., Ge, H., & Wang, L. (2022). Nature-Based Solutions (NBSs) to Mitigate Urban Heat Island (UHI) Effects in Canadian Cities. In *Buildings* (Vol. 12, Issue 7). MDPI. https://doi.org/10.3390/buildings12070925
- Hofierka, J., Gallay, M., Kanuk, J., Šupinský, J., & Šašak, J. (2017). High-resolution urban greenery mapping for micro-climate modelling based on 3D city models. *International Archives of the Photogrammetry, Remote Sensing and Spatial*

- *Information Sciences ISPRS Archives*, *42*(4W7), 7–12. https://doi.org/10.5194/isprs-archives-XLII-4-W7-7-2017
- Hofierka, J., & Šúri, M. (2002). Proceedings of the Open source GIS-GRASS users conference. http://www.geomodel.sk
- Honjo, T., Lin, T. P., & Seo, Y. (2019). Sky view factor measurement by using a spherical camera. *Journal of Agricultural Meteorology*, 75(2), 59–66. https://doi.org/10.2480/agrmet.D-18-00027
- Huang, X., & Wang, Y. (2019). Investigating the effects of 3D urban morphology on the surface urban heat island effect in urban functional zones by using high-resolution remote sensing data: A case study of Wuhan, Central China. *ISPRS Journal of Photogrammetry and Remote Sensing*, 152, 119–131. https://doi.org/10.1016/j.isprsjprs.2019.04.010
- Incropera, F. P., & DeWitt, D. P. (1996). *Introduction to Heat Transfer* (3rd Edition). JohnWile & Sons.
- IPCC. (2013). *Climate Change 2013: The Physical Science Basis*. Contribution of Working Group I to the Fifth Assessment Report of the Intergovernmental Panel on Climate Change [Stocker, T.F., D. Qin, G.-K. Plattner, M. Tignor, S.K. Allen, J. Boschung, A. Nauels, Y. Xia, V. Bex and P.M. Midgley (Eds.)].
- IPCC. (2018). Global Warming of 1.5°C: An IPCC Special Report on the impacts of global warming of 1.5°C above pre-industrial levels and related global greenhouse gas emission pathways. Intergovernmental Panel on Climate Change (IPCC). https://www.ipcc.ch/sr15/
- IPCC. (2023). Weather and Climate Extreme Events in a Changing Climate. In *Climate Change 2021 The Physical Science Basis* (pp. 1513–1766). Cambridge University Press. https://doi.org/10.1017/9781009157896.013
- Jiao, Z. H., Ren, H., Mu, X., Zhao, J., Wang, T., & Dong, J. (2019). Evaluation of Four Sky View Factor Algorithms Using Digital Surface and Elevation Model Data. *Earth and Space Science*, 6(2), 222–237. https://doi.org/10.1029/2018EA000475
- Kaloush, K. E., Carlson, J. D., Golden, J. S., & Phelan, P. E. (2008). The Thermal and Radiative Characteristics of Concrete Pavements in Mitigating Urban Heat Island Effects.
- Kehagia, F., Mirabella, S., & Psomopoulos, C. S. (2019). Solar pavement: A new source of energy. *Bituminous Mixtures and Pavements VII- Proceedings of the 7th International Conference on Bituminous Mixtures and Pavements, ICONFBMP* 2019, 441–447. https://doi.org/10.1201/9781351063265-61
- Konarska, J., Lindberg, F., Larsson, A., Thorsson, S., & Holmer, B. (2014). Transmissivity of solar radiation through crowns of single urban trees-application

- for outdoor thermal comfort modelling. *Theoretical and Applied Climatology*, 117(3–4), 363–376. https://doi.org/10.1007/s00704-013-1000-3
- Lin, P., Gou, Z., Lau, S. S. Y., & Qin, H. (2017). The impact of urban design descriptors on outdoor thermal environment: A literature review. In *Energies* (Vol. 10, Issue 12). MDPI AG. https://doi.org/10.3390/en10122151
- Lindberg, F., Grimmond, C. S. B., Gabey, A., Huang, B., Kent, C. W., Sun, T., Theeuwes, N. E., Järvi, L., Ward, H. C., Capel-Timms, I., Chang, Y., Jonsson, P., Krave, N., Liu, D., Meyer, D., Olofson, K. F. G., Tan, J., Wästberg, D., Xue, L., & Zhang, Z. (2018). Urban Multi-scale Environmental Predictor (UMEP): An integrated tool for city-based climate services. *Environmental Modelling and Software*, 99, 70–87. https://doi.org/10.1016/j.envsoft.2017.09.020
- Lindsey, R. (2009, January 14). *Climate and Earth's energy budget*. NASA Earth Observatory. https://earthobservatory.nasa.gov/features/EnergyBalance
- Lohani, B., & Ghosh, S. (2017). Airborne LiDAR Technology: A Review of Data Collection and Processing Systems. In *Proceedings of the National Academy of Sciences India Section A Physical Sciences* (Vol. 87, Issue 4, pp. 567–579). Springer India. https://doi.org/10.1007/s40010-017-0435-9
- Mandanici, E., Conte, P., & Girelli, V. A. (2016). Integration of aerial thermal imagery, LiDAR data and ground surveys for surface temperature mapping in urban environments. *Remote Sensing*, 8(10). https://doi.org/10.3390/rs8100880
- Manune, D. F. (2007). *Digital Elevation Model. Technologies and Applications: The DEM Users Manual* (2nd ed.). American Society for Photogrammetry and Remote Sensing.
- Martinelli, L., Lin, T. P., & Matzarakis, A. (2015). Assessment of the influence of daily shadings pattern on human thermal comfort and attendance in Rome during summer period. *Building and Environment*, 92, 30–38. https://doi.org/10.1016/j.buildenv.2015.04.013
- Massimo Micieli. (2019). Aerofotogrammetria con i droni. Mappatura e modellazione 3D del territorio con tecniche aerofotogrammetriche da SAPR (Sistemi Aeromobili a Pilotaggio Remoto) (Dario Flaccovio Editore, Ed.).
- Matius, M. E., Ismail, M. A., Farm, Y. Y., Amaludin, A. E., Radzali, M. A., Fazlizan, A., & Muzammil, W. K. (2021). On the optimal tilt angle and orientation of an onsite solar photovoltaic energy generation system for sabah's rural electrification. *Sustainability (Switzerland)*, 13(10). https://doi.org/10.3390/su13105730
- Mehendale, N., & Neoge, S. (2020). Review on LiDAR technology Srushti Neoge Ninad Mehendale. https://ssrn.com/abstract=3604309

- Middel, A., Lukasczyk, J., Maciejewski, R., Demuzere, M., & Roth, M. (2018). Sky View Factor footprints for urban climate modeling. *Urban Climate*, *25*, 120–134. https://doi.org/10.1016/j.uclim.2018.05.004
- Morini, E., Touchaei, A. G., Castellani, B., Rossi, F., & Cotana, F. (2016). The impact of albedo increase to mitigate the urban heat island in Terni (Italy) using the WRF model. *Sustainability (Switzerland)*, 8(10). https://doi.org/10.3390/su8100999
- NCEI. (n.d.). *Global Surface Summary of the Day GSOD*. Retrieved October 6, 2025, from https://www.ncei.noaa.gov/access/search/data-search/global-summary-of-the-day?pageNum=4
- Nguyen, T. X. B., Rosser, K., & Chahl, J. (2021). A review of modern thermal imaging sensor technology and applications for autonomous aerial navigation. *Journal of Imaging*, 7(10). https://doi.org/10.3390/jimaging7100217
- Nichols Consulting Engineers. (2012). Cool Pavements Study Final Report.
- Nunez, M., & Oke, T. R. (1977). The Energy Balance of an Urban Canyon.
- ODonohue, D. (2023, June 27). *Signal-to-Noise Ratio (SNR) and Image Resolution*. MapScaling. https://mapscaping.com/signal-to-noise-ratio-and-image-resolution/
- Oke, T. R. (1976). *The Distinction Between Canopy and Boundary-Layer Urban Heat Islands*. https://doi.org/https://doi.org/10.1080/00046973.1976.9648422
- Oke, T. R. (1981). Canyon geometry and the nocturnal urban heat island: Comparison of scale model and field observations. *Journal of Climatology*, 237–254. https://doi.org/https://doi.org/10.1002/joc.3370010304
- Oke, T. R. (1982). The energetic basis of the urban heat island. In *Quart. J. R. Met. Soc* (Vol. 108, Issue 455).
- Oudin Åström, D., Schifano, P., Asta, F., Lallo, A., Michelozzi, P., Rocklöv, J., & Forsberg, B. (2015). The effect of heat waves on mortality in susceptible groups: A cohort study of a mediterranean and a northern European City. *Environmental Health: A Global Access Science Source*, *14*(1). https://doi.org/10.1186/s12940-015-0012-0
- Palusci, O., & Cecere, C. (2022). Urban Ventilation in the Compact City: A Critical Review and a Multidisciplinary Methodology for Improving Sustainability and Resilience in Urban Areas. In *Sustainability (Switzerland)* (Vol. 14, Issue 7). MDPI. https://doi.org/10.3390/su14073948
- Passalacqua, P., Belmont, P., Staley, D. M., Simley, J. D., Arrowsmith, J. R., Bode, C.
  A., Crosby, C., DeLong, S. B., Glenn, N. F., Kelly, S. A., Lague, D., Sangireddy,
  H., Schaffrath, K., Tarboton, D. G., Wasklewicz, T., & Wheaton, J. M. (2015).
  Analyzing high resolution topography for advancing the understanding of mass and

- energy transfer through landscapes: A review. In *Earth-Science Reviews* (Vol. 148, pp. 174–193). Elsevier B.V. https://doi.org/10.1016/j.earscirev.2015.05.012
- Payra, S., Sharma, A., & Verma, S. (2023). Application of remote sensing to study forest fires. In *Atmospheric Remote Sensing* (pp. 239–260). Elsevier. https://doi.org/10.1016/B978-0-323-99262-6.00015-8
- Planck, M. (1914). The theory of heat radiation (Blakiston, Ed.).
- Possega, M., Aragão, L., Ruggieri, P., Santo, M. A., & Di Sabatino, S. (2022). Observational evidence of intensified nocturnal urban heat island during heatwaves in European cities. *Environmental Research Letters*, 17(12). https://doi.org/10.1088/1748-9326/aca3ba
- Prakash, A. (2000). International Archives of Photogrammetry and Remote Sensing.
- Pyszny, K., Sojka, M., & Wró Yński, R. (2020). LiDAR based urban vegetation mapping as a basis of green infrastructure planning. *E3S Web of Conferences*, *171*. https://doi.org/10.1051/e3sconf/202017102008
- Ratti, C., & Richens, P. (1999). *Urban Texture Analysis with Image Processing Techniques*. http://rsb.info.nih.gov/nih-image/
- Russo, S., Dosio, A., Graversen, R. G., Sillmann, J., Carrao, H., Dunbar, M. B., Singleton, A., Montagna, P., Barbola, P., & Vogt, J. V. (2014). Magnitude of extreme heat waves in present climate and their projection in a warming world. *Journal of Geophysical Research Atmospheres*, 119(22), 12,500-12,512. https://doi.org/10.1002/2014JD022098
- Sabins, F. F., & Ellis, J. M. (2020). *Remote Sensing: Principles, Interpretation, and Applications* (Waveland Press & Incorporated, Eds.; Fourth Edition).
- Sangiorgio, V., Fiorito, F., & Santamouris, M. (2020). Development of a holistic urban heat island evaluation methodology. *Scientific Reports*, 10(1). https://doi.org/10.1038/s41598-020-75018-4
- Santamouris, M. (2015). Regulating the damaged thermostat of the cities Status, impacts and mitigation challenges. In *Energy and Buildings* (Vol. 91, pp. 43–56). Elsevier Ltd. https://doi.org/10.1016/j.enbuild.2015.01.027
- Schatz, J., & Kucharik, C. J. (2015). Urban climate effects on extreme temperatures in Madison, Wisconsin, USA. *Environmental Research Letters*, 10(9). https://doi.org/10.1088/1748-9326/10/9/094024
- Song, J.-H., Han, S.-H., Yu, K., & Kim, Y.-I. (2002). ASSESSING THE POSSIBILITY OF LAND-COVER CLASSIFICATION USING LIDAR INTENSITY DATA.
- Sun, Y., Hu, T., Zhang, X., Li, C., Lu, C., Ren, G., & Jiang, Z. (2019). Contribution of Global warming and Urbanization to Changes in Temperature Extremes in Eastern

- China. *Geophysical Research Letters*, *46*(20), 11426–11434. https://doi.org/10.1029/2019GL084281
- Syrios, K., & Hunt, G. R. (2007). Urban canyon influence on building natural ventilation. *International Journal of Ventilation*, 6(1), 43–49. https://doi.org/10.1080/14733315.2007.11683763
- Takhtkeshha, N., Mandlburger, G., Remondino, F., & Hyyppä, J. (2024). Multispectral Light Detection and Ranging Technology and Applications: A Review. In *Sensors* (Vol. 24, Issue 5). Multidisciplinary Digital Publishing Institute (MDPI). https://doi.org/10.3390/s24051669
- Todeschi, V., Pappalardo, S. E., Zanetti, C., Peroni, F., & De Marchi, M. (2022). Climate Justice in the City: Mapping Heat-Related Risk for Climate Change Mitigation of the Urban and Peri-Urban Area of Padua (Italy). *ISPRS International Journal of Geo-Information*, 11(9). https://doi.org/10.3390/ijgi11090490
- Tuholske, C., Caylor, K., Funk, C., Verdin, A., Sweeney, S., Grace, K., Peterson, P., & Evans, T. (2021). *Global urban population exposure to extreme heat*. https://doi.org/10.1073/pnas.2024792118/-/DCSupplemental
- United Nations. (n.d.). *What is climate change?* Retrieved October 22, 2025, from https://www.un.org/en/climatechange/what-is-climate-change
- van Daalen, K. R., Tonne, C., Semenza, J. C., Rocklöv, J., Markandya, A., Dasandi, N., Jankin, S., Achebak, H., Ballester, J., Bechara, H., Beck, T. M., Callaghan, M. W., Carvalho, B. M., Chambers, J., Pradas, M. C., Courtenay, O., Dasgupta, S., Eckelman, M. J., Farooq, Z., ... Lowe, R. (2024). The 2024 Europe report of the Lancet Countdown on health and climate change: unprecedented warming demands unprecedented action. In *The Lancet Public Health* (Vol. 9, Issue 7, pp. e495–e522). Elsevier Ltd. https://doi.org/10.1016/S2468-2667(24)00055-0
- Vujovic, S., Haddad, B., Karaky, H., Sebaibi, N., & Boutouil, M. (2021). Urban Heat Island: Causes, Consequences, and Mitigation Measures with Emphasis on Reflective and Permeable Pavements. In *CivilEng* (Vol. 2, Issue 2, pp. 459–484). MDPI. https://doi.org/10.3390/civileng2020026
- Wasser, L. A. (2024, September 13). *The Basics of LiDAR Light Detection and Ranging Remote Sensing*. National Ecological Observatory Network (NEON), Managed by Battelle and Funded by the U.S. National Science Foundation. https://www.neonscience.org/resources/learning-hub/tutorials/lidar-basics
- Watson, I. D., & Johnson, G. T. (1987). Graphical estimation of sky view-factors in urban environments. *International Journal of Climatology*. https://doi.org/https://doi.org/10.1002/joc.3370070210

- WHO. (2025, May 30). *Climate change and health*. World Health Organization Regional Office for Europe. https://www.who.int/europe/news-room/fact-sheets/item/climate-change
- Wien, W. (1893). Über die Gesetzmäßigkeit der Wärmeemission.
- WMO. (n.d.). *Climate change*. Retrieved October 22, 2025, from https://wmo.int/topics/climate-change
- WMO. (1983). Bibliography of urban climate 1977–1980.
- WMO. (2023, September 21). *Climate Change and Heatwaves*. World Meteorological Organization. https://wmo.int/content/climate-change-and-heatwaves
- World Meteorological Organization, & European Union. (2025). *EUROPEAN STATE* OF THE CLIMATE 2024. https://doi.org/10.24381/14j9-s541
- Zwoliński, A., & Jarzemski, M. (2015). Computing and monitoring potential of public spaces by shading analysis using LiDAR data in 3D city models. *International Archives of the Photogrammetry, Remote Sensing and Spatial Information Sciences ISPRS Archives*, 40(7W3), 743–750. https://doi.org/10.5194/isprsarchives-XL-7-W3-743-2015